Fabian Luttenberger, MSc

Electric components in automotive battery systems above 800 V

Master's thesis

Graz University of Technology

Institute of Automotive Engineering

Supervisor: Dipl.-Ing. Dr.techn. Jürgen Fabian

In cooperation with AVL List GmbH

Supervisor: Dipl.-Ing. Dr.techn. Wenzel Prochazka

Graz, July 2016

Statutory Declaration

I declare that I have authored this thesis independently, that I have not used other than the declared sources/resources, and that I have explicitly marked all material which has been quoted either literally or by content from the used sources. The document uploaded to TUGRAZonline is identical with the present work.

Eidesstattliche Erklärung

Ich erkläre an Eides statt, dass ich die vorliegende Arbeit selbstständig verfasst, andere als die angegebenen Quellen/Hilfsmittel nicht benutzt, und die den benutzten Quellen wörtlich und inhaltlich entnommenen Stellen als solche kenntlich gemacht habe. Das in TUGRAZonline hochgeladene Textdokument ist mit der vorliegenden Diplomarbeit identisch.

Date/Datum	Signature/Unterschrift

Acknowledgment

I would first like express my special thanks and appreciation to my thesis supervisor and examiner Dr. Jürgen Fabian of the Institute of Automotive Engineering at Graz, Technical University for all his help, patience, guidance, and encouragement. I would also like to thank my supervisor Dr. Wenzel Prochazka at AVL List GmbH for his help, advice, feedback, and ideas of improvement.

Many thanks go to the experts at AVL List GmbH who supported me with valuable information, ideas, and intensive feedback, specifically Dr. Volker Hennige, Ing. Michael Reiter, Dipl.-Ing. Werner Bergmayr, Dipl.-Ing. Theo Volck, Dr. Corina Taeubert, Ing. Alois Lang, and Dipl.-Ing. Ingo Hausberger.

Finally, I would like to thank my parents, girlfriend, and friends for providing me support and encouragement throughout the process of writing this thesis.

Abstract

The electric vehicles currently available have nominal system voltages of 400 V, which results in load currents up to a few 100 A. When carrying such currents, electric components, such as relays and fuses, large in size and high in weight are required that are not easy to package in a battery system. Therefore voltage levels up to 800 V are currently planned for commercial usage by automotive manufactures in order to reduce load currents and handle heat losses while using smaller components. The objective of this thesis was to investigate on the potential efficiency increase of electrical components when using higher system voltages up to 1500 V. Focus was laid on the current-carrying components in the battery system such as relays, fuses, conductors as well as lithium-ion battery cells. The effects on the electrical drivetrain, including power electronics and the electric machine, were also briefly described.

Matlab simulations were conducted to compare the behavior of the electrical components at the different system voltage levels. The simulations include a vehicle model for conversion of vehicle speed profiles into power profiles for determination of current demands, a conductor model for describing the electro-thermal behavior of the high-voltage path, and a pre-charge circuit model for describing the inrush current for loading the inverter filter capacitance at vehicle start-up.

It was found that when comparing different voltage levels while maintaining constant power demand, a significant weight and power loss reduction can be achieved for the described electrical components due to lower load currents. As more cells need to be connected in series for reaching higher voltage levels, the overall battery resistance increases. This is beneficial for limiting short-circuit currents during fault conditions. The serialization however, results in a more complex cell monitoring and connection design.

Raising the system voltage also yields higher electrical safety requirements for electrical clearance and creepage distances, withstand voltages and insulation resistances. Also market availability for electrical high-voltage components for the automotive industry is scarce as of 2016.

Kurzfassung

Die aktuell kommerziell erhältlichen Elektrofahrzeuge weisen Systemspannungen von 400 V und resultierende Betriebsströme bis zu einigen 100 A auf. Die für diese Ströme benötigten elektrischen Komponenten, wie zum Beispiel Relais und Sicherungen, sind meist groß und schwer und nicht einfach in das Batteriesystem zu integrieren. Um die stromtragenden Bauteile kleiner zu gestalten, wird derzeit das Systemspannungslevel 800 V mit dementsprechend geringeren Strömen für die kommerzielle Nutzung in Fahrzeugen von Automobilherstellern untersucht. Die zentrale Frage der vorliegenden Arbeit ist, ob eine Effizienzsteigerung der elektrischen Komponenten durch noch höhere Spannungen bis 1500 V erzielt werden kann. Hauptsächlich wird auf jene Bauteile eingegangen, die sich innerhalb des Batteriesystems befinden. Dazu gehören Relais, Sicherungen, Leiter, Verbinder sowie Lithium-Ionen Zellen. Im letzten Kapitel wird kurz die Leistungselektronik und die elektrische Maschine des Antriebstrangs erörtert.

Mit Hilfe von Matlabsimulationen wird der Einfluss der betrachteten Spannungslevel auf die elektrischen Komponenten betrachtet. Die Simulationen beinhalten ein Fahrzeugmodell zur Umwandlung von Geschwindigkeitsprofilen in Leistungsprofile, ein Kabelmodell zur Beschreibung des elektrothermischen Verhaltens des Hochvoltpfads und ein Vorladeschaltungsmodell für die Betrachtung der Einschaltströme während des Startvorgangs des Fahrzeugs.

Bei Betrachtung der Spannungslevel bei gleichem Leistungsbedarf zeigt sich eine signifikante Gewichts- und Leistungsverlustreduktion der elektrischen Bauteile auf Grund der geringeren Lastströme. Da mehr Zellen in Serie verschaltet werden müssen, um die höhere Spannung zu erzielen, steigt der Innenwiderstand des Batteriesystems. Dies wirkt sich positiv

auf die Kurzschlussstrombegrenzung in Fehler-Situationen aus. Die Serialisierung birgt jedoch komplexere Verkabelung- und Verbindungstechniken, da jeder Zellblock abgegriffen werden muss. Die höhere Betriebsspannung führt zu höheren Anforderungen an die elektrische Sicherheit, wie die Auslegung von Luft- und Kriechstrecken, Durchschlagsspannungen und Isolationswiderstände. Außerdem ist die Marktverfügbarkeit von Hochvoltkomponenten für die Automobilindustrie im Jahr 2016 gering.

Abbreviations

BEV Battery Electric Vehicle
BMS Battery Management System
CADC Common Artemis Drive Cylce
CSC Cell Supervising Circuit
CTI Comparative Tracking Index
EIS Electrochemical Impedance Spectroscopy
HV High voltage
HVIL High Voltage Interlock
IGBT Insulated Gate Bipolar Transistor
IP International Protection Marking
IT Isolated terra
LV Low voltage
MSD Manual Service Disconnect
NEDC New European Drive Cylce
NPT Non-Punch-Through
OCV Open Circuit Voltage
OEM Original Equipment Manufacturer
RMS Root Mean Square
SOC State Of Charge
SOH State Of Health
WLTP Worldwide Harmonized Light Vehicle Test Procedure

Contents

Acknowledgment i

Abstract ii

Kurzfassung iii

Abbreviations v

1. Introduction 1
- 1.1. Motivation . . . 1
- 1.2. Goal and scope of work . . . 2
- 1.3. Voltage levels . . . 4
  - 1.3.1. Classification of voltage levels . . . 4
  - 1.3.2. Definition of high voltage in electric vehicles . . . 5
  - 1.3.3. Low voltage systems in electric vehicles . . . 5
  - 1.3.4. Definition of system voltage levels . . . 6

2. Drive Cycle Analysis 8
- 2.1. The necessity of the drive cycles analysis . . . 8
- 2.2. Methodology . . . 11
- 2.3. Power profiles of WLTP and CADC . . . 13

3. Electrical Safety 17
- 3.1. Preview of standards . . . 17
- 3.2. Electrical insulation . . . 19
  - 3.2.1. Insulation resistance . . . 19
  - 3.2.2. Insulation coordination . . . 19
  - 3.2.3. Test voltages . . . 23
- 3.3. Protective measures . . . 26

4. Battery system **29**
4.1. Conditions and specifications . . . 29
4.2. Battery architecture and functionality . . . 30
4.3. Lithium-ion battery cell . . . 32
4.3.1. Cell characteristics . . . 34
4.3.2. Impedance . . . 34
4.3.3. Losses . . . 37
4.3.4. Balancing . . . 39
4.4. HV connections . . . 41
4.4.1. Thermo-electrical behavior . . . 41
4.4.2. Thermal simulation results at different voltage levels . 47
4.4.3. Replacing copper by aluminum . . . 52
4.4.4. HV connectors and terminals . . . 53
4.5. Contactors . . . 55
4.5.1. Component tasks . . . 56
4.5.2. Structure . . . 57
4.5.3. Arc suppression at different voltage levels . . . 58
4.5.4. Weight and size . . . 63
4.5.5. Contactor alternatives . . . 67
4.6. Fuse . . . 68
4.6.1. Component tasks . . . 68
4.6.2. Structure . . . 68
4.6.3. Breaking behavior at different voltage levels . . . 69
4.6.4. Weight and size . . . 73
4.7. Pre-Charge Unit . . . 76
4.7.1. Structure and switching sequence . . . 77
4.7.2. Pre-charging at different voltage levels . . . 79
4.8. Sensor technology . . . 86
4.8.1. Voltage sensing . . . 86
4.8.2. Current sensing . . . 87
4.8.3. Temperature sensing . . . 87

5. Electric drivetrain **89**
5.1. Power electronics . . . 89
5.1.1. Semiconductor behavior at higher system voltage . . . 91
5.2. Electric Machine . . . 93
5.2.1. Behavior at higher system voltages . . . 93

6. Conclusion **97**

Appendices **99**

A. Touch protection **100**

B. Pre-charging simulation results **103**

C. Matlab codes **106**

Bibliography **126**

1. Introduction

1.1. Motivation

The main motivation to write this work is the ongoing trend in the automotive industry to reduce emissions in the individual transportation sector by introducing electrification of the vehicle power train. Finite resources of fossil fuels, increasing CO_2 emissions, and the consequent climate change are being controversially discussed world-wide. Transportation accounts to 24% of the global CO_2 emissions and the demand for passenger cars is further growing [1]. Ambitious vehicle emission targets defined by politicians and the increased customer interests in environmental protections are motives for a variety of propulsion developments in the automotive industry. One trend that is currently being pursued in the industry of vehicle development is the electrification of the powertrain.

Most battery electric passenger cars currently available have maximum system voltages of 400 V. When driving such vehicles above 100 kW over longer time periods, DC currents of about 300 A are usually required. In order to handle the heat losses when carrying such currents, electric components large in geometrical size are required that are not easy to package in a battery system. Furthermore, this will also result in high costs and weight. Vehicles with voltages up to 800 V are currently planned for commercial usage, which will reduce the nominal or continuous current drawn at maximum speed and the peak currents in high load driving situations with peak power reoccurring within short time intervals. As a result, wiring and connectors are relatively small in size and can therefore overcome the issues described above [2]. These effects will be even more beneficial when raising the system voltage above 800 V. In general, when

increasing the voltage level while maintaining constant power, the current will decrease following a $1/x$ function as can be seen in figure 1.1.

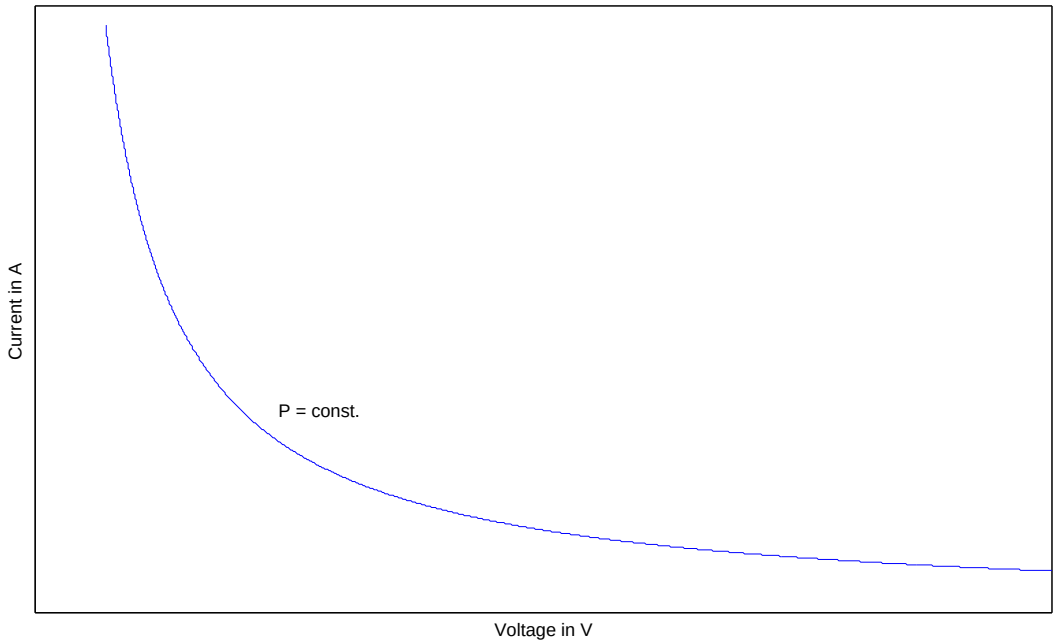

Figure 1.1.: Current plotted over voltage with constant power based on [3]

Besides the benefits, raising the system voltage yields heavier insulation of the electrical components. Also market availability for such high-voltage components for the automotive industry is scarce as of 2016 [2].

1.2. Goal and scope of work

Within the scope of this work, the behavior of the electric components of a Battery Electric Vehicle (BEV) at different voltage levels was analyzed. Voltage levels up to 1500 Vdc (within voltage class B according to ISO 6469-3 [4]) were considered. The main focus was laid on the electrical components that can be found inside the High Voltage (HV) battery system. Those components include conductors, connectors, contactors, fuses, the pre-charge unit, and battery cells. The behavior of these components at higher

voltage levels and the system impact in terms of weight and volume was described. The effects of higher system voltages were also briefly described for the power electronics and the electrical machine in chapter 5. The investigations consider small, medium sized passenger cars and sports cars. The vehicle drivetrain topology used for this study is presented in Figure 1.2.

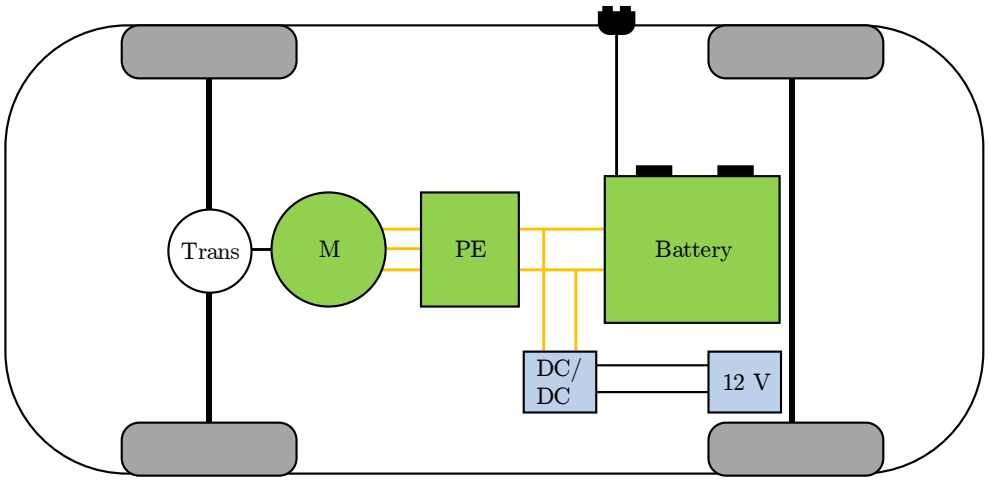

Trans	...	Transmissions
M	...	Electric machine
PE	...	Power electronics
Battery	...	HV Battery
DC/DC	...	DC/DC Converter
12V	...	Low voltage system

Figure 1.2.: Vehicle topology and electric drivetrain

The HV battery is the power source for the electrical drivetrain. The power electronics convert the DC voltage into a three-phase (or more) AC voltage for the electrical machine. Mechanical components, auxiliary devices, and the DC/DC converter supplied by the 12 V low voltage (LV) on-board power supply were not discussed in this study.

1.3. Voltage levels

1.3.1. Classification of voltage levels

Various national and international standards are dealing with voltage levels in plant and industrial engineering. The classifications into extra low, low, medium, and high voltage are given in Table 1.1. In the automotive industry, voltages up to 1000 Vac and 1500 Vdc are considered and are classified as low voltage according to EN 50110 [3].

Table 1.1.: General voltage levels according to [3]

Voltage level name	Max. Vac RMS	Max. Vdc	Referred standard	Contact protection
Protective Extra Low Voltage (PELV)	25	60	IEC 50178	without
Safety Extra Low Voltage (SELV)	25	60	IEC 61140	without
Extra Low Voltage (ELV)	25	60	IEC 60449	without
Extra Low Voltage (ELV)	50	120	IEC 60449	with
Low Voltage	1000	1500	EN 50110	double
Medium voltage	36000	-	country specific	clearance
High voltage	$>$ 36000	-	country specific	clearance

While battery electric vehicles are connected to the grid during charging, all electrical circuits are galvanically insulated to the charging infrastructure. In the vehicle, the galvanic insulation is realized by the on-board charger. In

case of DC charging the battery directly, the grid-side charging stations must ensure the isolation. As the vehicle's electrical system is always isolated from the high-voltage power supply and it has no direction earth connection, it is referred to as IT (isolated terra) system. Only if both HV poles of the battery are touched simultaneously, does this result in the risk of electric shock [3].

1.3.2. Definition of high voltage in electric vehicles

In the automotive industry, high voltage refers to voltages above 60 Vdc and 30 Vac. The components used for energy distribution of this voltage level are commonly color-coded orange. Marking live components and making a distinction between low and high voltage are especially helpful for lay persons to easily recognize the risk of an electric shock through high voltage [3].

An international standard dealing with protective measures against electrical shock and classification of voltage levels of vehicles with electric traction systems is ISO 6469 [5]. Part 3 of the standard is especially dedicated to car-integrated energy storage systems and its safe protection of persons against electric shock. It classifies electrical components in electrically propelled vehicles into voltage class A and B, which are described in Table 1.2 [4].

Table 1.2.: Voltage classes according to ISO 6469-3

Voltage level	Voltage Class	Vdc	Vac
Low voltage	A	$0 < U \leq 60$	$0 < U \leq 30$
High voltage	B	$60 < U \leq 1500$	$30 < U \leq 1000$

1.3.3. Low voltage systems in electric vehicles

Besides the automotive high voltage system (within voltage class B) supplied by the traction battery, an on-board low voltage system (within voltage class

A) is present for supplying electronic control units, sensors, and most of the vehicle's convenient features. The LV and HV systems operate independently and simultaneously from each other; galvanic isolation between the systems is imperative. The LV system is usually supplied by a 12 Vdc lead acid battery and is charged over a DC/DC converter by the traction battery. In the dangerous event of fault between the HV and LV systems, failure detection and protective circuits are necessary. The negative pole of the 12 V supply is conductively connected to the vehicle's chassis for potential equalization and insulation monitoring (refer to section 3.3) [3].

1.3.4. Definition of system voltage levels

The vehicle battery system consists of individual, rechargeable battery cells that are connected in series and in parallel to achieve the desired system voltage and energy content. The lithium-ion cell considered in this study is described in more detail in section 4.3. Depending on the active materials, the open circuit voltage is between 3 V and 4 V. For a lithium-ion cell with Nickle Magnese Cobalt (NMC) cathode materials the nominal voltage reaches 3.7 V. The voltage cut-off and safety limits during cell discharging and charging are 2.6 V and 4.2 V respectively [6, 7]. The cell cut-off voltages were considered for calculating the minimum and maximum pack voltage.

Most of the currently available small and medium sized electric vehicles have a maximum system voltage of 400 V. This results in a series connection of about 90 cells. Sports cars and prototype cars can have higher voltages up to 800 V. One example is the prototype electric vehicle Coup-e 800 V, which was developed by AVL in Regensburg, Germany [2]. Such system voltages can be achieved with about 180 cells in series. The maximum voltage that is considered throughout this work is 1500 V, the upper limit of voltage class B. This voltage level can be realized with 360 cells in series. Vehicles with such high voltages are currently not commercially available on the market. Table 1.3 summarizes the voltage levels that were compared and analyzed in this work. For a fair comparison, equal pack energy content and therefore the same number of total cells are considered for all defined voltage level. The total amount of cells in a battery pack is considered to be a multiple of 10. For simplifications, voltages have been rounded to the nearest fifty.

Table 1.3.: Definition of system voltage levels

Name	Cell in series	Minimum voltage in V	Nominal voltage in V	Maximum voltage in V	Usage
Level 1	90	250	350	400	Small and medium cars
Level 2	180	450	650	750	Sport cars, prototypes
Level 3	360	950	1350	1500	no commercial usage yet

2. Drive Cycle Analysis

Standardized second-by-second speed cycles are available for examining the emissions of light and heavy duty vehicles with internal combustion engine and are used for type approval [8]. Such speed profiles can also be used for electric vehicles to assess the performance and tank-to-wheel energy consumption. The energy efficiency has a considerate impact on the driving range and therefore on the battery capacity [9].

2.1. The necessity of the drive cycles analysis

In this work, drive cycles are used to evaluate the performance of electrical components in a battery system at different voltage levels. Such components (e.g. HV contactors or fuse) must be carefully selected to meet the performance targets of an electric vehicle. It is utterly important to not only dimension the components to optimize efficiency of the drive train but also to guarantee safety during every possible vehicle operation state. Overstressing the electrical parts can lead to overheating or even short-circuit fault. The analysis of different drive cycles covering real driving situations is therefore indispensable for designing the electrical components of a battery electric vehicle [3].

The drive cycles that are considered in this work are the Worldwide Harmonized Light Vehicle Test Procedure (WLTP) cylce and the Common Artemis Driving Cylce (CADC). Both cycles are depicted in Figure 2.1.
The WLTP cylce is being developed by the UN ECE GRPE (Working Party on Pollution and Energy) group on the basis of collections and analysis of drive data from Europe, India, Japan, Korea, and USA [10]. The data is separated into short trips and stop or idling phases. The driving profile

is comprised of four patterns: A low (up to 60 km/h), a medium (up to 80 km/h), a high (up to 110 km/h), and an extra high (above 110 km/h) pattern. When finalized, the WLTP cycle is expected to replace the New European Drive Cylce (NEDC) by the EU commission for type approval testing of light-duty vehicles [8].
The CADC was developed on the basis of a large database of European real world driving profiles within the European Artemis (Assessment and Reliability of Transport Emission Models and Inventory Systems) project. The profile consists of three patterns: Urban, Rural road and Motorway as 130 or 150 km/h variant [10]. The 130 km/h variant of the CADC has been considered in this study.

The following table summarizes the characteristics of the drive cycles:

Table 2.1.: Drive cycle characteristics

Drive cycle	Duration in s	Distance in km	Average speed in km/h	Maximum speed in km/h
WLTP:				
Low	589	3095	18.9	56.5
Medium	433	4756	44.5	76.6
High	455	7158	60.8	97.4
Extra high	323	8254	94.0	131.3
CADC:				
Urban	920	4.47	17.5	58
Rual Road	1081	17.27	57.5	112
Motorway 130	1067	28.74	97	132

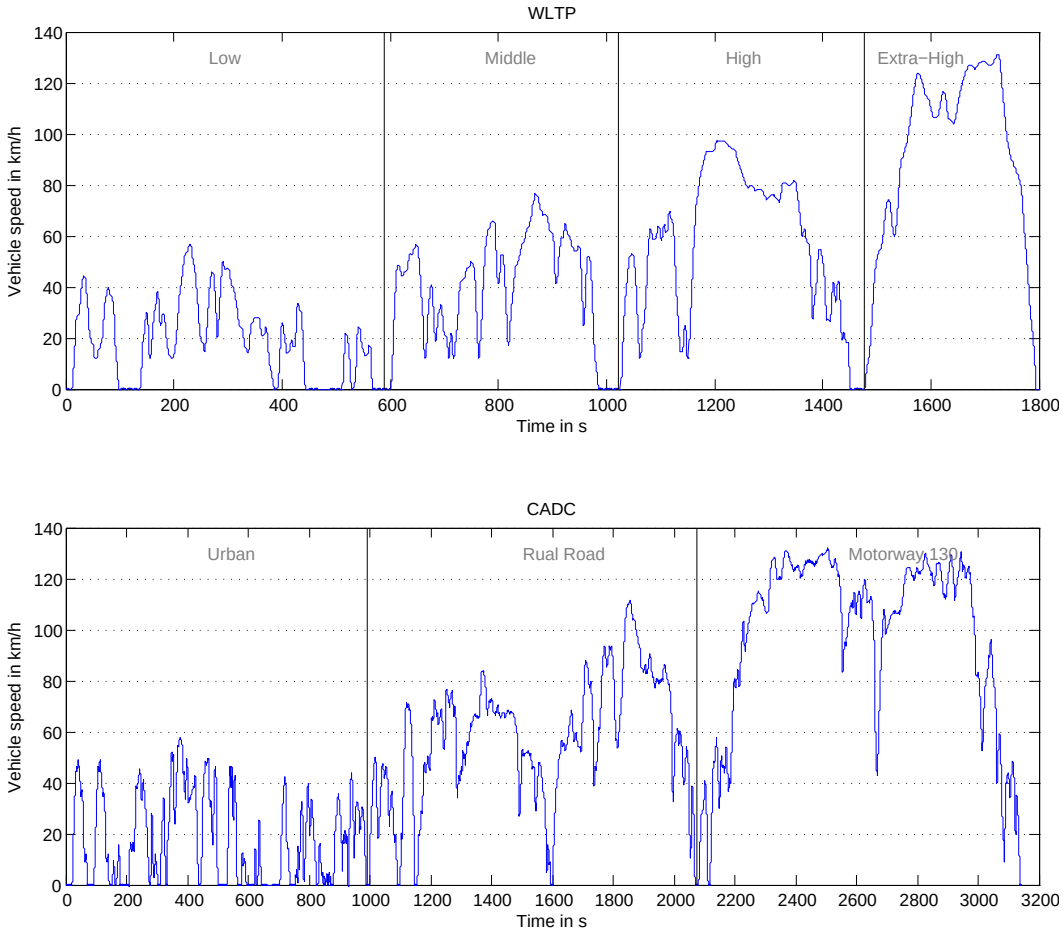

Figure 2.1.: WLTP and CADC speed profiles

2.2. Methodology

The standardized drive cycles are usually given in vehicle speed versus time. For further investigations on different system voltages of a battery electric vehicle it is necessary to calculate the power demand from such a speed profile. This can be achieved by introducing vehicle parameters such as the curb weight, front area as well as the air drag and rolling resistances. Further energy losses in the drive train, the engine, and the energy storing system also need to be taken into consideration when calculating the power demand based on a speed profile. Figure 2.2 shows the general workflow to transform the velocity profile to the dynamic power required to propel the vehicle.

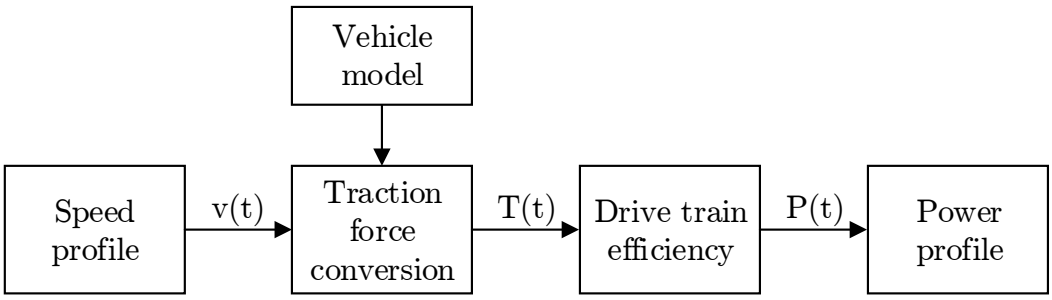

Figure 2.2.: Workflow for dynamic power calculation

The vehicle parameters and energy efficiencies of the drive train components used for the calculations are shown in Table 2.2 and are based on available vehicle data (e.g. Volkswagen Golf, Plug-In Vehicles with 50 km electric range) found in [9].

The combined efficiency $\eta_{Combined}$ can be calculated by multiplying the charging efficiency $\eta_{Charging}$, battery efficiency $\eta_{Battery}$, engine efficiency η_{Engine}, and drive train efficiency $\eta_{Drivetrain}$:

$$\eta_{Combined} = \eta_{Charging} \cdot \eta_{Battery} \cdot \eta_{Engine} \cdot \eta_{Drivetrain} = 73\% \tag{2.1}$$

The tractive force of the vehicle is needed for converting the speed profile into a power profile. The following calculations are based on [11]. For

Table 2.2.: Vehicle parameters and energy efficiency taken from [9]

Curb weight	Front area	Air drag coefficient	Rolling resistance coefficient
$1600\,kg$	$2\,m^2$	0.28	0.01
Charging efficiency	**Battery efficiency**	**Engine efficiency**	**Drive train efficiency**
90 %	95 %	90 %	95 %

simplification, it is assumed that the vehicle travels along a level road without slopes. The tractive forces F_t can be expressed as a function of the vehicle mass m, the acceleration a and the forces acting on the vehicle body as:

$$F_t = ma + F_w + F_r \tag{2.2}$$

where F_w is the aerodynamic drag force, and F_r is the rolling resistance force.

When neglecting the wind speed, the aerodynamic drag force F_w is a function of the squared vehicle speed v, the vehicle cross-section area A, the air density ρ[1], and the air drag coefficient c_d:

$$F_w = \frac{1}{2}\rho A c_d v^2 \tag{2.3}$$

The air drag coefficient c_d is highly depended on the shape of the vehicle body.

[1] At 20 °C the air density has a value of approximately 1.2 kg/m^3 [12]

The rolling resistance force F_r opposes the motion of the wheels. It is a function of the vehicle mass m, the gravitational acceleration g, and the rolling resistance coefficient c_r:

$$F_r = mgc_r \tag{2.4}$$

Considering the combined vehicle efficiency calculated in Equation 2.1, the mechanical traction power T_t can be calculated as:

$$T_t = F_t \cdot v = (ma + F_w + F_r)v \tag{2.5}$$

The electric traction power P_t that needs to be supplied by the battery can now be defined as:

$$P_t = \frac{T_t}{\eta_{combined}} = \frac{(ma + F_w + F_r)\, v}{\eta_{combined}} \tag{2.6}$$

While breaking, the kinetic energy can be recuperated by the electric engine and used to charge the battery. It is assumed that 70% of the energy is lost due to mechanical breaking [9]. For simplification, energy consumption by auxiliary consumers as well as heating and cooling consumption have been neglected in the above considerations.

It is noted that parameters such as the wheel-slip, the component attack time, the inertia of the electric machine, or other electric components require more mathematical descriptions of dynamic models and are therefore beyond the scope of this work.

2.3. Power profiles of WLTP and CADC

Figure 2.3 shows the power demands of the drive cycles with the defined vehicle model. Negative power represents discharged and positive recuperated power.

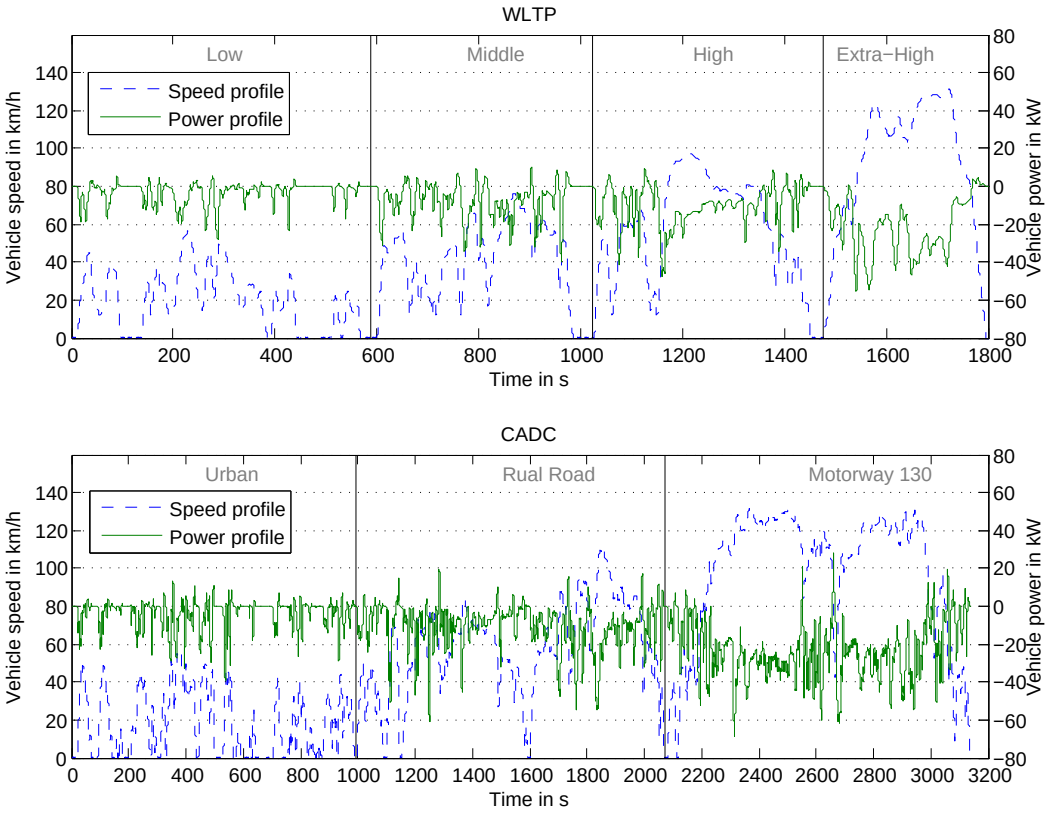

Figure 2.3.: Transformed WLTP and CADC power profiles

Table 2.3 summarizes the RMS power parameters and shows the currents for the considered voltage levels. The nominal voltages were used for current calculation. It can be noted that the current decreases with higher system voltage. The CADC leads to higher power and current requirements.

Table 2.3.: Summary of RMS power and currents at different voltage levels, nominal voltages were considered

Driving profile	RMS Power in kW	Current in A at 350 V	Current in A at 650 V	Current in A at 1350 V
WLTP	14.8	42.3	22.8	11.0
CADC	20.3	57.9	31.2	15.0

Figure 2.4 depicts the RMS currents at the prospected nominal system voltages for the RMS power of the WLTP and CADC cycle. While maintain a constant power, the current decreases with higher voltage levels following a $1/x$ function as described in section 1.1.

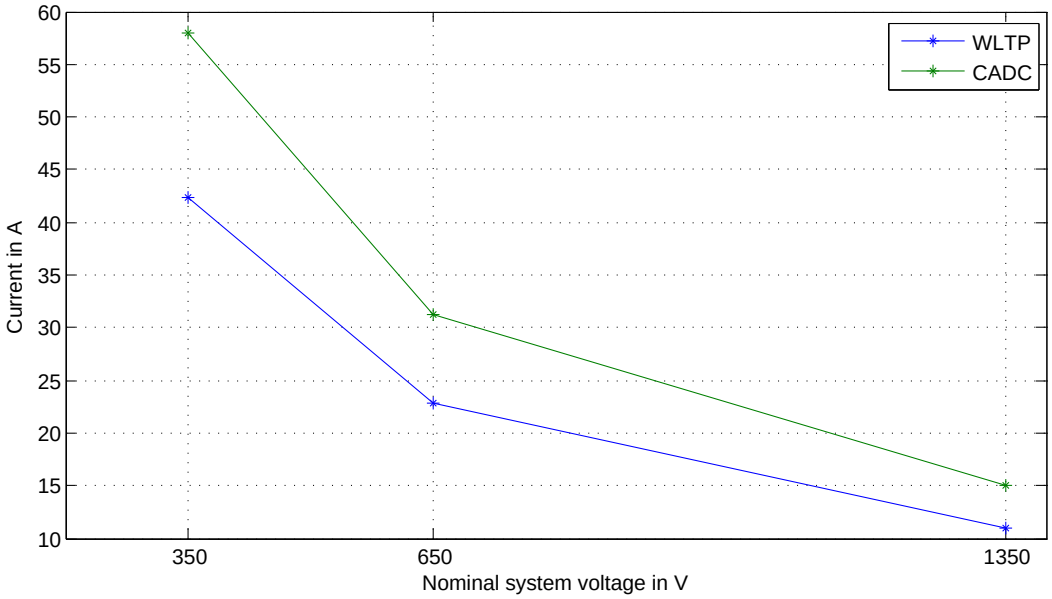

Figure 2.4.: RMS Currents for the WLTP and CADC power profiles at the prospected nominal system voltage levels

3. Electrical Safety

The electrical safety of a BEV comprises all measures for protection against and detection of electrical faults that can cause the hazard of direct contact with high voltage parts and the risk of an electric shock. The health risk associated with high voltage for people involved in the development, manufacture, maintenance or use of electric vehicles needs to be prevented. In the automotive industry, voltages above 60 V are classified as HV. Enclosures of such HV components have to be marked with a warning sign [4]. Cables are usually color coded orange for indication of HV [3].

The risk associated with high voltage within voltage class B includes [3]:

- Accidental arcs between two conductive parts
- Electric current flowing through the body caused by HV
- Electromagnetic fields affecting e.g. pacemakers

The protective measures and testings described in this work include insulation, air- and creepage distances, and functional protective measures such as insulation monitoring.

3.1. Preview of standards

As the demand for electric vehicles are growing worldwide, various international standards dealing with protective measures to ensure safety of electric vehicles have emerged. This chapters gives an overview of the standards relevant for electrical safety that have been reviewed for this study.

– **IEC 60664:** Insulation coordination for equipment within low-voltage systems [13]

  The standard defines the requirements for the insulation coordination for low voltage supplies up to 1000 Vac or 1500 Vdc. The definitions in the standard and the principles can be applied for insulation of electric vehicles to avoid hazards such as electrical shock or short circuit. The insulation coordination that covers air- and creepage definitions and testings is described in chapter 3.2.2.

– **ISO 6469 Part 1/2/3:** Electrically propelled road vehicles [5, 14, 4]

  The standard deals with safety requirements for persons inside and outside of electric vehicles and consists of 3 parts: Part 1 specifies safety requirements for on-board rechargeable energy storage systems of electrically propelled road vehicles [5]. Part 2 covers the requirements for operational safety means and protection against failures related to hazards for electric road vehicles [14]. Part 3 specifies requirements of the components of electric vehicles for the protection of persons against electrical shock [4]. The electrical insulation is described in detail in chapter 3.2.

– **IEC 61851:** Electric vehicle conductive charging system [15]

  The standard DIN EN 61851 describes charging stations of electric vehicles for voltages up to 1000 Vac and 1500 Vdc. This standard is used to reference the maximum impulse voltage of 2500 Vdc that can occur during charging the vehicle as described in chapter 3.2.2.

– **ISO 26262:** Road vehicles - Functional safety

  ISO 26262 deals with methods ensuring the functional safety of electric and electronic components in vehicles: each system function is evaluated and classified into the Automotive Safety Integrity Level (ASIL) from A to D, where D is the highest classification [6].

3.2. Electrical insulation

As the high voltage parts bear the hazard of an electrical shock, sufficient insulation of such parts must be ensured. Primarily solid insulation materials with high dielectric breakdown voltages are used for direct contact protection and insulation of the HV system against the vehicle chassis [7]. Additionally, proper clearance and creepage distances have to be provided otherwise hazardous current flow or even insulation break down may occur.

3.2.1. Insulation resistance

In electric vehicles, the insulation resistance between the HV system and the vehicle ground (e.g. chassis) indicates the safety state of the vehicle. When the insulation resistance drops below a critical value, passengers may be exposed to dangerous voltage levels. According to ISO 6469-3 [4], the insulation resistance divided by the maximum system voltage is required to be more than 100 Ω/V for DC circuits and more than 500 Ω/V for combined AC and DC circuits. The insulation resistance contributes to the slow self-discharge of the battery system. To ensure safety of the system and to reduce self-discharge, a value greater than 500 Ω/V is preferred. As this resistance is valid for the entire system, each component within the system must have a higher resistance value. The insulation further varies with and can be reduced by temperature stress, mechanical stress, electric stress and also environmental conditions such as excessive moisture or pollution. These effects need to be considered during insulation design [16]. The required insulation resistances for the defined system voltage levels are shown in Table 3.1.

3.2.2. Insulation coordination

In general, insulation coordination comprises the electrical endurance and stress of insulators. Within low voltage mains (voltages up to 1000 Vac and 1500 Vdc) insulation coordination is usually referred to as definition

Table 3.1.: Minimum required insulation resistance for different maximum system voltages according to ISO 6469-3

System voltage level	Maximum system voltage in V	Minimum required insulation resistance in kΩ
Level 1	400	200
Level 2	750	375
Level 3	1500	750

of clearance and creepage distances between two conductive parts that have to be fulfilled in order to avoid the hazard of an electrical shock. The clearance distance is the *"shortest distance in air between two conductive parts"* and the creepage distance the *"shortest distance along the surface of a solid insulating material between two conductive parts"* as stated in IEC 60664-1 [13] and depicted in Figure 3.1.

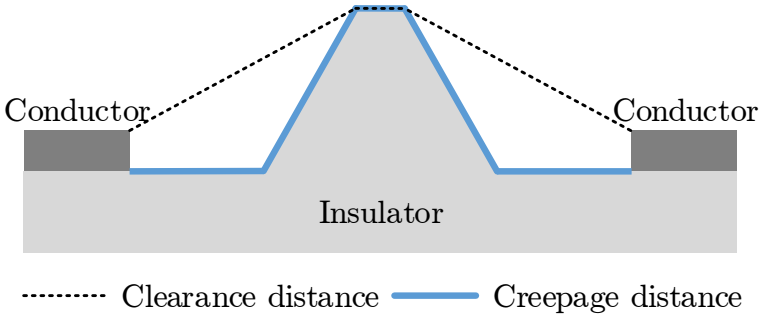

Figure 3.1.: Clearance and creepage distance

Clearance distance at different voltage levels

The clearance distance between two conductive parts is depended on the type of electric field, the required impulse withstand voltage, the pollution

degree, and the sea level [13].

The type of field between two conductive parts can be assumed as inhomogeneous as stated in IEC 60664-1 *"electric field which does not have an essentially constant voltage gradient between electrodes (non-uniform field)"* [13].

The impulse withstand voltage is the highest peak voltage that can occur between two conductive parts. According to Table F.1 in IEC 60664-1 the rated impulse voltage is 2500 V for a 230/400 V three-phase supply system [13]. IEC 61851-23 states that charging stations limit the rated impulse voltage: *"The isolated d.c. EV charging station shall reduce overvoltage to the EV to the rated impulse voltage of 2500 V"* [17].

The amount of dry pollution or condensation present in the environment can be classified into degrees of pollution. High voltage components in an electric vehicle are usually protected by sealed enclosures to minimize environmental influences such as moisture [16]. It is assumed that pollution degree 2 or 3 can be expected within HV components. The pollution degrees are cited from IEC 60664-1 [13]:

- Pollution degree 2: *"Only non-conductive pollution occurs except that occasionally a temporary conductivity caused by condensation is to be expected"*.
- Pollution degree 3: *"Conductive pollution occurs or dry non-conductive pollution occurs which becomes conductive due to condensation which is to be expected"*.

As can be seen in Table 3.2 in accordance with IEC 60664-1, for a rated impulse voltage of 2500 V the clearance distance is 1.5 mm for all pollution degrees. It should be noted that part tolerances should be considered for reaching the absolute minimum distance of 1.5 mm between to conductive parts.

Table 3.2.: Clearance distances according to IEC 60664-1

	Clearance distance in mm		
Rated impulse voltage in V	Pollution degree 1	Pollution degree 2	Pollution degree 3 and 4
2500	1.5	1.5	1.5

The shown clearance distance is valid for altitudes up to 2000 m. For higher altitudes the air pressure changes and the required clearance distance needs to be larger. The clearance distance is therefore multiplied with an altitude correction factor according to Table A.2 in IEC 60664-1. The correction factors up to an altitude of 6000 m are shown in Table 3.3.

Table 3.3.: Altitude correction factors up to 6000 m according to IEC 60664-1

Altitude in m	Multiplication factor for clearance	Resulting clearance distance[1] in mm
2000	1.00	1.5
3000	1.14	1.7
4000	1.29	2.0
5000	1.48	2.3
6000	1.70	2.6

[1] rounded to the nearest tenth

In conclusion, the clearance distance is depended on the rated impulse voltage that can occur within the system. Within voltage class B (refer to Table 1.2) the clearance distance is unaffected by the vehicle system

voltage.

Creepage distance at different voltage levels

The creepage distances between two conductive parts over the surface of an insulator is depended on the system voltage, the pollution degree, and the material class.

The material class of an insulator is classified by its Comparative Tracking Index (CTI). The CTI value ranks the insulator in its ability to conduct current along its surface under specific test conditions [18]. In accordance with IEC 60664-1 and as shown in Table 3.4, an insulator can be classified into different material groups (I, II, and III) according to its CTI value. The test procedure for determining the CTI value of an insulator is described in IEC 60112 [13].

Table 3.4.: CTI values according to IEC 60664

Material group I	$600 \leq \text{CTI}$
Material group II	$400 \leq \text{CTI} < 600$
Material group III	$175 \leq \text{CTI} < 400$

The creepage distances for the different material groups and pollution degrees are plotted against the voltage level in Figure 3.2.2. For worst-case consideration, the maximum system voltage levels (see Table 1.3 in chapter 1.3.4) are used for interpolating the creepage distances as in Table 3.5.

The creepage distances are increasing for higher voltages. The influence from the pollution degree and material groups are more present at higher voltages. It is assumed that insulation has to be larger in size to meet the higher creepage distances.

3.2.3. Test voltages

A withstand voltage or dielectric strength and an insulation resistance test has to be conducted to ensure the proper function and verification of an

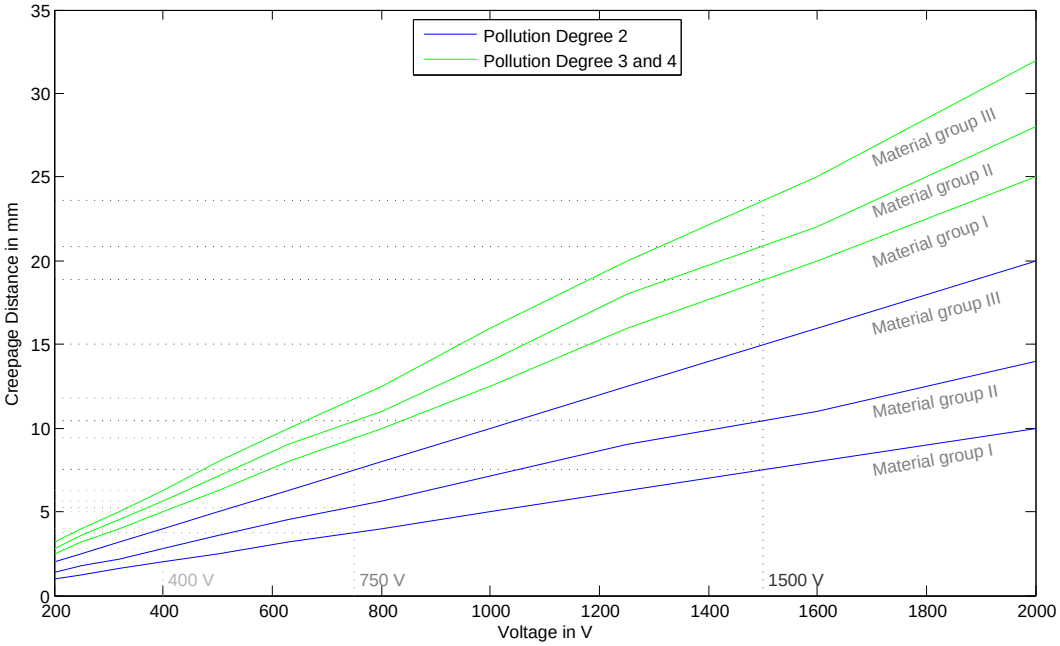

Figure 3.2.: Creepage distances according to IEC 60664

Table 3.5.: Interpolated creepage distances according to IEC 60664

	Creepage distance[1] in mm					
	Pollution degree 2			Pollution degree 3		
Max system voltage in V	Material group I	Material group II	Material group III	Material group I	Material group II	Material group III
400	2.0	2.8	4.0	5.0	5.6	6.3
750	3.8	5.3	7.5	9.5	11.4	11.8
1500	7.6	10.5	15.0	18.9	20.9	23.6

[1] Rounded to the nearest tenth

electrical insulation as protection against electric shock. Besides the proof of the dielectric strength of the insulator, the tests are carried out to control the quality and detected manufacturing faults. The tests are also used to determine the condition of the insulation after applying various stresses such as mechanical, thermal or environmental conditions. Such stresses lead to degradation and aging of the insulator. Various standards describe different test procedures with different test voltages [16]. The test procedures for verification of the insulation shown in this study is based on IEC 60664-1 and ISO 6569-3.

Verification of clearance distance

According to IEC 60664-1, an impulse voltage withstand test with the rated impulse voltage (in this study 2500 V) is used to assess the stresses caused by transient over voltage for altitudes up to 2000 m. The voltage is applied with a 1.2/50 μs waveform for a minimum of 3 impulses of each polarity with a pause of 1 s between pulses. It has to be noted that the clearance testing also stresses the solid insulation.

Verification of solid insulation

Based on IEC 60664-1, the DC test voltage for solid insulation has to be set to the rated impulse voltage and is applied for 1 minute without insulation breakdown [13]. In order to avoid pre-damaging of the insulation, alternatively a lower test voltage can be specified by the vehicle manufacturer according to ISO 6469-3 [**iec6469-3**]. The test voltage has then to be higher than the maximum system voltage but lower than the rated impulse voltage:

$$U_{Systemmaximum} < U_{Test} < 2500V \tag{3.1}$$

Verification of insulation resistance

As no ideal insulation material exists, a marginal current flow through the insulation will always be present. For examining the condition of the insulation, a insulation resistance test need to be performed. This is usually done by measuring each high voltage part's HV+ and HV- potential to the vehicle ground separately [16].
According to to ISO 6469-3 [4], the applied test voltage shall be a DC voltage of at least the maximum system voltage for a time long enough to obtain stable resistance reading.

3.3. Protective measures

Besides the correct selection of the electrical insulation, other design and functional measures have to be met to ensure electrical safety. The measures described in this section include double or reinforced insulation, equipotential bonding, insulation monitoring, touch protection, and HV interlock [3].

Double and reinforced insulation

In battery systems, *basic insulation* provides first-level protection against direct contact with live parts. However, safety of the system is provided by a second-level protection in the event of basic insulation failure. This can be achieved through *supplementary insulation*, which applied in addition to basic insulation makes up *double insulation*. If for such double insulation the basic and supplementary layer cannot be tested separately, the insulation is referred to as *reinforced insulation* [18].

Insulation monitoring

As the vehicle's HV system can be described as isolated terra, there is no common ground for the HV and the LV system. The first insulation fault between the HV circuit and the chassis will result in a single-fault condition. Depending on the operation strategy of the vehicle, this condition does not necessarily cause the supply system to shut off. However, it should only be operated as long as necessary, as passengers may be exposed to high voltage [19].

In order to detect such an insulation fault and to ensure second-level safety, it is necessary to observe insulation degrading or failure over the vehicle lifetime. Therefore the insulation condition is monitored by an insulation monitoring system installed in the Battery Management System (BMS) [20]. If the insulation resistance decreases significantly and drops below the required value, the system detects it as an insulation failure. The measurement has to be done periodically or continuously and the user has to be notified by a warning if a fault is detected [4]. Figure 3.3 depicts a typical structure of a HV system with integrated insulation monitoring.

Touch protection

HV components are required to be touch protective with complete finger (VDE finger) safety with IPXXB (see Appendix A), which may be tested with a test finger [3].

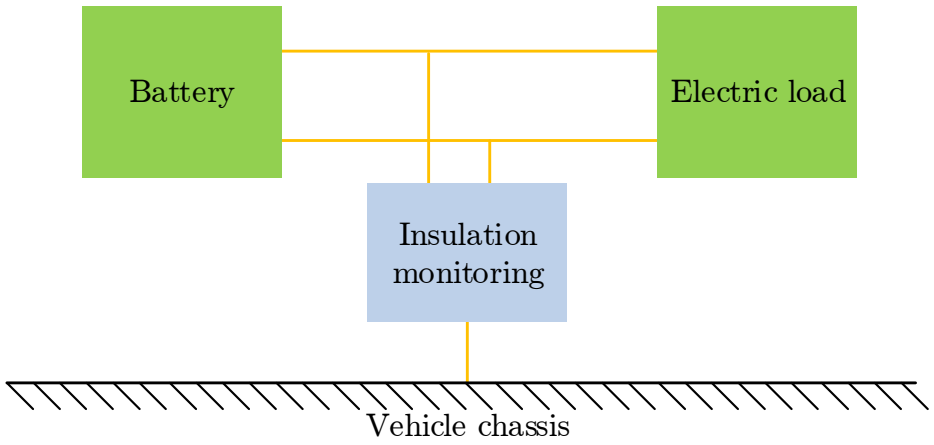

Figure 3.3.: Principle structure of a HV system with insulation monitoring adapted from [7]

Equipotential bonding

For protection against indirect contact with live parts, low impedance connection of the chassis with metallic HV enclosures is required [3]. The resistance of the equipotential bonding path has to be less than 0.1 Ω according to ISO 6469-3 [4].

Interlock

A High Voltage Interlock (HVIL) circuit is used to symbolize status of the HV circuit. Any break in the interlock circuit indicates an open high voltage path and a alarm signal will be sent to the BMS to disconnect the battery [16].

4. Battery system

A battery system used to power an electric vehicle consists of individual, rechargeable battery cells that are interconnected in series and in parallel. The system is controlled by the BMS that switches the power to the vehicle and monitors the cell voltage, temperature, and current. In this chapter focus is laid on the electric components in a battery system and their behavior at different voltage levels that include cells, HV connections, switches, fuses, and the pre-charge unit.

4.1. Conditions and specifications

The following definitions describe some general conditions and specifications of a battery system:

- State of Charge (SOC): Describes the remaining battery pack capacity and is given in percentage of maximum battery energy content.
- State of Health (SOH): An indication of the battery life cycle and a measure of its capacity relative to a new battery.
- Open circuit voltage (OCV): Voltage between the battery terminals with no load applied. The OCV increases with increasing SOC.
- Nominal voltage: Reference voltage of the battery pack, which is usually at 50% SOC.
- Cut-off voltages: Minimum and maximum allowable voltages, which also represents an empty battery pack.
- Capacity in Ah: Available volumetric capacity of the battery pack, which depends on the discharge current, cut-off voltage, and temperature.

- Nominal energy content in Wh: Product of the capacity and nominal pack voltage. Current commercially available electric vehicles have battery capacities of up to 90 kWh.
- Maximum continuous currents: Maximum discharging and charging currents at which the battery pack can be operated. Exceeding these limits for short time (e.g. 30 s current peak) is possible during peak operations such as acceleration or breaking. The limits are defined in order to avoid any damage of the system due to temperature increase caused by heat losses.
- C-rate: Defines the discharge or charge speed of the battery pack. 1C means the battery will be discharged or charged within 1 hour. 2C means the battery will be discharged or charged within half an hour.

4.2. Battery architecture and functionality

Figure 4.1 shows a typical battery pack system schematic.

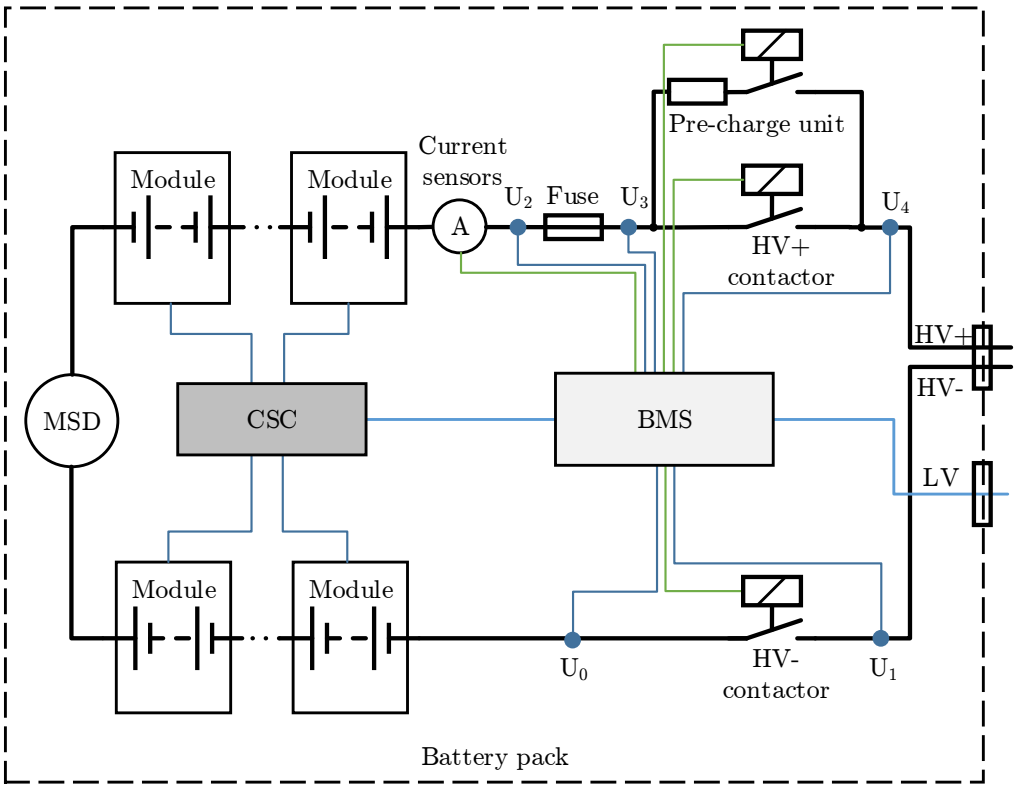

Figure 4.1.: Schematic battery pack architecture

A module is formed by connecting single cells (typically about 10 to 12 cells) in a metallic enclosure, then a pack is assembled by connecting several modules in series. The individual cells in the module can either be connected in series or in parallel. The serialization of cells raises the output voltage, a connection in parallel increases the ouput current and capacity. The battery is actively controlled by the BMS that get its inputs from the Cell Supervising Circuit (CSC) and the voltage and current measurements. The CSC monitors the voltages of all cell blocks connected in series and cell temperatures for safety reasons and can be either located directly at the modules or in central spot in the pack (as shown in the system schematic). Later strategy will increase the wiring effort, as each cell voltage and temperature signal must be routed from the modules to the central CSC. The BMS calculates

the important and safety relevant electrical characteristics such as state of charge, maximum charge or discharge power. The main contactors are controlled by the BMS and are used to switch the battery between the 'on' and 'off' state. A pre-charge unit is used to limit inrush-currents caused by the inverter filter capacitance. The main fuse is used for over-current protection such as short-circuit. The contactors, pre-charge unit and fuse will be described in detail in section 4.5 to 4.7. The voltage points U_0 to U_4 are used to measure pack voltage, to supervise if the contactors are in their requested "on" or "off" state, and to monitor if the fuse is blown. A Manual Service Disconnect (MSD) is typically placed in the "middle" of the pack to cut the battery pack voltage in half once the switch is opened. The MSD must be accessible from the outside of the battery allowing service engineers to cut the HV path before opening the pack. Most MSDs also utilize HVIL circuit integration. Once the switch is opened and the HVIL circuit is cut, the HV contactors will open [7].

4.3. Lithium-ion battery cell

Figure 4.2 shows the structure and the working principle of a typical lithium-ion battery cell used for automotive applications.

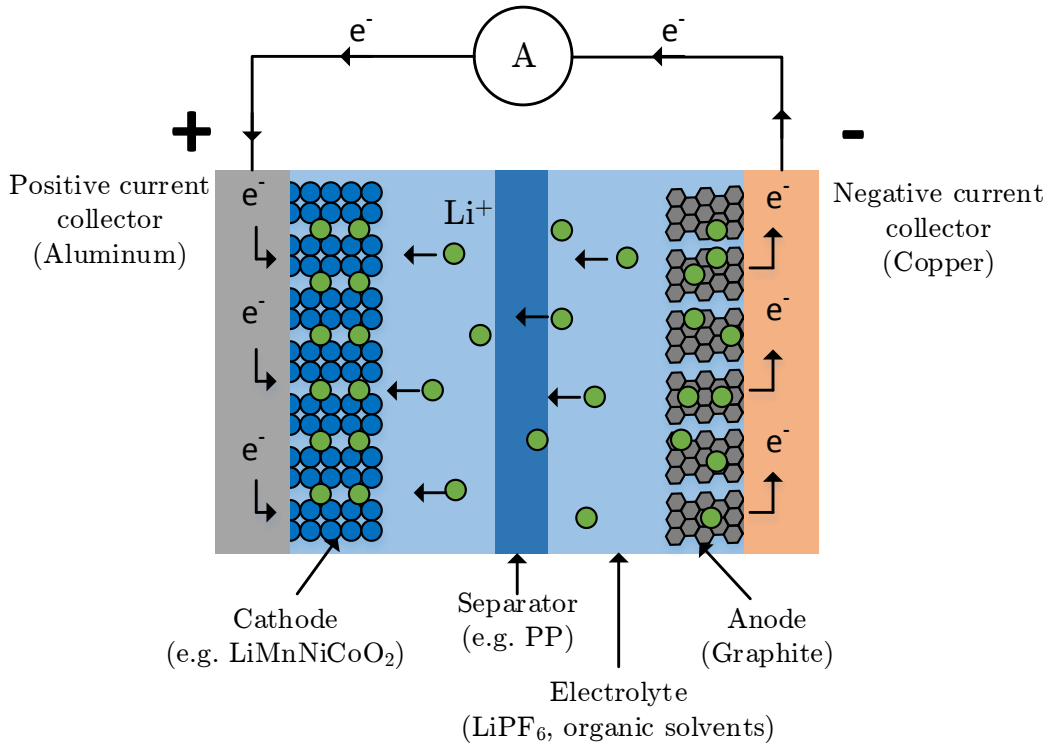

Figure 4.2.: Principle structure of a lithium-ion cell and working principle during discharge

The main elements of the cell are the positive and negative electrode, and the electrolyte. A porous separator diaphragm (e.g. polypropylene or polyethylene) is used to electrically insulate both electrodes from each other but allows for Li^+-ion diffusion. The active material of the positive electrode is made from a metal oxide (e.g. $LiMnNiCoO_2$), the material of the negative electrode is made from carbon (e.g. graphite). The electrolyte usually consists of lithium salt (e.g. $LiPF_6$) dissolved in a mixture of organic solvents. During discharging or charging, the Li^+-ion move between the electrodes and either insert into the electrodes (intercalation) or extract from the electrodes (deintercalation). During cell discharging (shown in Figure 4.2) the Li^+-ions deintercalate from the graphite anode and insert into the layered oxide cathode. The negative electrons move over the negative current collec-

tor (copper) over the load to the positive current collector (aluminum). The described process is reversed for charging where the Li^+-ions extract from the layered oxide and intercalate into the graphite [7].

4.3.1. Cell characteristics

The cell studied in this work is a commercial 50Ah pouch-type lithium-ion cell with NMC/graphite chemistry. The specifications for such a cell were taken from [21] and internal AVL documents [22] and are shown in Table 4.1.

Table 4.1.: Cell characteristics NMC/graphite lithium-ion pouch cell

Positive electrode	$LiMnNiCoO_2$
Negative electrode	Graphite
Electrolyte	$LiPoF_6$, organic solvents
Nominal voltage	3.7 V
Maximum open-circuit voltage	4 V
Maximum cut-off voltage	4.2 V
Minimum open-circuit voltage	3 V
Minimum cut-off voltage	2.6 V
Cell capacity	50 Ah

4.3.2. Impedance

The cell impedance R_{cell} is depended on different electro-chemical and mechanical factors, such as voltage, current, temperature, SOC, and cell age[1]. Figure 4.3 represents the impedance by an equivalent electric circuit.

[1]Aging is observed as capacity fades over cell cycling (number of complete charges and discharges) and calendar life (capacity loss through temperature and time due to self-discharge), resulting in cell energy decrease

Depending on the desired accuracy, the model application, and the time domain, the number of RC elements can be varied. The model accuracy increases with a higher number of RC elements, which however results in a more complex circuit. Whenever a lithium-ion battery cell is discharged or charged, a voltage drop or rise ΔV over the internal cell impedance R_{cell} can be observed. The immediate change in voltage depends on the ohmic resistance R_Ω, which mainly represents the limited conductivities of current collectors, terminals, active materials, and the electrolyte. A much slower voltage change over the additional polarization resistance is caused by the charge-transfer reactions of the electrodes and concentration-related effects such as diffusion. The elements R_i and C_i result from effects such as charge transfer and interfacial capacitance and describe the transient behavior during discharging and charging [23]. The battery cell Open Circuit Voltage (OCV) is represented as an ideal voltage source U_{OCV} in series with the cell impedance. The inductivity is commonly omitted as it usually has minor impact on the impedance behavior of a battery cell [21, 24].

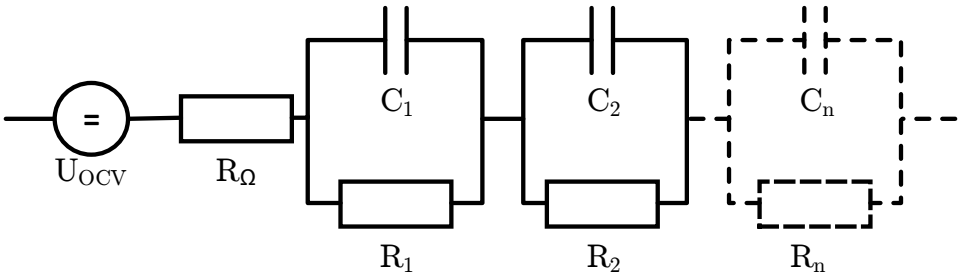

Figure 4.3.: Equivalent electric circuit according to [24]

A method to evaluate battery characteristics is the electrochemical impedance spectroscopy (EIS), where an AC voltage source is applied to the cell and the system response at different frequencies ω is measured. The voltage and current measurements are then analyzed and the impedance characteristics can be plotted in a Nyquist plot. The real part of the impedance is plotted on the X-axis and the imaginary part is plotted on the Y-axis, which results in semi-circles as exemplarily represented in Figure 4.4. The resistance values can be read from the real axis of the plot. It has been described in [24]

that the most accurate way to extract the ohmic resistance R_Ω is to take the minimal value of the measured real part, which is typically located at high frequencies near the intersect of the resistance curve with the $RE(Z)$ axis. The inner resistance is strongly depended on the capacity, size and current state of the cell [21, 24].

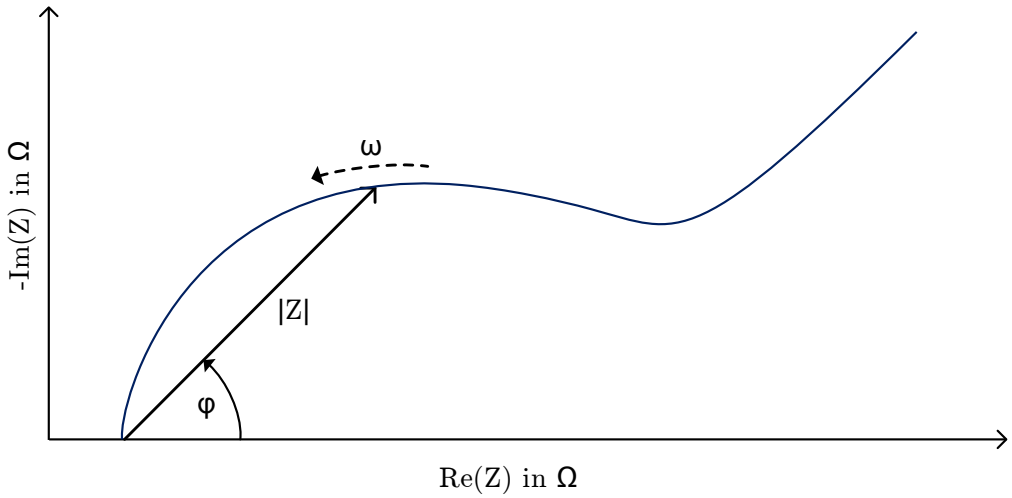

Figure 4.4.: Exemplary Nyquist plot according to [24]

Another method for measuring the inner resistance is the pulse current measurement. The cell receives a charge or discharge current pulse for several seconds and the voltage is measured. The test is typically conducted at different temperatures an SOC levels. Figure 4.5 depicts exemplary current and voltage curves for a discharge pulse test. The inner resistance can be calculated by employment of Ohm's law:

$$R_{Cell} = \frac{\Delta U}{I} \tag{4.1}$$

The internal resistance strongly depends on the length of the load pulse. For longer pulse duration, the RC elements depicted in Figure 4.3 have increasing shares in the resistance definition. Internal resistance measurements using the pulse current method on a commercial 50 Ah lithium-ion

cell were conducted at AVL. The impedance for a 1C discharge and charge current pulse at 50% SOC results in 1.52 $m\Omega$. This value will be referred to as inner cell resistance R_{Cell} throughout this study.

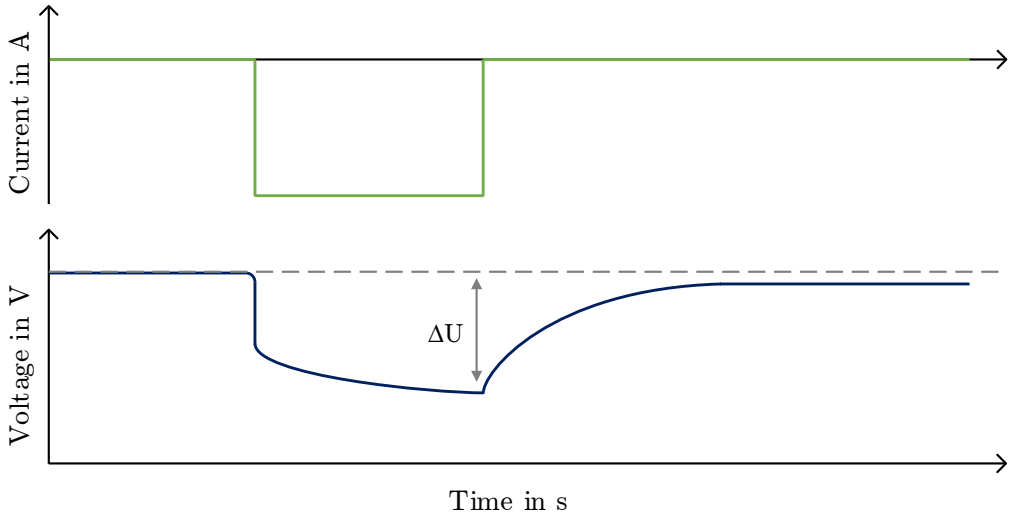

Figure 4.5.: Current charge pulse and voltage drops over time according to [24]

4.3.3. Losses

Current commercially available electric vehicles have battery capacities up to 90 kWh. For a fair comparison of all three voltage levels, a maximum amount n of 360 cells have been considered for the battery pack. With the cell data given in Table 4.1, this results in an equivalent nominal battery energy content of 67 kWh for all three voltage levels. The cells connected in series were chosen to be a multiple of 10, as this is a common amount of cells that are grouped into a module [7]. With a connection of 90, 180, and 360 cells in series for voltage level 1, 2, and 3 respectively, the amount of cells in parallel p_i necessary to reach the total amount of cells n can be calculated as:

$$p_i = \frac{n}{s_i} \tag{4.2}$$

where s_i represents the amount cells in series and index i indicates the voltage level. The total cell resistance for the cell configurations of each voltage level can be calculated as follows:

$$R_i = \frac{s_i R_{Cell}}{p_i} = \frac{s_i^2 R_{Cell}}{n} \tag{4.3}$$

The results are summarized in Table 4.2.

Table 4.2.: Cell resistance

Voltage level	Cells in series	Cells in parallel	Total amount of cells	Pack energy content in kWh	Sum of cell resistance in mΩ
1	90	4	360	67	34
2	180	2	360	67	137
3	360	1	360	67	547

Under the assumption that the power demand P of the vehicle is equal for each voltage level i, the current demand I_i can be calculated as:

$$I_i = \frac{P}{U_i} = \frac{P}{s_i U_c} \tag{4.4}$$

where U_i represents the battery pack voltage and U_cell a single cell voltage. The power losses caused by the inner cell resistances can be expressed as:

$$P_{Losses,i} = I_i^2 R_i \tag{4.5}$$

Considering equation 4.3 and 4.4 the power losses by the cells can be rewritten as:

$$P_{Losses,i} = \left(\frac{P}{s_i\, U_c}\right)^2 \frac{s_i^2\, R_{Cell}}{n} = \left(\frac{P}{U_c}\right)^2 \frac{R_{Cell}}{n} \tag{4.6}$$

It can be stated that the power losses are equal for all voltage levels with consistent power demand P and only depend on the cell characteristics and the total amount of cells n used. The series and parallel cell configuration shows no effect on cell resistance losses. The cell losses for the WLTP and CADC drive cycle RMS power demands are shown in Table 4.3.

Table 4.3.: Cell losses of WLTP and CADC

Drive cycle	RMS power demand in kW	Cell losses in W
WLTP	14.8	67.6
CADC	20.3	127.1

4.3.4. Balancing

Imbalances of battery cells are usual. The single cells have minor differences in internal impedance, self-discharge rate, and capacity. This results either from manufacturing variations or from unequal aging of the cell during operation. Later is caused by effects such as uneven temperature spread within the pack. When connected in series, the weakest cell determines the overall performance and charging or discharging has to be stopped when the lower or upper cell voltage limits (see chapter 4.1) are reached. Cell charge equalization, known as balancing, is necessary to compensate the imbalances. The necessary equalization elements are typically located in the CSC [25].
Different balancing approaches exist and are either passive or active. Passive balancing can be realized by switching a bleeding resistor in parallel to the cell for excess energy dissipation through generation of heat during battery charging. While cells with high capacity are still charging, the resistor is

switched on for low capacity cells to dissipate energy. Passive balancing is easy to implement but has an influence on battery cooling caused by the additional heat generation. The amount of resistors needed increases with an increasing amount of cells connected in series and therefore with increasing system voltage.
Active balancing realizes charge equalization through shuttling methods through capacitors or inductors. Charge is shuttled between individual cells or group of cells. Active balancing methods are more efficient than passive approaches but are more complex in design and control [11]. Figure 4.6 depicts example circuits for passive and active balancing.

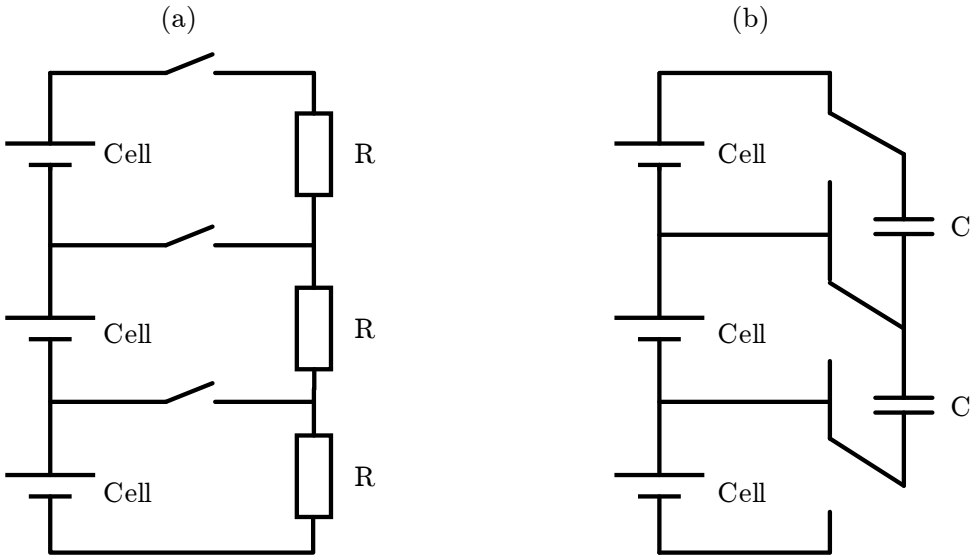

Figure 4.6.: Passive (a) and active (b) balancing circuit examples for 3 cells connected in series

With a higher system voltage level and more cells connected in series, the possibility of a weak cell increases. This results in more operation losses and lower cycling efficiency. The balancing losses also have to be taken into account when designing the system. Losses for passive balancing are about 18 W per module compared to 1.5 W for active balancing [7]. In addition,

the wiring effort for balancing increases with an increasing amount of cells in series.

4.4. HV connections

It has been discussed in chapter 4.2 that the battery pack consists of cell modules, switches, fuses, sensors, connectors, and other HV components. All these components are electrically interconnected by HV conductors. This is realized by either busbars or cables. Busbars are solid metallic strips or bars that are punched in form and usually electrical insulated (e.g. laminated). The preferred material for busbars and cables is copper due to its low electrical resistivity [11]. Cables are more flexible than rigid busbars and allow for more complex routing. However, multi-strand cables have a more complex manufacturing process and need connection elements such as crimp contacts [26]. The choice of the cross-section is determined by the current the conductor has to carry. Due to the Joule losses, the current causes the conductor to heat up. The heat produced is proportional to the square of the current: I^2R. A reduction of the current by half will therefore result in a quarter of the Joule losses. For the same system power demand, the current decreases linearly with increasing voltage as discussed in chapter 1. This leads to significant conductor cross-section reduction for higher system voltages, which has a beneficial impact on size, weight and costs.

4.4.1. Thermo-electrical behavior

In order to optimize size and weight of the HV connection, the thermo-electrical behavior must be understood. A mathematical model for describing the transient electro-thermal behavior of a conductor was therefor developed based on [26, 27]. This study presents a one-dimensional numerical model describing the Joule heat transfer from the inside of the conductor to the surrounding air. In general, busbars have a rectangular and cables a circular cross-section. When considering equal cross-sections and length, rectangular busbars offer a greater surface than cylindrical cables and are therefore able to transfer more heat to the surrounding air by convection.

Due to worst-case considerations and due to simplicity of the mathematical model, only a cylindrical cable has been considered in this study.

Method and assumptions

Several assumptions have been made to simplify the mathematical model: Heat is generated in the conductor as a result of power losses through the electrical resistance. The multi-strand cable is represented by a single conductor of equivalent cross-section. The conductor is assumed to be symmetrical along the longitudinal axis. In this work, the transferred heat along the axial axis of the conductor is neglected. Figure 4.7 shows the thermal network for a cable including the joule heat losses $\dot{Q}_{losses}$, thermal capacities C_{th}, thermal conductivities G_{ij} from node i to j, and conduction through convection G_{conv}.

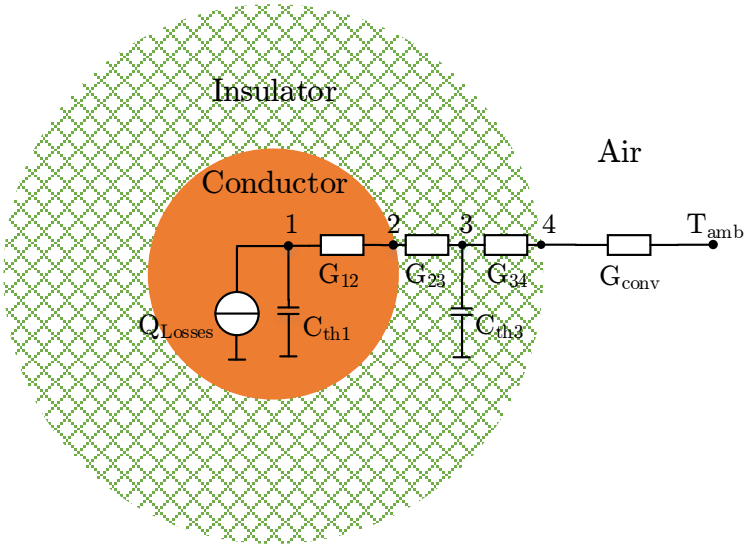

Figure 4.7.: Thermal model of a cable with insulator adapted from [27]

The nodes 1 to 4 represent temperatures at different interfaces. Node 1 to 2 shows the heat conduction within the conductor. The interface between

conductor and insulation is represented by node 2. Node 4 describes temperature on the insulator surface. It is assumed that the conductor is placed in still air (no significant air currents) with a constant temperature T_{amb}. The thermal energy at the outer surface of the conductor is lost to the surrounding air through free convection. Heat conduction through air and radiation are neglected due to simplicity of the model. The thermal model shown is also valid for busbars. In this work, busbar and cable differ only in the representation of the surface: The heat flux is conducted to the outer surface radially for a cable or through its sides, top and bottom for a busbar.

The initial boundary conditions of the system are available: The initial conductor is at known ambient temperature T_{amb} of 25°C. The ambient temperature of the air remains constant (Dirichlet condition) and a temperature time derivative equal $\frac{dT}{dt}$ to zero for the external node (homogeneous Neumann condition). Including the external node with temperature T_{amb}, the $N-1$ nodes system can be represented by the following heat equation:

$$\mathbf{G_{ij}} \cdot \mathbf{T_i} + \dot{\mathbf{Q}}_\mathbf{i} = \mathbf{C_{ij}} \cdot \frac{\mathrm{d}\mathbf{T_i}}{\mathrm{d}t} \tag{4.7}$$

The conductance matrix $\mathbf{G_{ij}}$ includes heat fluxes by conduction and convection, $\mathbf{T_i}$ is a vector containing the unknown node temperatures. Vector $\dot{\mathbf{Q}}_\mathbf{i}$ describes the heat sources (Joule losses) and heat sinks (convection to surrounding air). The thermal densities as node 1 and 3 are represented by the heat capacity matrix $\mathbf{C_{ij}}$. With vector $\mathrm{d}\mathbf{T_i}/\mathrm{d}t$ the transient temperature changes are taken into account [26, 27, 28].

The material chosen is copper for the conductor and PVC for the insulator. Table 4.4 lists the material characteristics.

Losses

The conductor is supplied by a DC current that causes the copper to heat up due to Joule losses. With the known length l, cross-section A, resistivity ρ, temperature T, and temperature coefficient α the temperature-dependent resistance of the conductor can be calculated:

Table 4.4.: conductor and insulation characteristics according to [26, 27]

Property	EPT Copper	PVC
Thermal conductivity in W/mK	385	0.17
Specific heat capacity in J/kgK	385	960
Density in kg/m^3	8890	1760
Specific resistance 20°C in $\Omega mm^2/m$	$1.7{\cdot}10^{-2}$	-
Temperature coefficient at 20°C	0.00393	-

$$R_{20} = \rho \cdot \frac{l}{A} R = R_{20} \cdot (1 + \alpha \cdot (T - 20)) \tag{4.8}$$

The heat losses $\dot{Q}_{Losses}$ are proportional to the square of the current:

$$\dot{Q}_{Losses} = I^2 R \tag{4.9}$$

Heat conduction

Heat is transferred in materials through heat conduction. The heat flux $\dot{Q}_{Conduction}$ for a volume with cross-section A, length l, and the thermal conductivity λ is proportional to the change of temperature along the radius r for a cable:

$$\dot{Q}_{Conduction} = -\lambda \, A \, l \, \frac{\mathrm{d}T}{\mathrm{d}r} \tag{4.10}$$

For a cable the thermal resistance is a function of the geometry. The heat flux from radius R_{inner} to R_{outer} can be expressed by:

$$\dot{Q}_{Conduction} = -\frac{2\pi l \lambda}{ln(R_{outer}/R_{inner})} (T_{outer} - T_{inner}) \tag{4.11}$$

The heat conductivity λ is a temperature-dependent material property that is defined by experimental studies [29]. Within this work, the heat conductivity is assumed to be constant.

The conductance is then given by:

$$G_{Conduction} = -\frac{2\pi l\lambda}{ln(R_{outer}/R_{inner})} \tag{4.12}$$

At node 1, where the conductor radius equal to zero, the thermal conductance can be expressed by:

$$G_{Conduction} = -4\pi l\lambda \tag{4.13}$$

Heat convection

At the interface between the solid conductor insulation and the gaseous air, the heat is transferred by convection. In this study, free convection is considered. For the insulation surface area $A_{surface}$ the heat loss by convection can be described as

$$\dot{Q}_{convection} = h_c\, A_{surface}\, (T_{ambient} - T_4) \tag{4.14}$$

where h_c represents the convection coefficient. The thermal conductance for free convection can now be expressed:

$$G_{convection} = h_c\, A_{surface} = h_c\, 2\pi rl \tag{4.15}$$

In order to simplify convection, the usually temperature-dependent convection coefficient h_c is assumed to be constant. The value for free air is chosen to be $8\,W/m^2K$ according to [30]. For busbars more heat can be transferred to the surrounding air by convection, as the rectangular surface is larger than a cylindrical when considering the same cross-section.

Heat capacity

With the heat capacity C_{th} of the conductor and insulator, the transient thermal behavior of the cable can be considered:

$$\dot{Q}_{th} = C_{th} \frac{\mathrm{d}T}{\mathrm{d}t} \tag{4.16}$$

The heat capacity is a function of the material geometry and properties: For a conductor with cross-section A, length l, the density ρ, and the specific heat capacity c_p.

$$C_{th} = A\, l\, \rho\, c_p \tag{4.17}$$

Numerical calculation

The heat equations 4.21 for $N-1$ nodes (node 1 to 4 in Figure 4.7) can now be defined and composed into a matrix system:

$$\begin{bmatrix} G_{11} & -G_{12} & 0 & 0 \\ -G_{21} & G_{22} & -G_{23} & 0 \\ 0 & -G_{32} & G_{33} & -G_{34} \\ 0 & 0 & -G_{43} & G_{44} \end{bmatrix} \cdot \begin{bmatrix} T_1 \\ T_2 \\ T_3 \\ T_4 \end{bmatrix} + \begin{bmatrix} \dot{Q}_1 \\ \dot{Q}_2 \\ \dot{Q}_3 \\ \dot{Q}_4 \end{bmatrix} = \begin{bmatrix} C_1 & 0 & 0 & 0 \\ 0 & 0 & 0 & 0 \\ 0 & 0 & C_3 & 0 \\ 0 & 0 & 0 & 0 \end{bmatrix} \cdot \begin{bmatrix} \mathrm{d}T_1/\mathrm{d}t \\ \mathrm{d}T_2/\mathrm{d}t \\ \mathrm{d}T_3/\mathrm{d}t \\ \mathrm{d}T_4/\mathrm{d}t \end{bmatrix} \tag{4.18}$$

The conductance matrix $\mathbf{G_{ij}}$ is symmetric, which means $G_{ij} = G_{ji}$. For the diagonal elements, the equation $G_{ii} = \sum_{j=1}^{N-1} G_{ij}$ holds true.

The temperatures at the current temperature T^i and a later one T^{i+1} can be calculated numerically with

$$\frac{\mathrm{d}T_i}{\mathrm{d}t} = \frac{T^{i+1} - T^i}{\Delta t}, \tag{4.19}$$

where Δt represents a small time step.

Equation 4.18 can be solved numerically with various methods such as Euler and Runge Kutta [26]. The method chosen in this study is the implicit Backward Euler method, where T^{i+1} is unknown:

$$\mathbf{G_{ij}T^{i+1}} + \dot{\mathbf{Q}}_\mathbf{i} = \mathbf{C_{ij}} \cdot \frac{\mathbf{T^{i+1}} - \mathbf{T^i}}{\Delta t} \tag{4.20}$$

Finally, this equation transforms into:

$$\mathbf{T^{i+1}} = (\mathbf{C_{ij}} - \mathbf{G_{ij}}\Delta t)^{-1}(\dot{\mathbf{Q}}_\mathbf{i}\Delta t + \mathbf{C_{ij}T^i}) \tag{4.21}$$

The equation system was solved using text-based script in MATLAB. The script can be found in Appendix C.

4.4.2. Thermal simulation results at different voltage levels

The currents resulting from the CADC profile (see Table 2.3) for the three defined voltage levels have been considered for thermal analysis. It has to be noted, that only RMS currents were used for simulation. Higher cable temperatures for transient current peaks are expected. The initial conductor temperature equals the assumed constant ambient temperature of the free surrounding air. It has been described that the maximum ambient temperatures acceptable within battery packs are 70°C [7]. Due to the expectation of temperature peaks for transient currents, a safety-margin of 20°C was chosen. The cross-sections of the conductors have therefore been chosen so that the insulation surface temperatures stays below 50°C. For the defined voltage levels, Table 4.5 lists the required cross-sections and insulation wall thicknesses based on HV cables commercially available [31]. With a decreasing wall thickness for thinner cables, the maximum voltage the insulator can withstand also decreases. Too thin wall thicknesses may be inadequate for higher voltage levels and need to be verified for possible dielectric breakdown. The simulation was conducted with per-meter cable lengths.
Figure 4.8 shows the transient simulation results of the conductor and

insulation surface temperature. Steady state temperatures are considered at 2000 s, where no further significant change in temperature can be observed. The steady state is reached faster for cables with smaller cross-sections and thinner wall thicknesses. The following list summarizes the described simulation boundary conditions:

- The RMS power from the CADC drive profile was used
- Nominal voltages were used for RMS current calculation
- Cable temperatures should stay below 50°C
- 25°C were chosen for start and ambient temperature temperature
- Per-meter values were considered for the simulation ($l = 1\,m$)

Table 4.5.: Transient thermal behavior of a cable at different voltage levels and currents

Voltage level	Nominal voltage in V	RMS Current in A	Conductor cross-section in mm^2	Insulation wall thickness in mm
1	350	57.9	18.0	0.80
2	650	28.9	8.0	0.64
3	1350	14.5	3.0	0.58

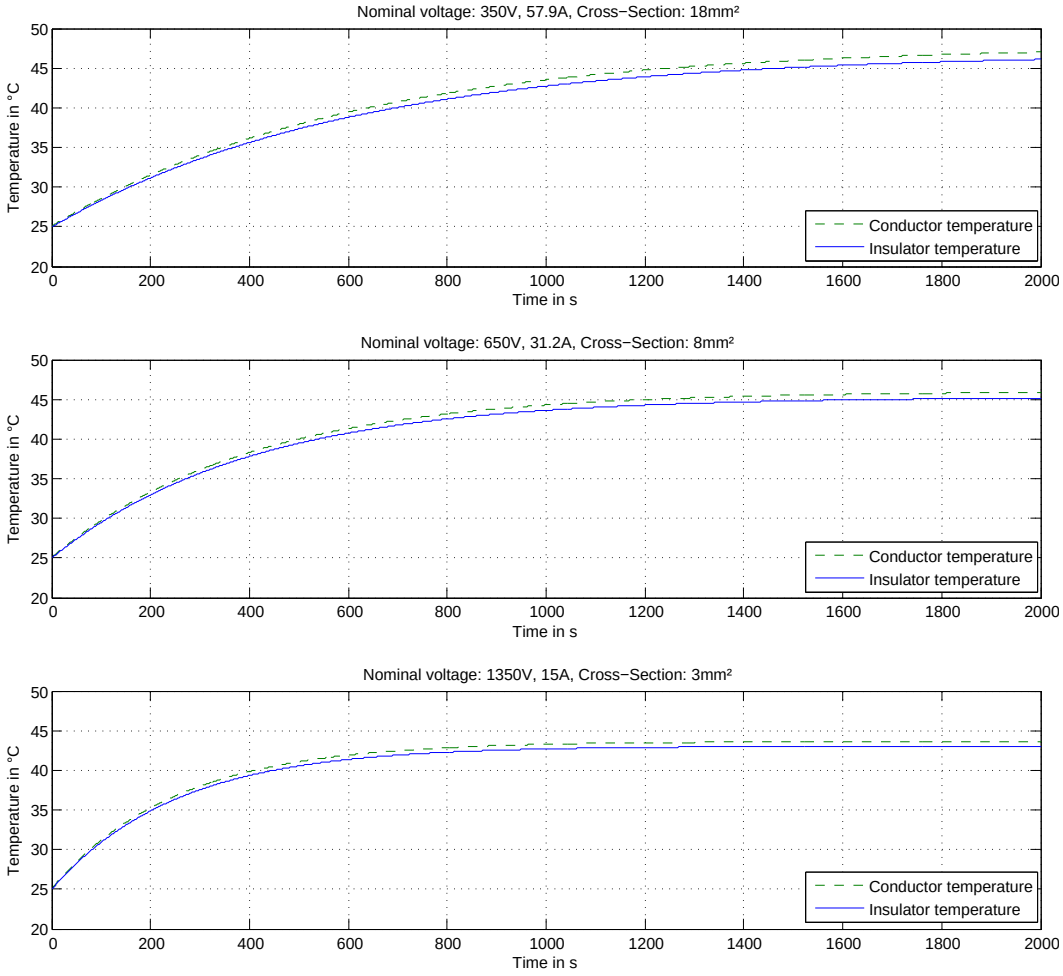

Figure 4.8.: Simulation results for surface temperatures of cables

Table 4.4 summarizes the results of the thermal analysis and compares the thermal behavior at different voltage levels and resulting currents. The properties of the cable (current density, weight, resistance, power losses) for voltage level 2 and 3 are compared to those of voltage level 1. The weight of the conductor can be reduced by 54% for system voltage level 2 compared to the weight for the cable used at voltage level 1. The weight decrease from voltage level 1 to voltage level 3 flattens out to 81%. The resistance at the steady-state increases by 124% and 493% for voltage level 2 and 3

respectively compared to the resistance of voltage level 1. The steady-state power losses decreases by 35% and 60% for voltage level 2 and 3 respectively compared to the power of voltage level 1.

Table 4.6.: Thermal simualtion per-meter results for cable with PVC insulation, voltage level 1 as reference

Voltage level	1	2	3
Nominal voltage in V	350	650	1350
RMS Current in A	57.9	31.2	15.0
Cross section in mm^2	18.0	8.0	3.0
Steady state temperature conductor in °C	47.0	45.9	43.6
Steady state temperature insulation in °C	46.1	45.2	43.0
Current density in A/mm^2	3.2	3.9	5.0
Increase in current density	ref.	21 %	55 %
Cable weight in g/m	186.2	85.2	34.7
Reduction in weight	ref.	54%	81%
Resistance in mΩ/m	1.0	2.3	6.2
Increase in Resistance	ref.	124 %	493%
Power losses in W/m	3.5	2.3	1.4
Reduction of power losses	ref.	35%	60%

The results for current density, weight, steady-state resistance, and steady-state power losses of the cable at different voltage levels and resulting

currents are also shown in Figure 4.9. As the required current decreases with higher voltage levels, the required current density and the resulting resistance of the conductor increase almost linearly. It can be clearly seen that the decreases in weight and power losses tend to flatten out at higher voltage levels. In conclusion, when targeting a certain cable surface temperature, raising the system voltage level results in decreasing weight and power losses of the cables. However, these benefits flatten out with higher system voltages.

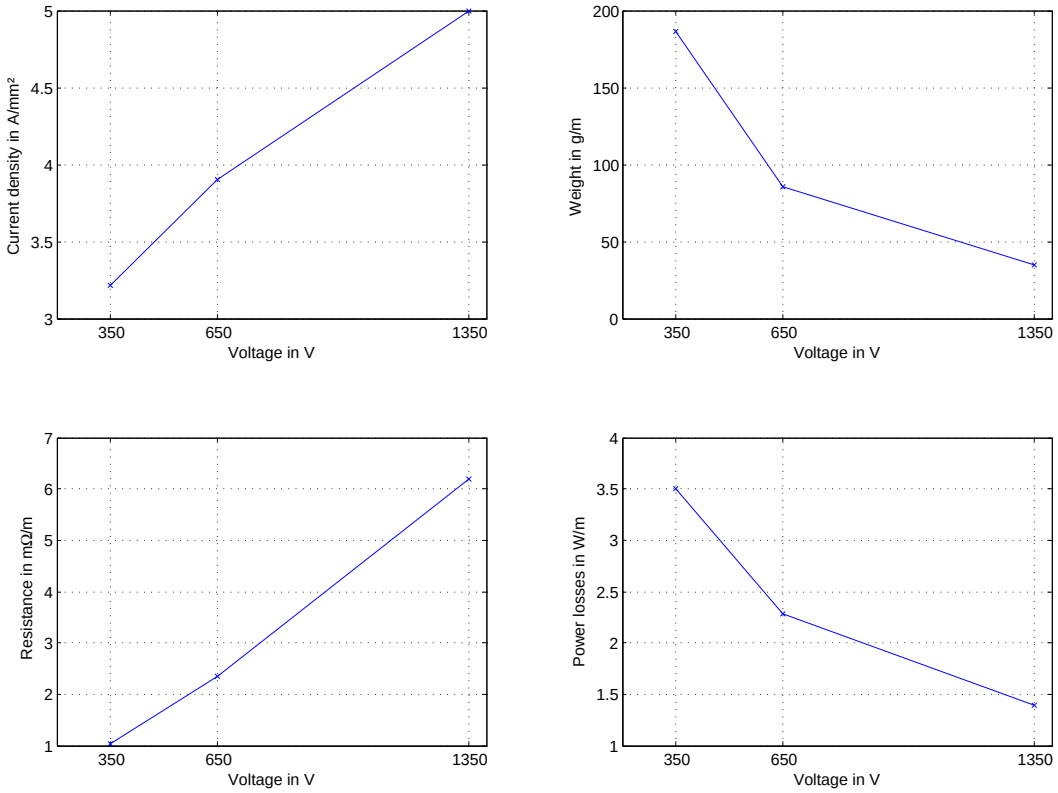

Figure 4.9.: Cable Current density, weight, steady-state resistance, and steady-state power losses at different voltage levels and resulting currents

4.4.3. Replacing copper by aluminum

A trend that can be observed for electric vehicles is the replacement of copper by aluminum. The two materials are most commonly used for cables and busbars in electric equipment [32]. Aluminum has a lower conductivity than copper but has the benefit of significant lower weight [26]. This makes it attractive for the usage in electric vehicles. In order to achieve the same conductivity, aluminum must be larger in volume by the ratio 1.6 compared to copper. For the same heat capacity, the ratio results in 1.4. Comparisons between Copper (Cu-ETP) and Aluminum (E-Al 99.5) for the same conductivity and for the same heat capacity are given in Table 4.7:

Table 4.7.: Comparison between copper and aluminum

	Cu-ETP	:	E-Al 99.5
Same conductivity:			
Resistance	1	:	1
Cross section	1	:	1.6
Surface	1	:	1.25
Weight	1	:	0.3
Heat capacity	1	:	0.17
Same heat capacity:			
Heat capacity	1	:	1
Cross section	1	:	1.4
Surface	1	:	1.17
Resistance	1	:	1.1
Weight	1	:	0.4

Figure 4.10 depicts the conductor mass comparison of copper and aluminum with same conductivity and same heat capacity for equivalent copper cross-sections up to 100 mm^2.

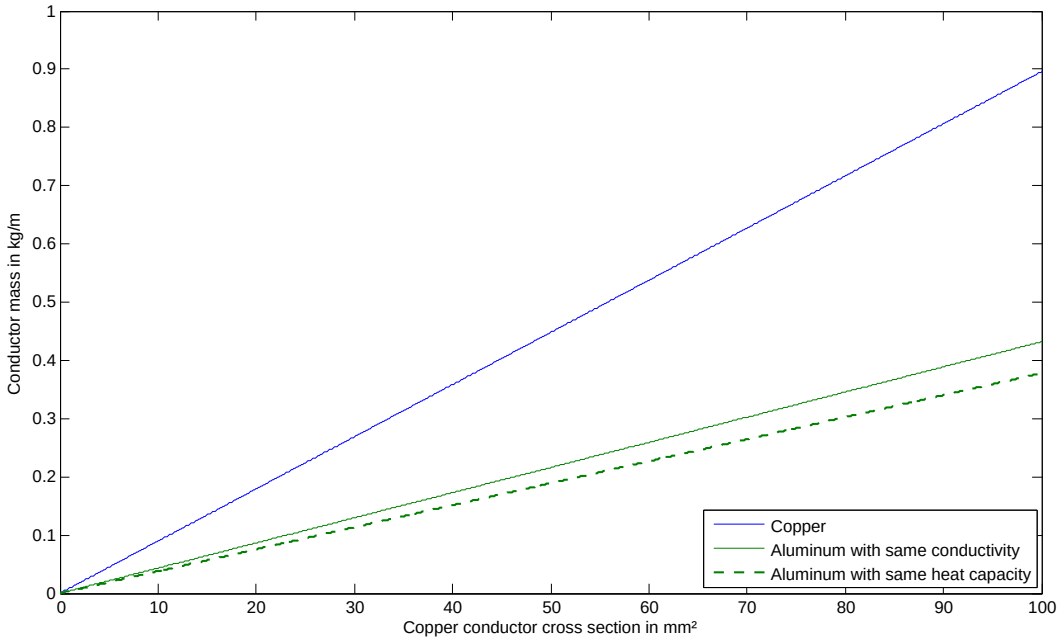

Figure 4.10.: Comparison between copper and aluminum with same conductivity and same heat capacity for copper cross section, adapted from [26]

Aluminum also has drawbacks compared to copper. The higher volume of aluminum (ratio 1.6) is a main disadvantage, especially when packaging space is tight in battery packs. Another disadvantage of the material is the appearance of an oxide layer on its surface. Especially for joints, oxidation must be minimized by plating the aluminum conductor with materials such as tin or silver. Bolted connections of unplated aluminum to copper conductors is discouraged due to electro-chemical corrision [32].

4.4.4. HV connectors and terminals

HV connectors and terminals interconnect the HV components inside the battery. Connectors further provide an interface from the battery pack to vehicle components such as the inverter or the on-board charger. German

automotive manufacturers have bundled the requirements for HV connectors and terminals in the supplier regulation LV 215-1. Some important connector specifications are listed below:

- Maximum voltage of 850 Vdc
- Ambient temperatures from -40°C to 140°C
- Touch protection complying to IP2XB (VDE-Finger) when in mated condition
- Color coded orange
- HVIL signal path for emergency shut-off
- Shielding connection with a contact resistance less than 10 mΩ
- Water-tightness in mated condition complying to IP6K9K, IPX7 (refer to Appendix A)
- Air- and creepage distances according to IEC 60664-1 [13]
- Withstand voltage and insulation resistance according to ISO 6469-3 [4].

Although the maximum voltage is specified with 850 Vdc in LV 215-1, connectors with maximum voltages of 1000 Vdc are commercially available [33]. Connectors for voltages up to 1500 Vdc are currently not available for automotive usage.
Peak ambient temperatures of up to 140°C near the connector can be expected in specific load cases. Connectors are color coded orange. This coding indicates the danger of high voltage and the possible risk of an electric shock. In order to achieve touch protection IP2XB in unmated condition, design measures are required. These can include high enough walls, that prevent touching the HV contacts.
HV connectors usually have a HVIL integrated for safety means. The BMS is constantly evaluating the HVIL signal. When unplugging the connector during vehicle operation, the HVIL path breaks and the BMS subsequently shuts the battery system down.
EMC shielding becomes more difficult with higher voltages and higher currents. The contact resistance needs to be less than 10 mΩ over the entire lifetime of the battery. The shielding path of the connector is required to carry continuous currents up to 10 A and fault currents up to 25 A for 60 s [3, 7].

According to LV 215-1 HV, terminals and connectors can be sorted into 5 classes shown in Table 4.8. Connector variety can be reduced with this modular system of connector classes and different applications can be covered with less connectors.

Table 4.8.: HV connection classifications

Class	Cross-section in mm^2	Current in A at 125°C	Connection technology
1	2.5 to 4	25	Plug-in
2	4 to 6	40	Plug-in
3	6 to 16	80	Plug-in
4	16 to 50	200	Plug-in and terminal
5	70 to 120	400	terminal

4.5. Contactors

The main function of the high-voltage DC power contactors is to connect and disconnect the battery from the vehicle drive train. Usually two contactors are used to switch both, the positive and the negative HV path. This is done in order to achieve redundancy according to ISO 26262 (see section 3.1), a homogeneous switching behavior, and to guarantee a complete galvanic separation of the battery from the rest of the system. When the vehicle is started, the contactors switch the battery to the rest of the system based on the commands from the BMS. The contactors remain closed during driving and disconnect the battery after the vehicle is turned off again. Under normal operating conditions the system is switched without load. The contactors usually have to withstand about 500,000 mechanical switching cycles [34]. The switch gear in electric vehicles has to meet hard requirements with regard to volume, power losses and weight [7, 35].

4.5.1. Component tasks

Conduction

During system design, contactors need to be chosen that are capable to conduct all system currents that can occur during operation without any damage with the worst-case being a short circuit. In electric vehicles, short-circuits can be in the range of 16-times the nominal current. In that case, the switch needs to remain closed and conduct the fault current until the protective fuse breaks the high voltage circuit in the time range of 40 ms to 100 ms. If the contactor opens during short-circuit it will be thermally overloaded and destroyed. During conduction, the contact resistance of the contacts is preferably low to minimize I^2R losses [35].

Make and break

During switch-on (referred to as "make"), contact surface stresses are reduced by limiting inrush currents through a pre-charge circuit, which is described in detail in chapter 4.7. During switch-off (referred to as "break"), the contactor disconnects the battery from the rest of the vehicle. Under normal operating conditions, only minimal currents that will not lead to contact arcing need to be interrupted as the vehicle power electronics typically disconnects before the contactors open.

In the event of a fault (e.g. crash) the battery needs to be disconnected from the system immediately by switching off under load. Depending on the system structure, time constants up to 1 ms need to be taken into account [35]. During switch-off under load, phenomena such as contact erosion, contact welding, and arc movement need to be considered. In such faulty situations the feasible number of switching operations reduces to a only a few depending on the electrical load.

Polarity

The polarity needs to be considered during switch-off, as arc-distinguishing mechanisms are usually polarity-depended as described in chapter 4.5.3. System faults can also occur during charging or recuperation.

Galvanic separation

When not actuated, the contactors ensure a galvanic separation of the HV battery from the drive train. The clearance distances (see section 3.2.2) inside the switchgear need to be chosen to ensure proper insulation.

4.5.2. Structure

Figure 4.11 shows the structure of a typical contactor that is used in electric vehicle applications. The actuating part is composed of a solenoid and a moveable ferromagnetic core. Once voltage is applied (usually 12 V or 24 V), the magnetic force is higher than the spring force and actuates the core to move up. The HV path is now closed over the movable and stationary contacts and current flow is encouraged. After the solenoid voltage is switched off, the return spring moves the core down and the contactor maintains in an open position until actuated again. In automotive high-voltage DC contactors, two permanent blowing magnets (not shown in Figure 4.11) are usually embedded in the contact chamber. The magnetic field produced by magnets are blowing the switching arc to the left or right for arc extinguishing. This mechanism is elaborated in detail in chapter 4.5.3.

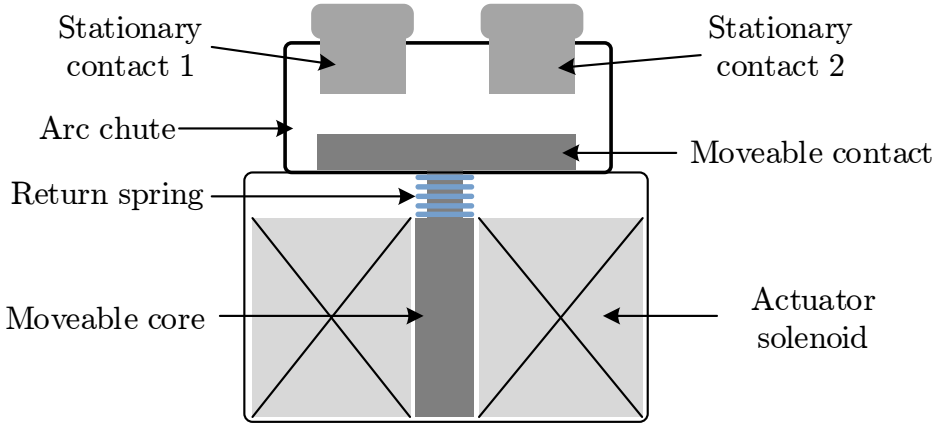

Figure 4.11.: Structure of contactor

The arcing chute is often hermetically sealed and filled with hydrogene (H_2). The gas offers a higher heat capacity and higher dielectric strength than air. This ensures the formation of high arc voltages for faster arc-quenching. H_2 also has drawbacks as the gas carries the risk of a potential explosive reaction. Open air-filled chambers are also possible in automotive contactors but must have sufficiently large arching chambers [36].

In this work, the focus is laid on the HV path and the HV contactor switching mechanisms. The system voltage level usually does not have major impact on the electromagnetic mechanism of the LV solenoid actuator, which will therefore not be further discussed.

4.5.3. Arc suppression at different voltage levels

When DC contactors are opened under load, the I^2R losses on the contacts (anode and cathode) lead to hot spots on the contacts that are eventually melting. Contact material transfers from cathode to anode. The air in the gap between the contacts is super heated and begins to ionize. The metallic ions and the ionized channel between anode and cathode begin to conduct electrons and form an electric arc. Only if the current is high enough will the arc contain sufficient energy to sustain itself. The arc maintains a low

voltage drop and behaves like a non-linear resistor. Figure 4.12 shows the principle voltage and current curves during contactor switch-off.

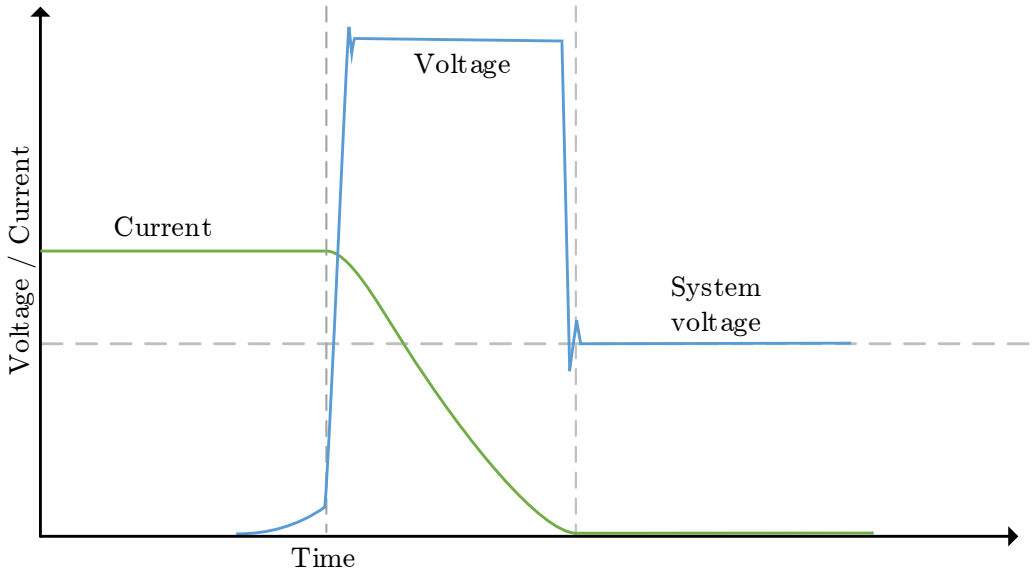

Figure 4.12.: Voltage and current curve during contactor switch-off adapted from [37]

When considering an DC circuit with voltage source U, resistance R and inductance L, and arc voltage u_{arc} as represented in Figure 4.13 the following mash equation can be defined:

$$U = L\frac{di}{dt} + R \cdot i + u_{arc} \tag{4.22}$$

The current i must be forced to zero in order for the electric arc to extinguish:

$$\frac{di}{dt} = \frac{U - R \cdot i + u_{arc}}{L} < 0 \tag{4.23}$$

$$u_{arc} > U - R \cdot i \tag{4.24}$$

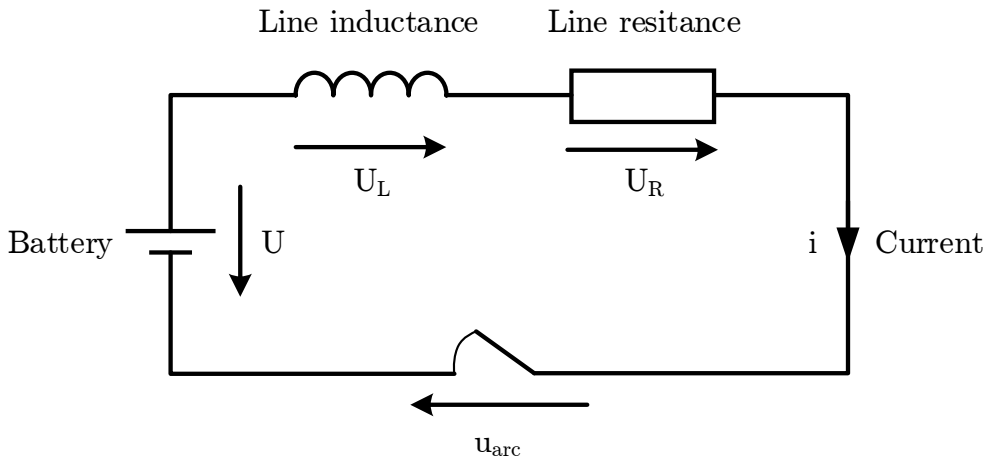

Figure 4.13.: DC circuit during contactor switch-off according to [38]

When the arc voltage rises above the system voltage, the current drops until finally the arc extinguishes [37]. Hence, a fast rising arc voltage is indispensable for an effective DC interrupter. Otherwise the arc will remain burning and the heat stresses the switchgear until destruction. The switching capacity of a contactor is limited by the thermal capacity of the arc chute. Minimization of the thermal stress caused by the power losses and the duration of the arc are necessary [35, 36].

The arc voltage u_{arc} can be described by the following equation:

$$u_{arc} = U_{anodefall} + E_{gap} \cdot l_{arc} + U_{cathodefall} \tag{4.25}$$

$U_{anodefall}$ and $U_{cathodefall}$ are the anode and cathode fall voltages respectively. E_{gap} is the electric field strength of the gap between the contacts, and l_{arc} represents the length of the arc. During switching under load, the arc voltage rises up to 2 to 4 times the system voltage [36, 39].

During current interruption, the energy stored in the circuit load inductance has to be dissipated in the switching arc chamber:

$$W_{inductance} = \frac{1}{2} L I^2 \tag{4.26}$$

Under the assumption of equal inductance values for all voltage levels, the energy stored in the inductance is lower for higher voltages due to reduced currents. Consequently, less energy has to be dissipated in the contactor chute for higher system voltages. The arc duration however, depends on several parameters such as the arc voltage level u_{arc}, time constant τ, and the geometrical properties of the contactor.

Mainly two principles are used for arc quenching: active arc lengthening and cooling. The contactor blowing mechanism lengthens the arc for higher voltages and the surrounding gas and the chamber walls cool the arc.

Arc lengthening

The arc can be lengthened by magnetic deflection. Two permanent magnets are set besides the contact to blow the arc in the direction of the Lorentz force $\mathbf{F}_L$:

$$\mathbf{F}_L = I(\mathbf{l}_{arc} \times \mathbf{B}) \tag{4.27}$$

Two magnets ensure a more homogeneous magnetic flux $\mathbf{B}$, as can be seen in Figure 4.14. The arc duration decreases with the increment of the flux density as described in [40].

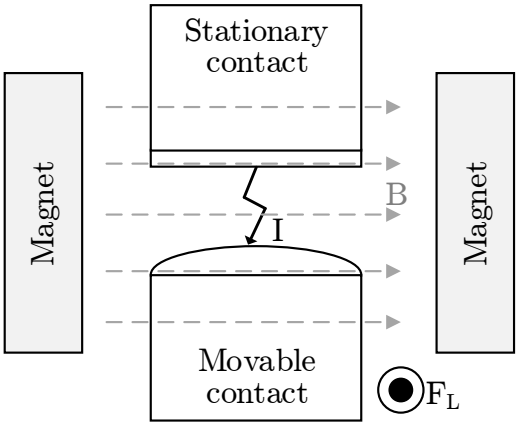

Figure 4.14.: Blowing magnet principle

Arc cooling

The arc chute can be hermetically sealed and filled with gas such as H_2. The gas has a higher dielectric strength and higher heat capacity than air. The arc energy is therefore reduced effectively by cooling the arc. As H_2 molecules are small, the sealing of the arc chambers poses a challenge. The wall of the chamber can further cool the arc through heat conduction. Especially ceramic is used in automotive contactors. Figure 4.15 exemplary shows the arc time of a sealed and gas-filled contactor at 600V and 75A with a resulting arcing time of 1 ms [38].

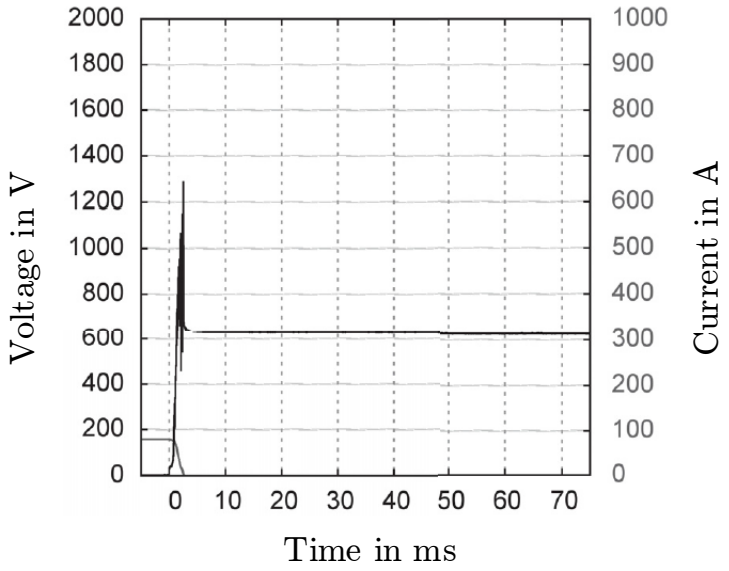

Figure 4.15.: Arc time of a sealed contactor with a system voltage of 600V and a current of 75A taken from [38]

4.5.4. Weight and size

In this study, 46 contactors that are commercially available for hybrid and electric vehicles were analyzed in terms of weight, size, maximal switching voltage, and nominal switching current. Figure 4.16 shows the increase in weight and the volume for higher nominal switching currents. To carry and switch higher currents, the HV path need to be larger in size and weight as more copper is needed. More solenoid winding turns are needed to provide a sufficient magnetic force in order to lift the larger and heavier movable contact. Some contactor manufactures use an epoxy sealed instead of a ceramic chamber to further decrease weight [41, 42].

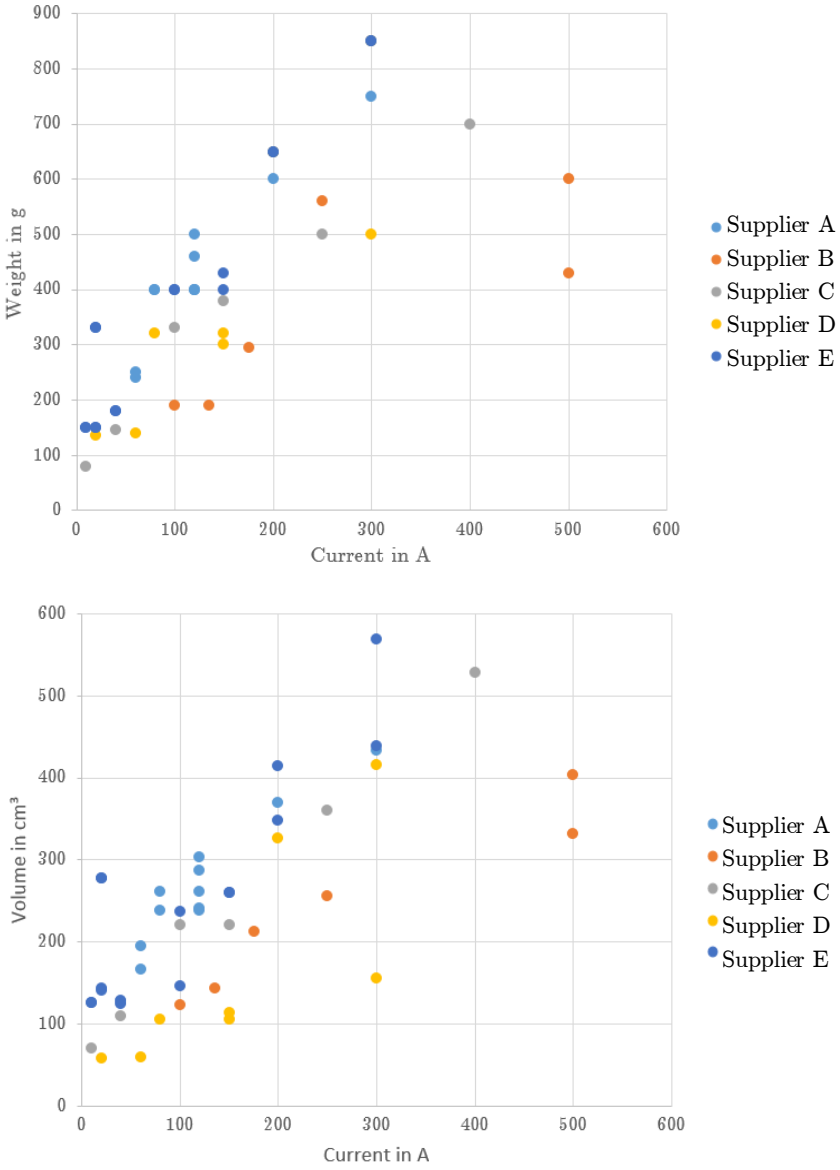

Figure 4.16.: Weight and volume of various contactors over their nominal switching current

It was found that 23 of the analyzed contactors are suitable for switching

more than 800 V according to the data sheets. The clearance and creepage distances, and the withstand voltage between the open contacts and between the HV and the LV path of those contactors are large enough to handle the higher system voltage. However, the higher switching voltage is also load-depended and need to be aligned with the switchgear supplier [34]. The weight mainly depends on current capabilities as can be seen in Figure 4.17 no correlation could be found between the weight or volume and the maximum switching voltage of contactors grouped at different nominal currents.

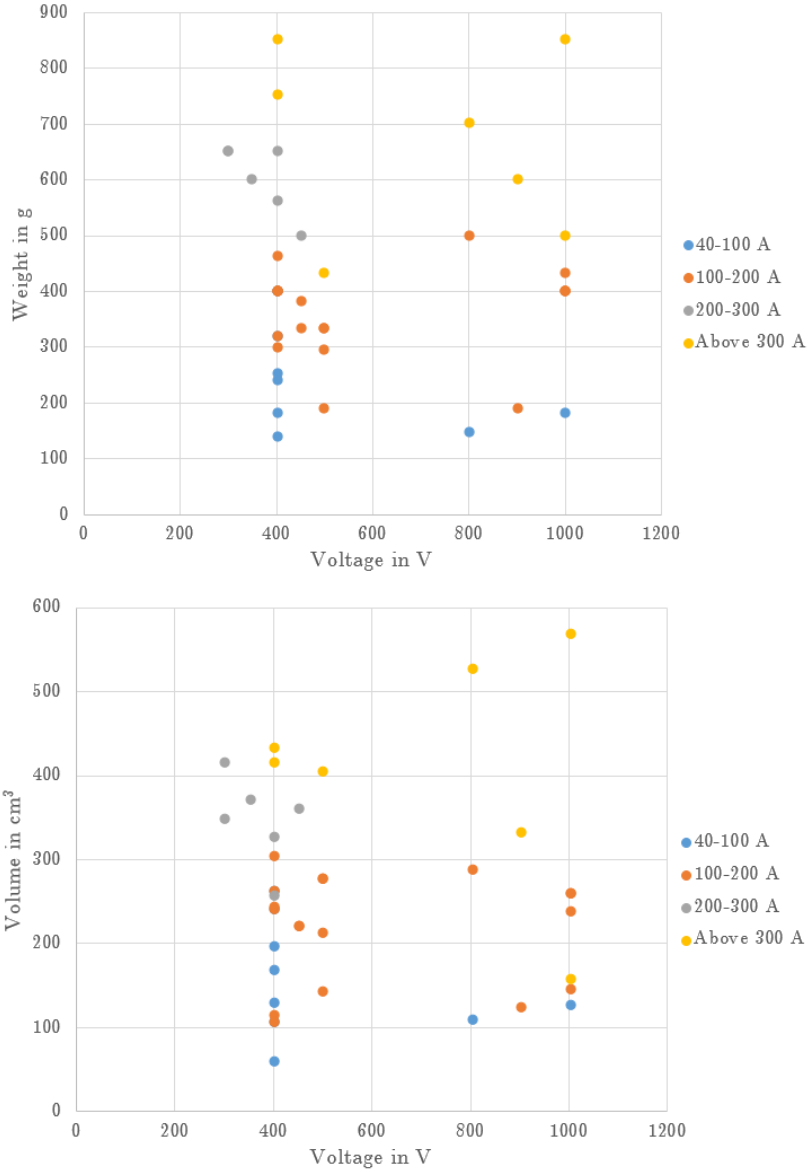

Figure 4.17.: Weight and volume of various contactors grouped into current ranges over their maximal switching voltage

There are currently no automotive contactors commercially available for switching voltages up to 1500 V. Contactors for such high DC voltages can be found for solar power production applications and stationary battery storage systems, which are not fulfilling the automotive standards [38].

4.5.5. Contactor alternatives

With an increasing system voltage up to 1500 V, special focus has to be laid on the design of arc quenching mechanisms to realize high DC voltage breaks [40]. One mechanism to increase the arc voltage is to use spitting plates. Iron plates are used to split the arc into shorter sub-arcs as shown in Figure 4.18. As this mechanism is commonly used in AC contactors but exhibits an obstacle for DC devices: the DC arc is hindered to move between the plates caused by its larger arc diameter. The optimization of the edges of the splitter plates is necessary to facilitate arc splitting [38].

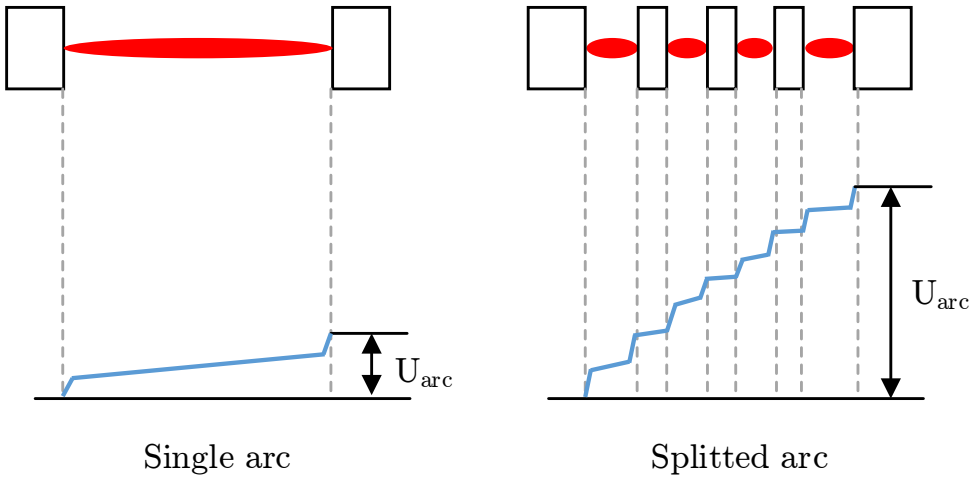

Figure 4.18.: Arc voltage for single and splitted arc adapted from [37]

Another approach to further decrease weight and size is the usage of hybrid switches. Such switches have a semiconductor (MOSFET or IGBT) connected

in series that switches the high voltage. The mechanical switch is solely used for switching without load and can be small in size and weight. The semiconductor however, creates additional losses during conduction [36].

4.6. Fuse

The system must be protected from currents the contactors are not capable to safely switch off. Such overcurrents and short-circuit protection is ensured by a fuse, which cuts off large fault currents.

4.6.1. Component tasks

Conduction

During normal operation of the system, the fuse has to carry the operating current without aging or early trigger. Thus, the fuse must be operated under its minimum breaking current.

Break

In the event of an overcurrent or short-circuit the fuse has to break the current. The breaking process is composed of a pre-arcing (melting) and arcing phase. If the thermal energy associated with the current is greater than the fuse can absorb, the fuse may explode [43].

4.6.2. Structure

The fuse typically consists of an current-carrying element that is surrounded by an arc-quenching filler such as silica sand. The element and the filler are enclosed in a ceramic fuse body. The element is soldered or welded to the fuse terminals that are usually bolted to the battery system HV path. Figure 4.19 shows the structure of a typical EV-fuse.

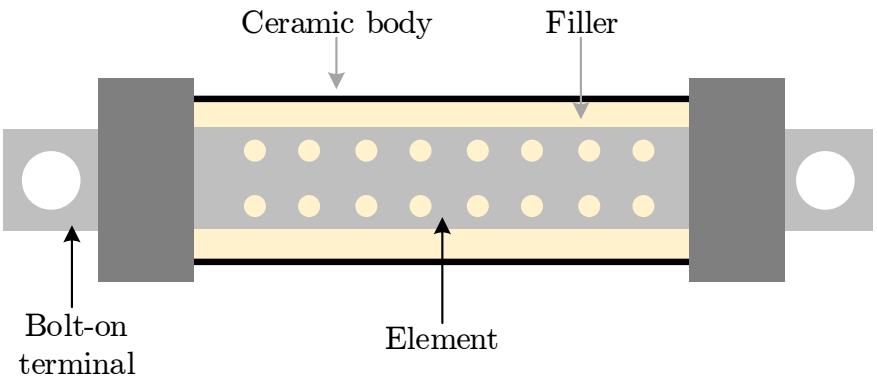

Figure 4.19.: Structure of fuse

The element contains holes — also called notches — for cross-section reduction. The resistance of the element is depended on its geometry and material, the connection to the end caps, the end caps, and the terminals. Depending on the load current, heat is generated by the element through Joule losses. The generated heat inside the fuse is conducted to the fuse body and to the surrounding air by the filler material. A ceramic body ensures a high dielectric strength and heat stability. In the event of an overload or short-circuit the element heats up faster than the filler is able to conduct heat away. The element will eventually melt at the notches and vaporize. Caused by the presence of battery line inductance the current is not able to fall to zero instantly, the voltage over the small gap rises and an electric arc forms between the open contacts. The filling sand then dissipates the arc energy until the current reaches zero and the arc extinguishes [43, 44].

4.6.3. Breaking behavior at different voltage levels

The breaking behavior of the fuse can be differentiated into a pre-arcing and an arcing period. A typical voltage and current curve of a fuse during breaking can be seen in Figure 4.20.

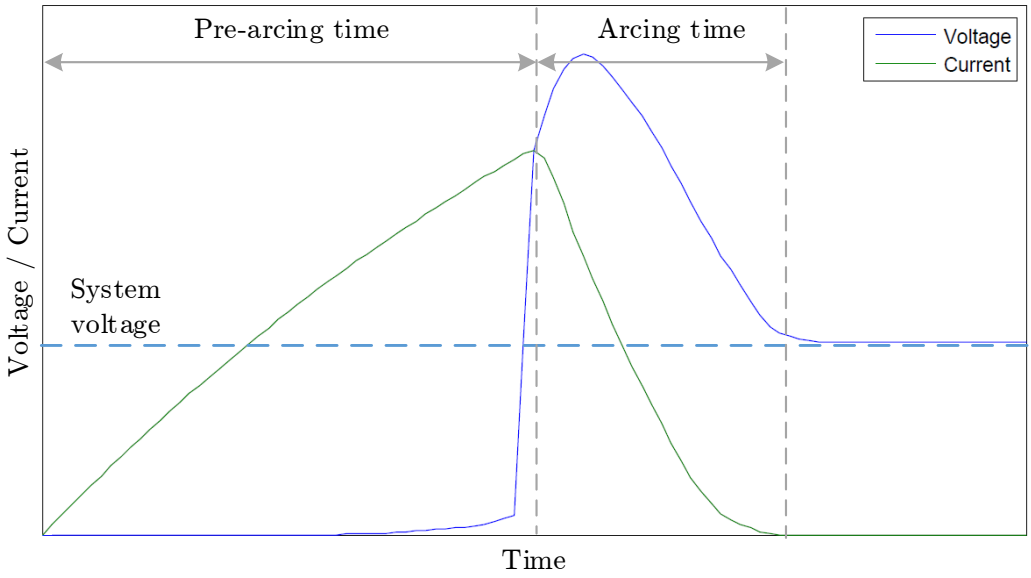

Figure 4.20.: Voltage and current graph of a fuse, adapted from [45]

Pre-arcing

The following Figure shows the fault circuit that is used for explaining the fuse behavior:

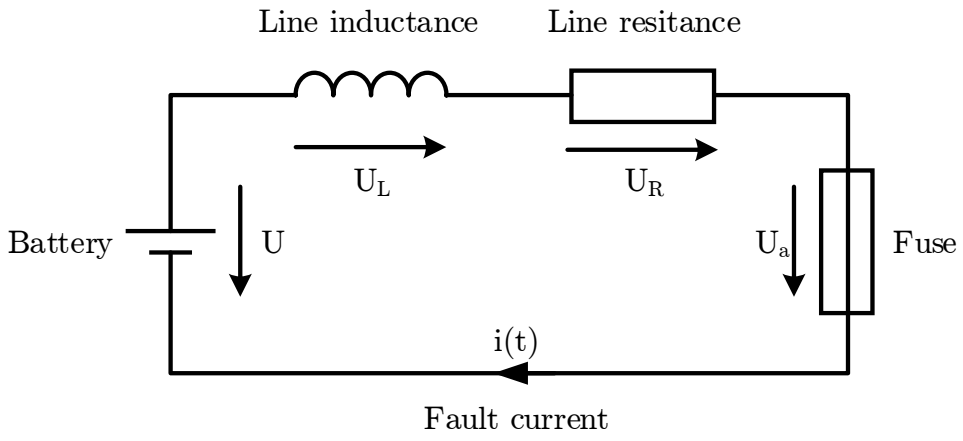

Figure 4.21.: Fault circuit

The time during the current increases until the element eventually melts is known as pre-arcing phase. As can be seen in figure 4.22, in the event of a fault the current rises exponentially towards the fault current I_F:

$$i(t) = I_F \cdot (1 - e^{-\frac{t}{\tau}}) = \frac{U}{R} \cdot (1 - e^{-\frac{t}{\tau}}), \tag{4.28}$$

with the time constant τ:

$$\tau = \frac{L}{R} \tag{4.29}$$

where R and L represents the line resistance and line inductance respectively [46]. As mentioned in [35] the time constant τ for battery systems can reach values up to 1 ms. For worst-case short-circuit scenarios, only the cell resistances for the different voltage levels (see table 4.2) are considered as line resistance. With the voltage levels given in 1.3 and the current rise calculated in 4.28 the maximum available fault currents can be seen in Figure 4.22.

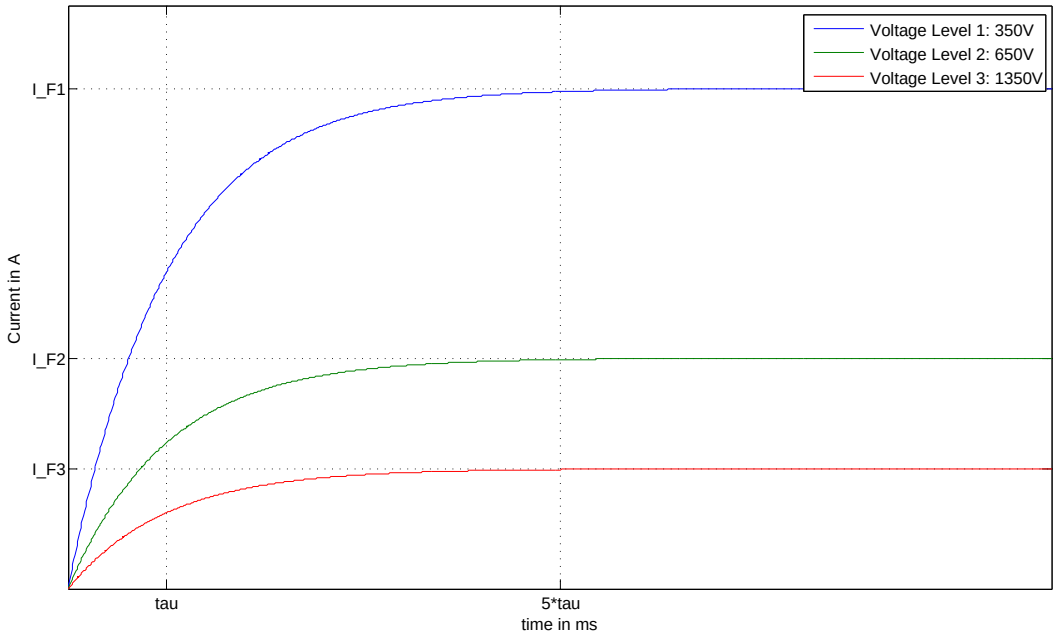

Figure 4.22.: Fault current rise at different voltage levels

It is interesting to note that the fault current decreases with higher system voltage. This is reasoned by an disproportional increase of resistance caused by decreasing parallel connection. As the temperature caused by I^2R losses rises slower for lower currents, the pre-arcing time increases for higher system voltages. The melting time and the corresponding It^2 value are usually given in the fuse data sheet [45].

Arcing

While the pre-arcing process is well understood and can be analytically predicted, the following arcing events are less well understood. After pre-arcing, the current will not fall to zero instantly. High voltages will be produced across the gap and an electric arc is initiated. The gap and consequently the arc will lengthen as more material will vaporize due to the high arc temperature. As described in equation 4.25 in chapter 4.5.3 the arc voltage consists of the anode-fall, arc column, and cathode-fall voltage. With an increasing

arc length, the voltage will further rise. The arc energy is absorbed by the filler material and causes the current to decrease. When the current reaches zero, the voltage across the gap drops to the system voltage [44, 45].

The peak arcing voltage across the fuse depends on the system voltage and the time constant τ. It increases with an increasing system voltage [46]. The maximum value of the peak arc voltage is determined by the fuse element length [47] and is usually given in the data sheet. As the arcing time depends on the system circuit specific application, it is usually not given in the data sheet [45].

4.6.4. Weight and size

In this study, 181 commercially available DC fuses with voltages up to 1250 V were analyzed in terms of weight, fuse body length and volume. The analyzed fuses are used for hybrid and electric vehicles, and DC drives [48, 49]. Table 4.9 gives an overview of the analyzed fuses. The rated current ranges from 10 A to 1100 A.

Table 4.9.: Overview of the analyzed fuses

Voltage in V	Amount of fuses analyzed	Average body length in mm	Average volume in cm^3
500	94	41.3	19
800	2	62.0	40
1000	43	73.1	247
1250	43	74.5	268

The fuses were grouped into current ranges of 10-50 A, 50-100 A, 100-200 A, 200-300 A, 300-400 A, and above 400 A. The body length and volume of the analyzed fuses are plotted against their maximum voltage rating as represented in Figure 4.23. The graphs show that with an increasing voltage

level, the fuse body length increases. For higher currents, the fuse body diameter increases and thus the overall fuse body volume increases.

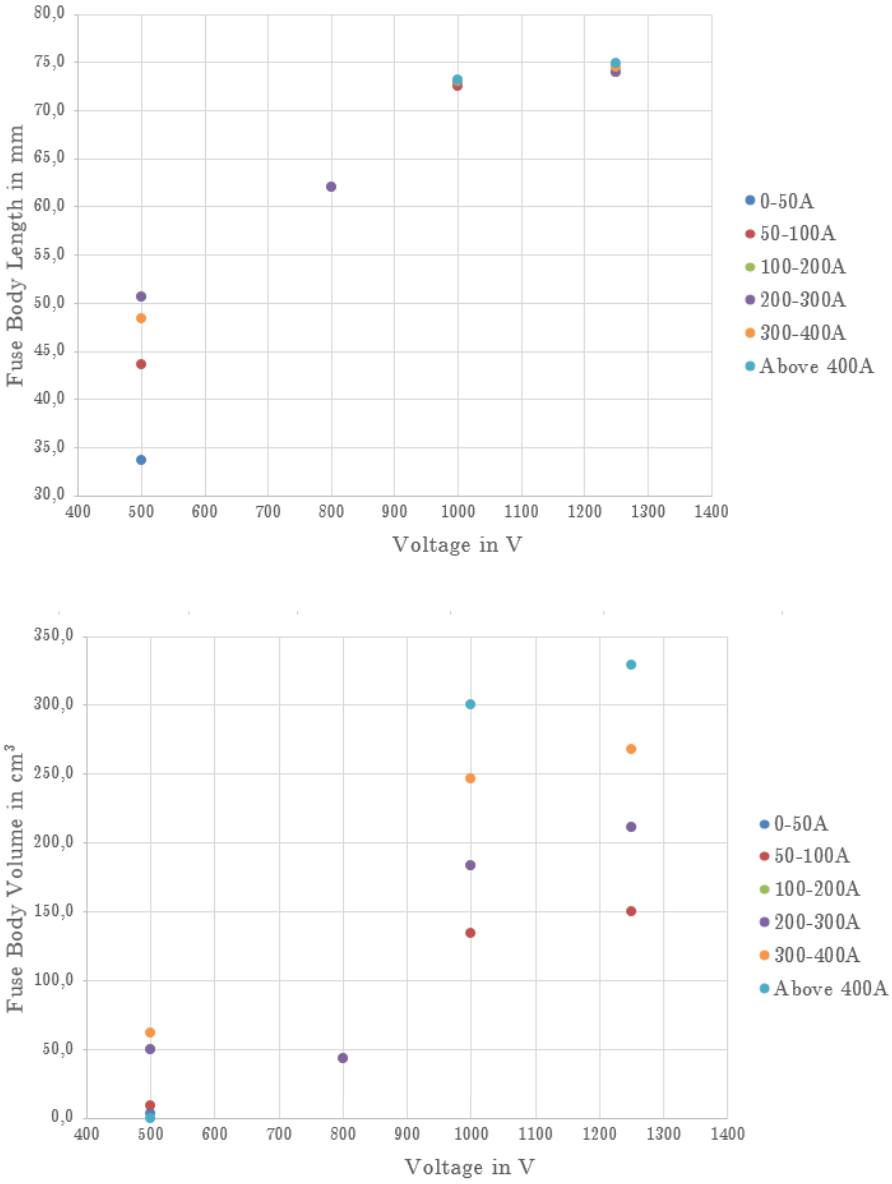

Figure 4.23.: Fuse body length and volume at different voltage levels

4.7. Pre-Charge Unit

The battery output is coupled to the DC/AC inverter and contactors are used to switch between the ”on” and ”off” state of the battery system. The power inverter typically employs a filter capacitor on its input side. The low impedance of the HV path from the battery to the DC link capacitor can result in very high inrush currents during battery switch-on. Without limiting those currents, damage could be caused to the HV contactors and other components. Before closing the main HV contactors, the DC link capacitor therefore needs to be charged to a predetermined voltage level by a pre-charging unit which consists of a resistor and a pre-charge contactor in series. The pre-charge switch couples the battery to the DC link and the inrush current is limited by the resistor. After the capacitor is charged to a defined level, the main HV contactors can be closed and the pre-charge contactor opens to disconnect the pre-charge unit [50].

4.7.1. Structure and switching sequence

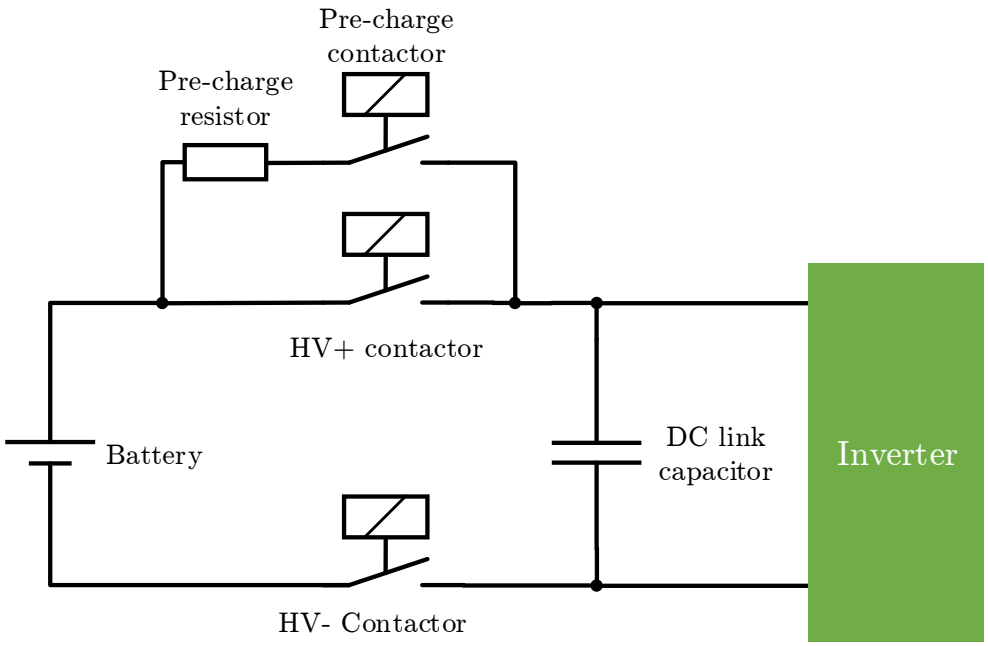

Figure 4.24.: HV schematic with pre-charge unit

Figure 4.24 shows the principle structure of a HV battery connected to a inverter with a DC link capacitor. The pre-charge circuit consists of a contactor and a resistor connected in series. The unit is typically connected in parallel to the positive HV contactor. Usually the following switch-on sequence is applied:

1. Switch-on negative contactor
2. Switch-on Pre-charge contactor
3. Charging the DC link capacitor
4. Switch-on positive contactor
5. Switch-off pre-charge contactor

The following picture shows the described pre-charge sequence and the typical resulting waveforms:

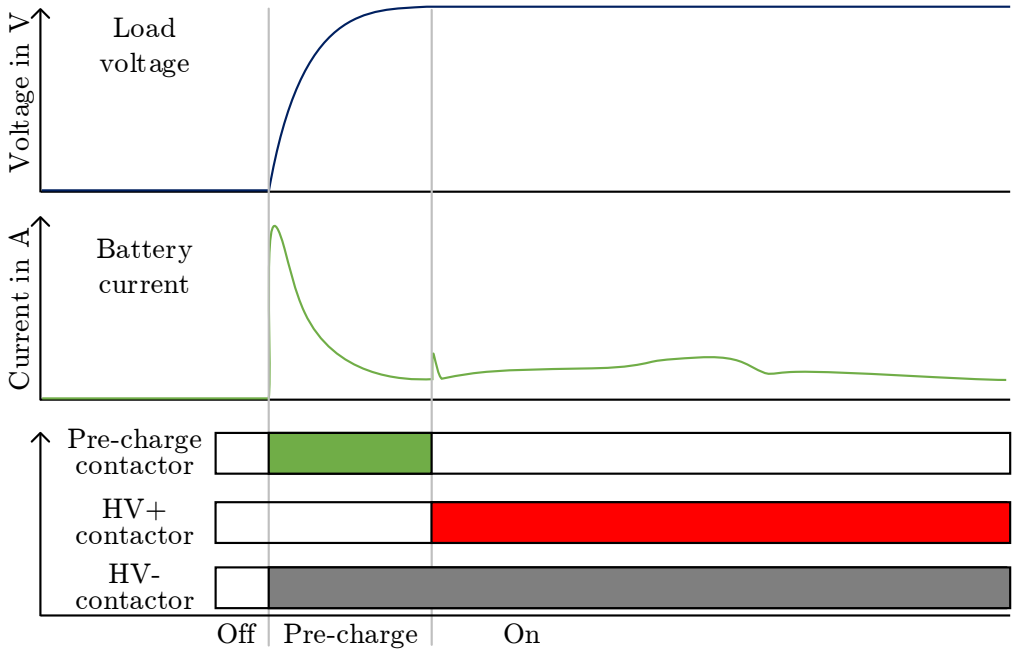

Figure 4.25.: Typical pre-charge behavior

The pre-charging time mainly depends on the resistance value and the required DC link voltage level after pre-charging. The capacitance is typically charged up to about 80 to 98% of the system voltage within a few 100 ms. This results in initial current peaks of about 10 to 30 A [7]. Automotive pre-charge resistors usually consist of wire windings that are embedded in a water proof cement core and enclosed in a metallic housing that provides mounting features and allows heat-sinking capabilities (e.g. cooling ribs). They are commercially available in wide ranges of resistance and power rating up to a few 100 W [51]. The pre-charge resistor has to be chosen in accordance with the DC link capacitor value to complete the pre-charge process in a short enough time so that the vehicle can be driven immediately after starting. The resistor has to be large enough to limit the surge current

but too large values result in undesirably long pre-charge times [50]. Pre-charge times under 500 ms are considered as acceptable [52]. Pre-charge contactors are regular automotive contactors as described in section 4.5. Since the current is limited by the resistor, the contactor can be chosen for small nominal current ratings in the range of a few 10 A but the contactor has to switch on to a short-time inrush current and has to withstand the whole system voltage.

4.7.2. Pre-charging at different voltage levels

In order to describe the behavior of the pre-charge unit at different voltage levels, a simple electrical RC network was analyzed and simulated in MATLAB. As already shown in Figure 4.24, during pre-charging the network consists of the battery voltage source U, the pre-charge resistor R and the DC link capacitor C. Under the assumption that the battery voltage stays constant over time, the DC link capacitor voltage u_c and the network current i can be calculated as

$$u_c(t) = U \cdot (1 - e^{-\frac{t}{\tau}}) \tag{4.30}$$

$$i(t) = \frac{U}{R} \cdot e^{-\frac{t}{\tau}} \tag{4.31}$$

with the capacitive time constant $\tau = RC$. At time τ, the surge current reaches $1/e$ of its initial value. The voltage drop u_R over the resistor can be calculated as:

$$u_R(t) = U - u_c(t) \tag{4.32}$$

DC link capacitors for automotive application have values of around 1000 μF [53]. Nominal system voltages were considered for simulation scenarios. After pre-charging, the HV+ contactor closes the main HV path with a resistance of a few 100 $m\Omega$ consisting of the cell resistance and the HV line resistance that includes busbars, cables, connection, contacts. In addition

to the voltage level specific cell resistance, a cable or busbar length of 7 m was considered for HV path resistance. This results in another current peak after pre-charging that has to be carried by the main contactors. Table 4.7.2 summarizes all input simulation parameters:

Table 4.10.: Input parameters for the pre-charge simulation

Item	Value	Unit
Capacitance	1000	μF
Nom. voltage level 1	350	V
HV path resistance voltage level 1	41	$m\Omega$
Nom. voltage level 2	650	V
HV path resistance voltage level 2	153	$m\Omega$
Nom. voltage level 3	1350	V
HV path resistance voltage level 3	590	$m\Omega$

The pre-charge process is considered to be finished after a pre-defined pre-charge time or after the DC link capacitor is charged up to a defined voltage level.

Defined pre-charge time

Different scenarios with typical pre-charge times between 200 ms and 500 ms were simulated. The pre-charge process is considered to be completed when the current reaches an acceptable value after approximately 5τ [52]. The required resistances to reach a given pre-charge time $t_{pre-charge}$ can therefore be calculated as:

$$R = \frac{t_{pre-charge}}{5 \cdot C} \tag{4.33}$$

The resulting resistance values are listed in the following table:

Table 4.11.: Resistance values for defined pre-charge times

Pre-Charge time in ms	τ in s	Resistance in Ω
200	0.04	40
250	0.05	50
300	0.06	60
350	0.07	70
400	0.08	80
450	0.09	90
500	0.10	100

Figure 4.26 shows the simulation results of the pre-charge behavior with a defined pre-charge time of 200 ms.

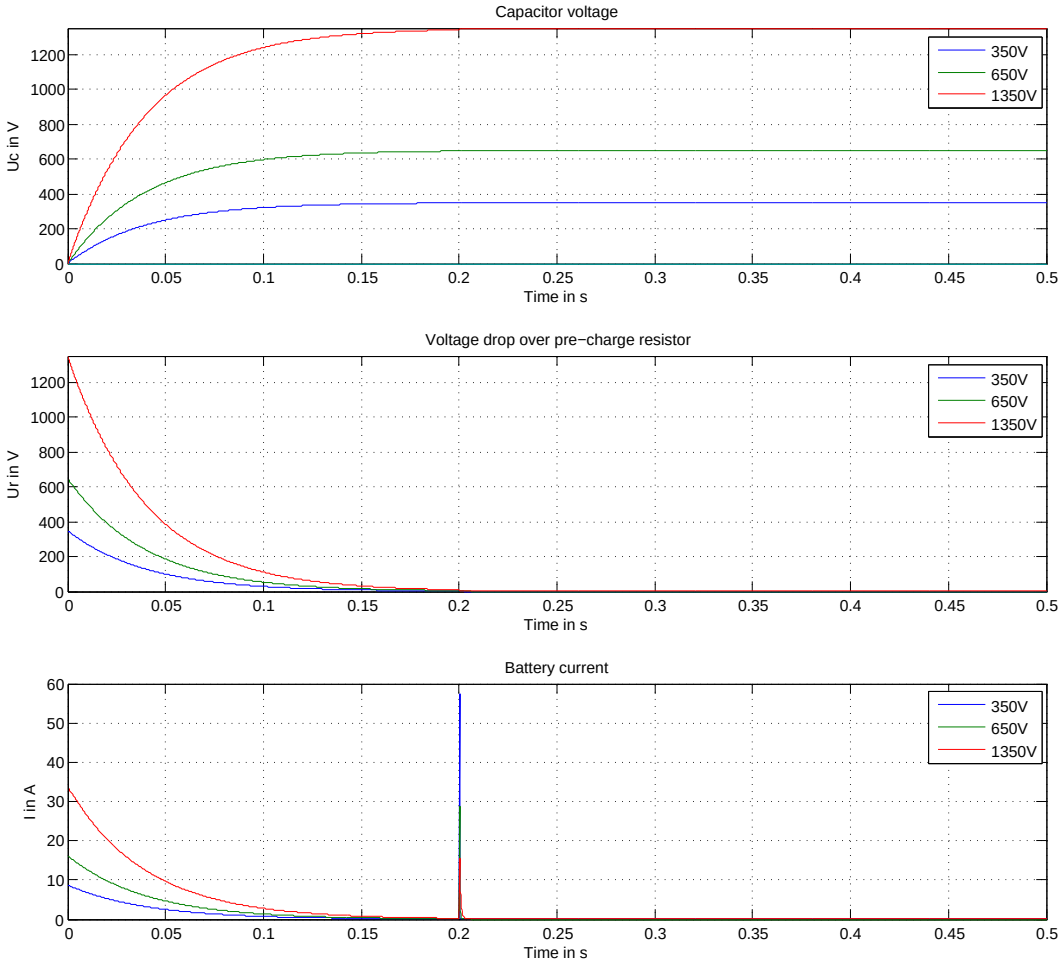

Figure 4.26.: Pre-charge behavior for a defined pre-charge time of 200 ms

Table 4.12 lists the simulation results. The full simulation results can be found in the appendix B.

Table 4.12.: Simulation results with a defined pre-charging time of 200 ms

Voltage level	Initial current peak in A	Current peak after pre-charging in A	Capacitor voltage after pre-charging in V	Voltage drop over resistor after pre-charging in V
1	8.8	49.1	347.0	2.4
2	16.3	25.5	645.6	4.4
3	33.8	14.2	1240.9	9.1

It is found that voltage level 1 has the lowest initial current peak as the same pre-charge resistance value is used for all voltage levels. The current peak after pre-charging is the lowest for voltage level 3, due to the disproportional cell resistance increase caused by decreasing cell connection in parallel for the higher system voltage level.

Defined capacitor level

For pre-charging the DC link capacitor to a defined capacity level, it is assumed that the initial surge current is limited to 25 A. This results in resistor values of 14 Ω, 26 Ω, and 54 Ω for voltage level 1, 2, and 3 respectively. Table 4.13 summarizes the input parameters used for the simulation.

Table 4.13.: Resistor values for defined capacity level

Voltage level	Resistor value in Ω	DC link capacitance charge	Voltage drop over resistor in V
1	14	90%	35
		92%	28
		94%	21
		96%	14
		98%	7
2	26	90%	65
		92%	52
		94%	39
		96%	26
		98%	13
3	54	90%	135
		92%	108
		94%	81
		96%	54
		98%	27

Figure 4.27 shows the simulation results for charging up to a capacitance level of 90% of the system voltage. Pre-charging times significantly lower than 200 ms can be achieved with this pre-charge strategy. However, the current peaks resulting after closing the HV+ contactors are around 10 times higher than the inital pre-charge peaks. Such high inrush currents may damage the HV contactors or other components over lifetime. Table 4.14 shows the simulation results. The full simulation results can be found in the appendix B.

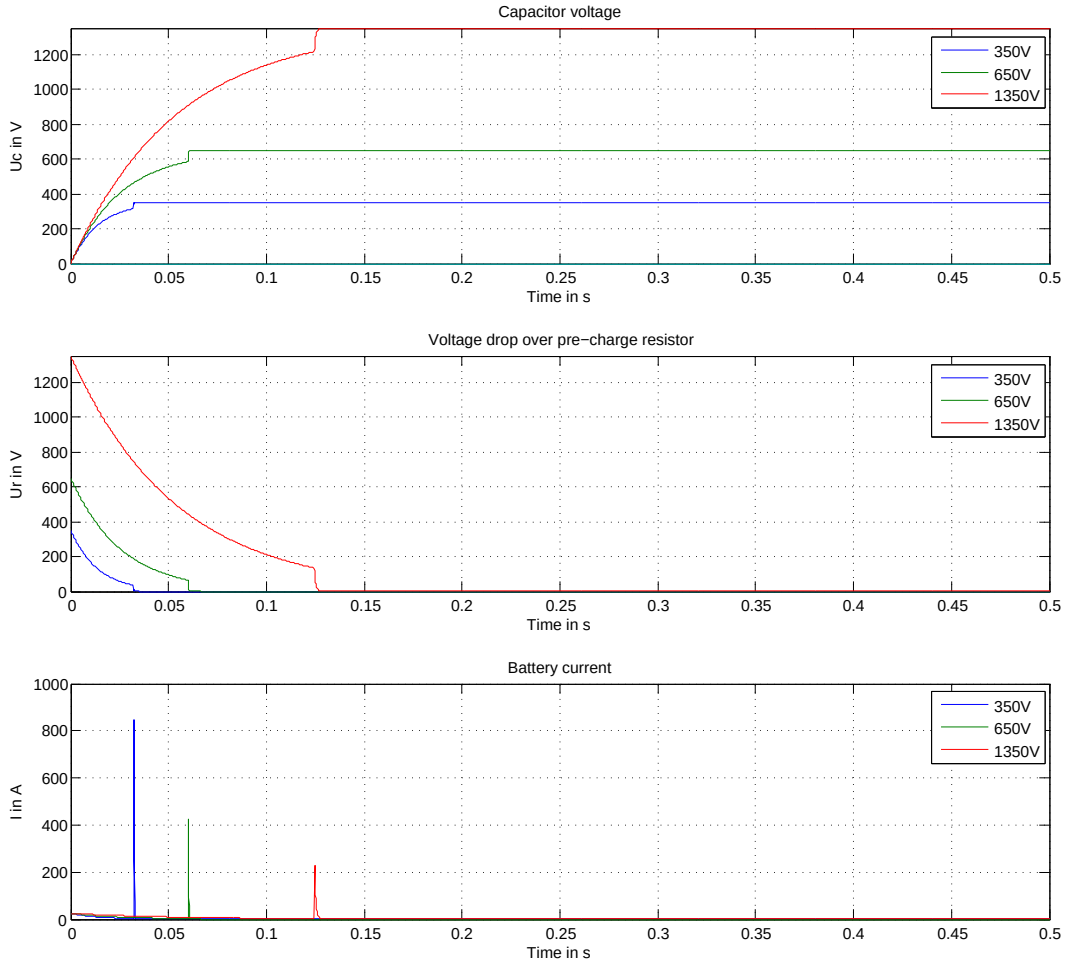

Figure 4.27.: Pre-charge behavior for charging to a defined capacitor level of 90% of the system voltage

Table 4.14.: Simulation results with for charging to a defined capcitor level of 90% of the system voltage

Voltage level	Pre-charge Time in s	Current peak after pre-charging in A	Capacitor voltage after pre-charging in V	Voltage drop over resistor after pre-charging in V
1	0.03	723.64	315.12	34.88
2	0.06	376.56	585.04	64.96
3	0.12	210.27	1215.11	134.89

The pre-charge unit also has to be designed so it can withstand several consecutive pre-charging sequences without overheating or damage. The required amount and timing of the sequences have to be aligned with the OEM.

If the pre-charge unit fails (e.g. damaged resistor or contactor) the inrush current will occur over the main HV contactors. This may result in damaging the contactors and other components and the fuse will most likely blow [52].

4.8. Sensor technology

In order to evaluate the battery condition (e.g. SOC, SOH, and SOF) and to operate the battery within its safety limits it is necessary to monitor parameters such as current, cell voltage, and cell temperature.

4.8.1. Voltage sensing

The voltage of each cell block in series is measured by the CSC for cell state determination and safety means. The measurement has to be done very

accurately in order to not exceed the cell voltage limits, during charging or discharging. Voltage sensing is realized through the same wires used for balancing described in section 4.3.4. The open voltage of the battery pack is also an indicator for the battery SOC. However, the batteries usually need rest time for the open-voltage to become stable, which can be in the range of hours [11]. For higher voltage levels, the wiring complexity increases, as each cell in series needs to be monitored. If the CSC is centrally located in the battery pack (see section 4.2), the wiring cables are routed through the battery pack and the cable insulation has to withstand the system voltage.

4.8.2. Current sensing

The current and therefore the charge entering and leaving the battery pack is measured for evaluation of SOC, SOF, and SOH. Galavanic isolated measurement is done with a hall sensor, which measures the magnetic flux caused by the current flow in a conductor. The measurement does not influence the inner resistance of the cells. Another option is a shunt sensor, which measures the voltage drop over a small resistor of usually 100 $\mu\Omega$ and a small temperature coefficient [7]. It is often necessary to measure current with both principles in order to achieve redundancy according to ISO 26262. The dielectric strength of shunt sensors must be high enough for a higher system voltage level.

4.8.3. Temperature sensing

It is important to measure the cell temperature for battery state determination and safety means. The upper temperature limit of lithium-ion cells is usually around 60°C [54]. Increasing the cell temperature above the safety limits may result in instability of the active material. The consequent reactions with the electrolyte lead to further temperature increase and to a possible cell fire. This chain-reaction is referred to as thermal runaway. For very low temperatures, only a fraction of the nominal power can be supplied or received by the cell. As the temperature sensors are usually in direct

contact with the cell surfaces, a high enough dielectric strength of sensor insulation material has to be achieved for higher voltage levels [7].

5. Electric drivetrain

The drivetrain of a battery electric vehicle comprises all components that are required to generate electric power and convert it into mechanical power for vehicle propulsion. The main components of an electric drivetrain include:

- Battery system
- HV conductors and connections
- Power electronics
- Electric machine
- Mechanical components such as transmissions, differential gear, drive shaft, and wheels.

The battery system is the vehicle's supply for electrical power. HV conductors and connections are used for electrical energy distribution between the HV components. The effects of higher voltages on conductors and connectors are similar than those within the battery that have already been described in section 4.4. In this section, the behavior of power electronics and electric machines on higher system voltages will be briefly described. The mechanical components are beyond the scope of this study and will not be further investigated.

5.1. Power electronics

Power electronics are used to control and convert the electric power flow between the HV battery and the electrical machine. In electric vehicles, the inverter transforms the battery DC voltage into a three-phase AC voltage output required to drive the electric motor. During braking, the power flow is reversed and the three-phase AC voltage is converted into DC voltage

used to charge the battery. The power electronics are mainly comprised of semiconductor switches and diodes. The electrical circuit of a three-phase inverter is shown in Figure 5.1.

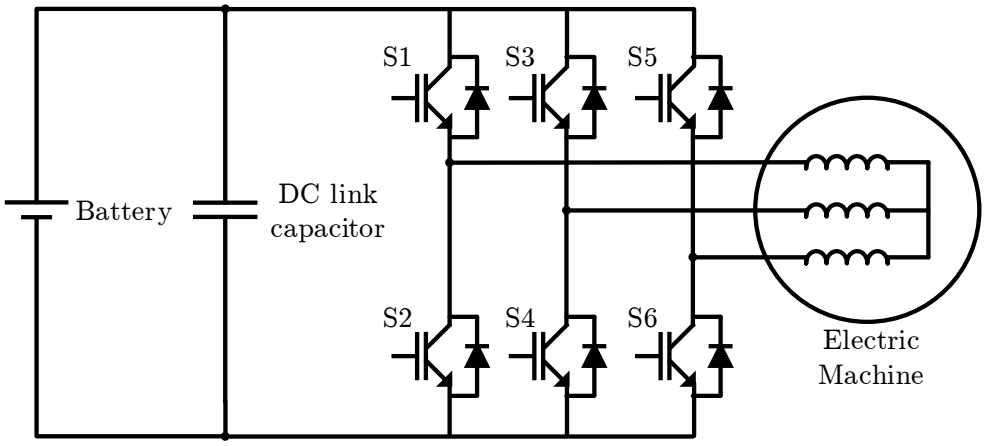

Figure 5.1.: Inverter circuit according to [11]

The three phases of the electric machine are usually Y-connection and then connected to the middle point of each inverter leg. The six transistors with antiparallel flyback diodes are working as bidirectional switches $S1$ to $S6$ [11]. The diodes are used to provide a path for the current driven by the motor inductance magnetic energy during transistor switch-off. A DC link capacitor is used to decouple the HV battery from the power electronics during semiconductor switching and to provide a low-impedance path for effects such as current ripples caused by semiconductor switching. DC link capacitors have values of around 1000 μF [53]. The inverter semiconductor properties are highly voltage depended and need to be investigated for different system voltages.

5.1.1. Semiconductor behavior at higher system voltage

Blocking voltage

In electric vehicles, insulated gate bipolar transistors (IGBT) are commonly used mainly due to low switching and conduction losses in high-power and high-voltage applications and reverse blocking capabilities [11]. Figure 5.2 shows the structur of a non-punch-through (NPT) IGBT. The electric field gradually decreases within the n^- doped drift-region (epitaxial layer).

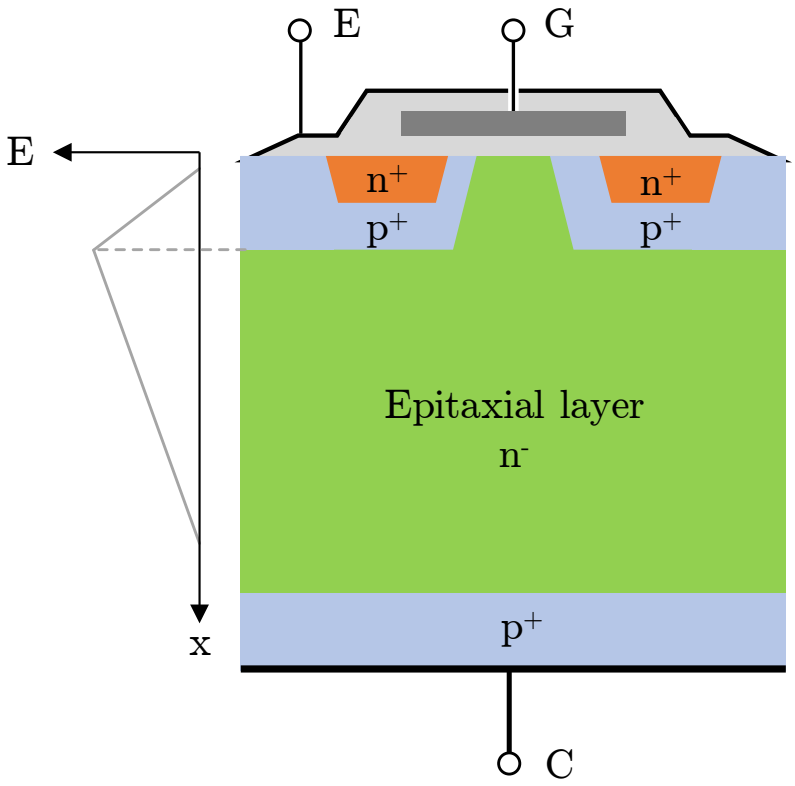

Figure 5.2.: IGBT structure according to [6]

The maximum blocking voltage mainly depends on the low doped n^- center region. For a NPT IGBT the width w_B of this region is approximated to be proportionally to the breakdown voltage V_{BD} according to [6]:

$$w_B \sim {V_{BD}}^{7/6} \tag{5.1}$$

The center region also defines the semiconductor on-state resistance R_{CE} and conduction losses.

The turn-off losses can be reduced by reduction of the collector-side p-doping, which results in a current gradient $\frac{dI}{dt}$ increase [55]. This however, results in a higher voltage overshoot $V_{CE,max}$ caused by the IGBT internal and external stray inductances L_s in the system:

$$V_{CE,max} = L_s \frac{dI}{dt} \tag{5.2}$$

It can be stated, that the base material doping has a huge impact on breakdown voltage, overshoot voltage, and switching losses. The overshoot voltage can be in the range of a few 100 V, depending on the switching frequency, stray inductance, and current gradient. The IGBT blocking voltage must be rated higher than the system voltage. Commercially available IGBTs are for automotive usage have blocking voltages up to 1200 V and are suitable for maximum system voltages of up to about 800 V [3]. This results in a system-to-blocking-voltage ratio of 66%, which would yield a necessary IGBT blocking voltage of about 2300 V for system voltages up to 1500 V.

Reduction of overshoot voltage

In order to minimize voltage overshoot, the stray inductance must be reduced while having a low resistive path for the continuous current. The stray inductance fall into inverter internal and external sources. Internal sources for inductive loops include semiconductor wire bonding, power tracks on the copper substrate, and bus bar connection elements inside the inverter modules. The external sources are mainly caused by the resulting HV path busbar and cable routing loop area and stray inductances from other HV components such as the DC link capacitor. Countermeasures include compensating capacitors directly mounted in parallel to each IGBT and low-inductive HV routing by avoiding loops. Another option

to minimize overshoot voltage is the reduction of switching speed, which consequently decreases the current gradient [56].

5.2. Electric Machine

The electric machine converts electrical energy into mechanical energy used for vehicle traction. Electric vehicles are usually operated with three-phase AC synchronous or asynchronous machines. Due to their compact design and avoidance of brushes, synchronous machines are commonly equipped with permanent magnets rather than independently excited electromagnets in the rotor. It can be stated that for all electric machines, the torque is depended on the current rate, and the nominal speed on the machine nominal voltage [3].

5.2.1. Behavior at higher system voltages

Rated voltage

The rated voltage of the electrical machine is defined to meet the system voltage requirements and depends on parameters such as geometry, pole pairs, rated speed, and rated flux. In the following considerations, said parameters are assumed to be constant for a fair comparison of different system voltages. When neglecting the stator resistive losses, the rated voltage for AC machines can be approximated by

$$V_r \approx 2\pi k_1 N \phi f, \tag{5.3}$$

where k_1 represents the machine constant, ϕ the magnetic flux, f the frequency and N the number of stator winding turns. The limits of magnetic flux and frequency are defined by geometric and mechanical parameters. The rated voltage can be adjusted by changing the number of turns: when increasing the number of turns, the rated voltage increases and the wire cross-section can be reduced, provided that the wires do not become too

thin. The number of turns need to be adapted so that the minimal battery voltage can meet the nominal machine voltage and nominal speed. When reaching the maximum voltage and nominal speed, electric machines can be operated in the field weakening range. By drawing reactive power, the machine speed can be increased while reducing torque and maintaining constant electrical power. Figure 5.3 shows a principle torque over speed graph and the said constant torque and constant power region. To ensure full torque at nominal speed n_r, the nominal machine voltage has to be higher or equal the minimum battery voltage [6, 3].

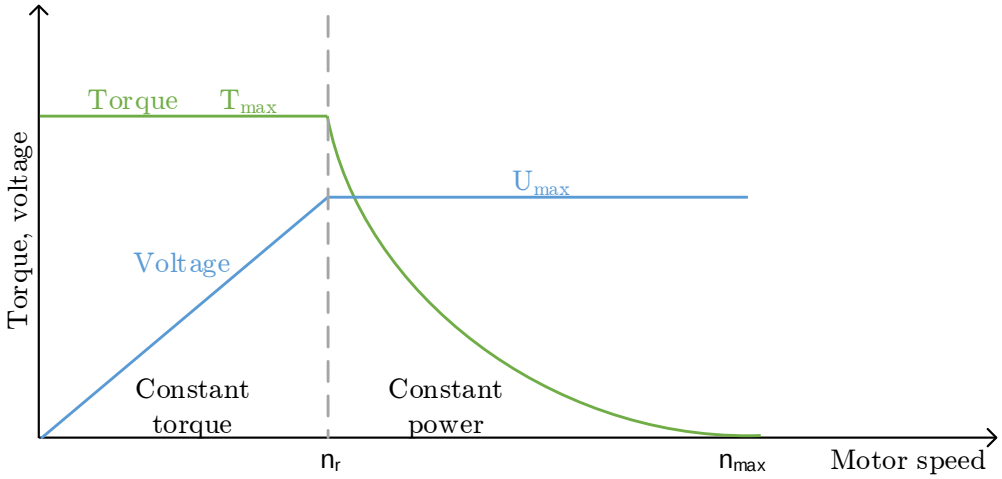

Figure 5.3.: Torque over speed in constant torque and constant power region according to [11]

Insulation

The stator insulation is comprised by slot, conductor and phase insulation as depicted in Figure 5.4.

If the number of turns is changed to adjust the rated voltage, the wire insulation must be adjusted accordingly. The filling factor describes the ratio between total conductor cross-section to slot area and has a value of up to 0.4. As the slot mainly consists of air and filling materials between

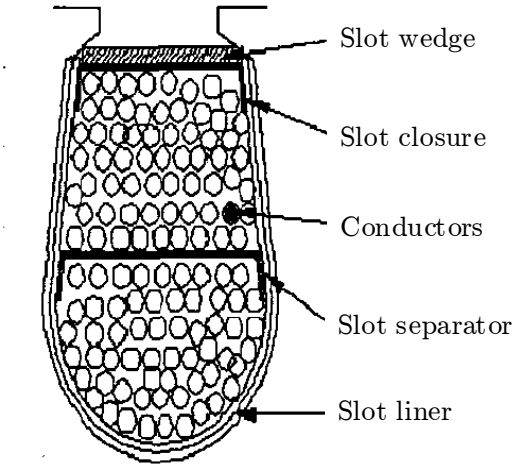

Figure 5.4.: Electrical machine insulation adapted from [57]

the conductors, the filling factor is barely influenced by the insulation [6]. To sum up, the effects on insulation thickness can be neglected in machine design for higher voltages.

It has been described in section 5.1.1 that the inverter IGBT high-frequency switching causes transient voltage overshoot. This can lead to partial discharge in machine insulation and eventual aging or breakdown as described in [57]. These voltage stresses are increased with higher system voltage and need to be considered in electrical machine insulation design.

Losses

When increasing the number of turns for higher rated machine voltage, the stator current I_s required for the same electric power will decrease. A higher number of turns N results in an increased copper wire length l. While the resistance R will increase proportionally with N, the copper cross-section A can be decreased by N. The conductor losses P_v remain unchanged, as can be seen in the following equation:

$$P_v = {I_s}^2 R = {I_s}^2 \rho \frac{l}{A} = \left(\frac{I_s}{N}\right)^2 \rho \frac{l \cdot N}{A/N} \tag{5.4}$$

As no effects on flux magnitude and frequency are assumed, the stator iron and rotor losses show no effect by changing the stator winding turns [6].

6. Conclusion

This study explored the effects of higher system voltage levels on the electric components in vehicle battery systems on a system engineering level. Chapter 1 gave an overview of the classification of voltage levels according to national and international standards. In the automotive industry, voltages above 30 Vac and 60 Vdc are classified as high voltage. For this study, three system voltage levels with nominal voltages of 350 Vdc, 650 Vdc, and 1350 Vdc were defined.

In chapter 2 the WLTP and CACD drive profiles were analyzed. A simple vehicle model was described for a speed cycles to power cycle conversion. It could be observed that the CACD cycle has higher power requirements and had therefore been used in further considerations. The currents for the defined voltage levels were calculated. It can be concluded that under constant power demand the current requirements decrease for an increasing voltage level.

Chapter 3 investigates the safety measures for higher system voltages. From the reviewed standards it can be concluded that the higher insulation requirements for solid insulation, clearance distance, and creepage distance are necessary with increasing system voltages. As packaging space is in general limited in battery systems, higher insulation requirements such as larger safety distances may lead to design hurdles.

Chapter 4 presents the effects of higher voltages on cell connection, power losses, and electrical components for energy distribution and safety means. To increase the system voltage, more cells have to be connected in series. This yields a more complex wiring and connection design. The weakest cell determines the overall performance of the battery system. Although the cell resistance increases for higher voltages, the power losses remain the same and the short-circuit current decreases. A simple thermo-electrical

model was created in MATLAB to analyze the thermal behavior of HV conductors. Compared to a nominal voltage of 350 V, significant weight, cross-section, and power losses reductions can be achieved for 650 V. These beneficial effects however, flatten out with voltages reaching 1350 V. Higher voltages also lead to different arcing behavior in contactors and fuses. A comparison of a variety of commercially available contactors and fuses was done. It was found that the contactor weight and size mainly depends on its rated current. Fuses for higher voltages show a larger body length and are therefore larger in size. The pre-charge behavior at different system voltages was analyzed based on MATLAB simulations. The system voltage only has a minor impact if pre-charge contactor and resistor values are adjusted accordingly. In general it can be stated that market availability of electric components above 800 V is scarce as of 2016.

Chapter 5 gave an overview of the effects of higher voltages on the power electronics and the electric machine. Currently IGBT semiconductors are available for voltages up to 1200 V. The limiting factor for higher voltages is the IGBT blocking voltage. It is expected that further semiconductor development will lead to reduced switching losses and higher blocking voltages. The rated voltage for electric machines mainly depends on the number of winding turns when geometrical properties are considered to be constant.

Future work

Future work on higher system voltage levels may involve:

- Complete drivetrain model in MATLAB and analytic analysis of higher system voltages
- Detailed market research on electric components for higher voltages
- Detailed investigations on power electronics and electric machine
- Considerations on charging infrastructure and behavior on existing charging stations.

Appendices

A. Touch protection

The International Protection Marking (IP code), describes the degree of protection for electric enclosures against dust, intrusion, and water. The rating is defined in standard IEC 50529 [58]. Figure A.1 shows the IP code formation and Tables A.1 and A.2 list the meaning of the IP code numbers and letters.

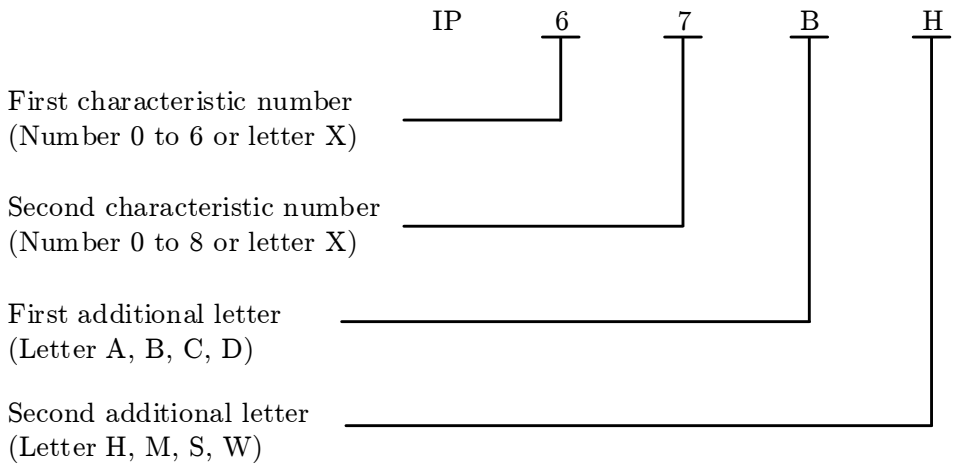

Figure A.1.: IP code formation according to [58]

Table A.1.: IP ratings according to [58]

Number	Protection against
First characteristic number	
0	No protection
1	Large objects (e.g. back of a hand) up to 50mm^3
2	Fingers or similar objects up to 12 mm
3	Tools and wires up to 2.5 mm
4	Tools and wires over 1 mm
5	Dust with limited ingress
6	Dust tight
Second characteristic number	
0	No protection
1	Vertically falling drops of water
2	Direct sprays of vertically falling water up to 15 degrees
3	Direct sprays of vertically falling water up to 60 degrees
4	Water sprayed from all directions
5	Low-pressure jets of water from all directions
6	Strong jets of water from all directions
7	Temporary immersion between 15 cm and 1 m
8	Long periods of immersion under pressure
9	High pressure, high temperature jets of water from multiple directions

Table A.2.: Additional letters according to [58]

Number	Protection against
First letter	
A	Back of a hand
B	Finger
C	Tool
D	Wire
Second letter	
f	Oil
H	High voltage device
M	Moving object during water test
S	Still object during water test
W	Weather conditions

B. Pre-charging simulation results

Table B.1 and B.1 show the simulation results for different pre-charge times and capacitor charge levels.

Table B.1.: Simulation results with a defined pre-charging time

Pre-Charge time in ms	Voltage level	Initial current peak in A	Current peak after pre-charging in A	Capacitor voltage after pre-charging in V	Voltage drop over resistor after pre-charging in V
	1	8.8	57.5	347.6	2.4
200	2	16.3	28.8	645.6	4.4
	3	33.8	15.5	1340.9	9.1
	1	7.0	57.4	347.6	2.4
250	2	13.0	28.7	645.6	4.4
	3	27.0	15.5	1340.9	9.1
	1	5.8	57.4	347.6	2.4
300	2	10.8	28.7	645.6	4.4
	3	22.5	15.4	1340.9	9.1
	1	5.0	57.4	347.6	2.4
350	2	9.3	28.7	645.6	4.4
	3	19.3	15.4	1340.9	9.1
	1	4.4	57.3	347.6	2.4
400	2	8.1	28.7	645.6	4.4
	3	16.9	15.4	1340.9	9.1
	1	3.9	57.3	347.6	2.4
450	2	7.2	28.7	645.6	4.4
	3	15.0	15.4	1340.9	9.1
	1	3.5	57.3	347.6	2.4
500	2	6.5	28.7	645.6	4.4
	3	13.5	15.4	1340.9	9.1

Table B.2.: Simulation results with for charging to a defined capcitor level

Capacitor level	Voltage level	Pre-charge Time in s	Current peak after pre-charging in A	Capacitor voltage after pre-charging in V	Voltage drop over resistor after pre-charging in V
	1	0.032	846.6	315.1	34.9
90%	2	0.060	424.8	585.0	65.0
	3	0.125	228.5	1215.1	134.9
	1	0.036	679.0	322.0	28.0
92%	2	0.066	340.0	598.0	52.0
	3	0.137	182.6	1242.2	107.8
	1	0.040	507.1	329.1	20.9
94%	2	0.073	255.0	611.0	39.0
	3	0.152	137.1	1269.1	80.9
	1	0.045	338.0	336.1	13.9
96%	2	0.084	169.7	624.0	26.0
	3	0.174	91.4	1296.0	54.0
	1	0.055	169.5	343.0	7.0
98%	2	0.102	84.7	637.0	13.0
	3	0.211	45.7	1323.0	27.0

C. Matlab codes

Drive cycle analysis

```
% -- DRIVE CYCLE CONVERSION - Fabian Luttenberger
    2016 ------------%

%init
clc
close all
clear all

%Program Parameters
store_excel = 0;
plot_speed_profiles = 1;
plot_power_profiles = 1;
plot_rms = 0;
plot_currents = 0;
current_profile_analysis = 0;
save_as_pdf = 0;
savename = 'power_peaks';
t_a = 0.01; %Sample rate for profiles
j0 = 1; %Begin
N = 2; %End
smth = 1/1000; %0 = off; 5 = std; <5 even smoother;
show_jerk = 0;
peaks = [0.1 1 5 10 30 60];
legend_pos = 'northwest';

%Voltages
%Level 1:
u(1,1) = 250;
u(1,2) = 350;
u(1,3) = 400;
%Level 2:
u(2,1) = 450;
u(2,2) = 650;
u(2,3) = 750;
%Level 3:
u(3,1) = 950;
u(3,2) = 1350;
u(3,3) = 1500;
```

```
38 u_title = {'Voltage Level 1','Voltage Level 2','
      Voltage Level 3'};
39
40 %Vehicle Model
41 v_m = 1600; %Vehicle mass in kg
42 v_a = 2; %Vehicle front area in m2
43 v_ad = 0.28; %Vehicle air drag coefficient
44 v_fc = 0.01; %Friction coefficient
45 v_eff = 0.73; %Vehicle efficiency
46 v_recup_eff = 0.3; % Recuperation efficiency
47
48 %Load Profiles from Excel
49 [speed_profiles , mylegend] = loadExcelProfiles(
      store_excel );
50
51 %Memory pre-allocation
52 T_peaks = zeros(numel(peaks)+1,N);
53 I_peaks = T_peaks;
54 n_peaks = numel(peaks)+1;
55 uu = u';
56 uu = 1./uu(:);
57 I_summary = uu*ones(1,n_peaks*N);
58
59 %Initiate Figures
60 cc=hsv(N); %Different colours
61 scrsz = get(groot,'ScreenSize');
62 if ( plot_speed_profiles || plot_power_profiles ||
      plot_currents )
63 f_sp = figure('Position',[10 100 scrsz(3)/2 scrsz(4)
      /1.5]);
64 end
65 if current_profile_analysis
66 f_c = figure('Position',[10 100 scrsz(3)/1.2 scrsz(4)
      /1.1]);
67 u_legend = {};
68 end
69 power = {};
70 mylinestyle = {'-s','-o','-*','-d','-x'};
71 mylinecolor = {'b','g','r','y'};
72
73 %% Loop through speed profiles
74 for j=j0:N
75 % --- Load and interpolate speed profile ---
76
77 v_time_ = speed_profiles{j}(:,1);
78 v_speed_ = speed_profiles{j}(:,2);
79 v_time = [0:t_a:max(v_time_)]; %interpolated time
80 v_speed = interp1( v_time_ , v_speed_ , v_time ,'
      spline'); %interpolated speed
81 v_time = v_time(:);
```

```
82 v_speed = v_speed(:);
83
84 %% --- Calculations ---
85 [v_power, jerk, a] = transformToPower( v_time,
       v_speed, v_m, v_a, v_ad, v_fc, v_eff, v_recup_eff,
       t_a, smth );
86 v_power_rms = rms(v_power);
87 power{j} = [v_time(:), v_power(:)];
88
89  if (current_profile_analysis)
90      [T, v_power_rms_max ] = analyseCurrentProfile(
           v_time , v_power, peaks );
91      T_peaks(:,j) = T(:);
92      I_peaks(:,j) = v_power_rms_max(:);
93      disp(v_power_rms_max(end))
94  end
95
96 %% ---- Plotting ----
97 if ( plot_speed_profiles || plot_power_profiles ||
       plot_currents )
98     figure(f_sp);
99     v_time_max = ceil(max(v_time/100))*100;
100    subplot(N,1,j);
101    DisplayCurrents
102
103  %Power & Speed Plot
104 if ( plot_speed_profiles && plot_power_profiles && ~
       plot_currents )
105    [ax,h1,h2] = plotyy(v_time,v_speed,v_time,v_power
          );
106    ylabel(ax(2),'Vehicle power in kW');
107    ylabel(ax(1),'Vehicle speed in km/h');
108    set(ax(1),'ylim',[0 160]);
109    set(ax(2),'ylim',[-80 80],'YTick',[-80:20:80]);
110    set(h1,'LineStyle','--');
111    set(ax(1),'xlim',[0 v_time_max]);
112    set(ax(2),'xlim',[0 v_time_max]);
113    set(ax(2),'XTick',[]);
114    set(ax,'YColor',[0 0 0]);
115    %set(h(2),'ylim',[0 100]);
116    legend('Speed profile','Power profile','Location'
          ,legend_pos);
117    plotverticals(mylegend(j));
118    set(ax(2),'YGrid','on');
119    DisplayCurrents
120
121 % Only Speed Plot
122 elseif (plot_speed_profiles && ~plot_power_profiles )
123    plot(v_time,v_speed);
```

```
124       ylabel('Vehicle speed in km/h');
125       set(gca,'ylim',[0 140]);
126       plotverticals(mylegend(j));
127       set(gca,'YGrid','on');
128
129   %Only Power Plot
130   elseif ( ~plot_speed_profiles && plot_power_profiles
          )
131       plot(v_time,v_power);
132       ylabel('Vehicle power [kWh]');
133       if plot_rms
134           hold on;
135           plot([0 v_time(end)],[v_power_rms v_power_rms
                ]);
136           legend('Power profile','Power RMS','Location'
                ,legend_pos);
137       end
138
139    %Only Current Plot
140   elseif ( plot_currents )
141       plot(v_time,[v_power/u(1,2) v_power/u(2,2)
             v_power/u(3,2)]*1000);
142       ylabel('Vehicle currents in A');
143
144       %Current and speed plot
145   elseif (plot_speed_profiles && plot_currents )
146       [ax,h1,h2] = plotyy(v_time,v_speed,v_time,[
             v_power/u(1,2) v_power/u(2,2) v_power/u(3,2)
             ]*1000);
147       ylabel(ax(2),'Vehicle current in A');
148       ylabel(ax(1),'Vehicle speed in km/h');
149       set(ax(1),'ylim',[0 160]);
150       set(ax(2),'ylim',[-200 200],'YTick'
             ,[-200:50:200]);
151       set(h1,'LineStyle','--');
152       set(ax(1),'xlim',[0 v_time_max]);
153       set(ax(2),'xlim',[0 v_time_max]);
154       set(ax(2),'XTick',[]);
155       set(ax,'YColor',[0 0 0]);
156       legend('Speed profile','Current profile','
             Location',legend_pos);
157       plotverticals(mylegend(j));
158       set(ax(2),'YGrid','on');
159
160   end
161   title(mylegend(j))
162   hold off;
163
164   set(gca,'XTick',[0:200:v_time_max]);
```

```
165 set(gca,'YTick',[0:20:140]);
166 xlim([0 v_time_max]);
167 xlabel('Time in s');
168 end
169
170 %--- Plot Current Profiles ---
171 if current_profile_analysis
172     figure(f_c);
173
174         aleg = char(strcat(cellstr(mylegend(j)), ' U
              min'));
175         bleg = char(strcat(cellstr(mylegend(j)), ' U
              nom'));
176         u_legend{end+1} = aleg;
177         u_legend{end+1} = bleg;
178
179         p = ones(9,1)*v_power_rms_max'*1000;
180         ib = n_peaks*(j-1)+1;
181         ie = n_peaks*j;
182         I_summary(:,ib:ie) = p.*I_summary(:,ib:ie);
183
184     for i=1:3;
185         subplot(3,1,i)
186         hold on;
187         plot(T,[v_power_rms_max*1000./u(i,1)
              v_power_rms_max*1000./u(i,2)],mylinestyle{i
              },'Color',mylinecolor{j}); %'color',cc(j,:)
              ,
188         title(u_title(i));
189         legend(u_legend);
190         set(gca,'XScale','log');
191         grid on;
192         xlabel('Pulse duration in s');
193         ylabel('Current in A');
194     end
195 end
196 end
197
198 I_summary = [T_peaks(:)'; I_summary];
199 tightfig(f_sp);
200 if save_as_pdf
201     saveas(f, savename, 'pdf');
202 end
203 if show_jerk
204     NN =10;
205     jerk = zeros(NN,1);
206 figure();
207 for i=0:NN-1
208     [v_power, jerk(i+1)] = transformToPower( v_time,
          v_speed, v_m, v_a, v_ad, v_fc, v_eff,
          v_recup_eff, t_a, i );
```

```
end;
plot(0:NN-1,jerk)
end
```

```
function [v_power ,jerk, v_acc] = transformToPower(
    v_time, v_speed, v_m, v_a, v_ad, v_fc, v_eff,
    v_recup_eff, t_a, smth )
%Calculate acceleration
v_acc = diff(v_speed./3.6)./diff(v_time);
v_acc(end+1) = 0;
%Calculate jerk
jerk = max(diff(v_acc)./diff(v_time));
%Smooth profile
if smth > 0
    v_acc = smooth(v_acc,smth);
    % alpha = 0.2;
    % v_acc = filter(alpha, [1 alpha-1], v_acc);
end
%Include recuperation in acceleration
v_acc = v_acc.*(v_acc<0)*v_recup_eff + v_acc.*(v_acc
    >0); %
%Calculate air drag and rolling forces
air_drag_res = 1.2/2 .* v_ad .* v_a .* (v_speed/3.6)
    .^2;
roll_res = v_m * 9.81 * v_fc;
%Calculate power
v_power = -1/v_eff .* (v_m .* v_acc + air_drag_res +
    roll_res) .* (v_speed./3.6) ./1000;
end
```

Thermal analysis

```
% -- THERMAL CABLE SIMULATION - Fabian Luttenberger
    2016 --%

clear all;
clc;
close all;

%Init:
material = 1; % Material selection: 1... Copper; 2...
    Alu
insulation = 1; %  Material selection: 1... PVC; 2...
    EPR
geometry = 1; % Geometry selection: 1... Cable; 2...
    Busbar (1mm height)
xsection = [18 8 3]; % Cross-section of conductor in
    [mm2]
wall_thickness = [0.8 0.64 0.56]; % wall thickness
    cable [mm]
```

```
I_all = [57.9 31.2 15]; % Currents [A]
U = [350 650 1350]; %Voltage levels [U]
hc = 8; % Heat convection [W/m2K]
T_amb = 25; % Ambient Temperature [C]
T_start = 25; % Start Temperature Cable [C]
e = 0; % Emissivity of the insulation
bc = 5.670367E-8; %Stefan-Boltzmann constant [W/m2K4]
N = 2000; % Time [s]
dt = 0.1; % Time step [s]

% Plot mode:
% 1... On one plot
% 2... Different plots
plot_mode = 2;
show_res_plot = 0;
show_power_plot = 0;
show_summary_plot = 1;

% C to K
T_start = T_start + 273;
T_amb = T_amb + 273;

% Plot for each current:
N_c = numel(I_all);
color = hsv(N_c); % Define diferent plot colors for
    each current
mylegend = {};
mylegend_res = {};

% Set Screen Size
scrsz = get(groot,'ScreenSize');
fig = figure('Position',[10 100 scrsz(3)/1.8 scrsz(4)
    /1.3]);
if show_res_plot
fig_res = figure('Position',[10 100 scrsz(3)/1.8
    scrsz(4)/1.6]);
end
if show_power_plot
fig_power = figure('Position',[10 100 scrsz(3)/1.8
    scrsz(4)/1.6]);
end
if show_summary_plot
fig_prop = figure('Position',[10 100 scrsz(3)/1.8
    scrsz(4)/1.6]);
end

% Set output vectors
P_ = 0; %Power
R_ = 0; %Resistance
W_ = 0; %Weight
CD = 0; %Current density
output = zeros(12,3);
```

```
60
61 % Calculate transient thermal behavior
62 for j=1:N_c
63
64 %Considere different cross-sections
65 j_xsection = 1;
66 if numel(xsection) > 1
67     j_xsection = j;
68 end;
69
70 %Considere different wall thickness
71 j_wt = 1;
72 if numel(wall_thickness) > 1
73     j_wt = j;
74 end;
75
76 I = I_all(j); %Considere different currents
77
78 T = ones(2,1)*T_start; %Define calculating
       temperature vector
79 T_all = ones(4,1)*T_start; %Temperature vector of all
       4 temperatures
80
81 % Geometry properties
82 xsection(j_xsection);
83 xsect = xsection(j_xsection)*1E-6; %Cross section of
       copper [m2]
84 r_c = sqrt( xsect / pi ); %radius of copper [m]
85 r_iso = r_c + wall_thickness(j_wt)*1E-3; %radius of
       cable with insulation [m]
86 r_iso_half = r_iso-(r_iso-r_c)/2; %radius of cable
       with half of insulation [m]
87 A = 2*pi*r_c;  % Surface of copper per meter [m2]
88 A_iso = 2*pi*r_iso; % Surface of insulation per meter
       [m2]
89 A_iso_half = 2*pi*r_iso_half; % Surface of half of
       insulation per meter [m2]
90 xsect_iso = (r_iso)^2*pi-xsect; %Cross section of
       insulation [m2]
91
92 % Material properties
93
94 % Check inputs
95 if material ~= 1 && material ~=2 && insulation ~= 1
       && insulation ~=2
96     error('Error. Please select proper material.')
97 end
98
99 %Conductor:
100 %Copper:
101 if material == 1
102     res = 1.7E-2; %Resistivity @ 20C [Ohm*m/mm2]
103     a_res = 0.00393; % Temperature Coefficient @ 20C
```

```
104     a = 402; % Thermal Conducticity Copper [W/mK]
105     cp = 385; % Thermal heat capacity [J/kgK]
106     p = 8960; % Density copper [kg/m3]
107 %Alu:
108 else
109     res = 2.65E-2; %Resistivity @ 20C [Ohm*m/mm2]
110     a_res = 0.0036; % Temperature Coefficient @ 20C
111     a = 217; % Thermal Conducticity Copper in [W/mK]
112     cp = 897; % Thermal heat capacity in [J/kgK]
113     p = 2700; % Density in [kg/m3]
114 end
115
116 %Insulator:
117 %PVC:
118 if insulation == 1
119     a_iso = 0.17; % Thermal Conducticity [W/mK]
120     cp_iso = 960; % Thermal heat capacity [J/kgK]
121     p_iso = 1760; % Density of PVC kg/m3S
122 %EPR:
123 else
124     a_iso = 0.27; % Thermal Conducticity [W/mK] from
          http://www.engineeringtoolbox.com/thermal-
          conductivity-d_429.html
125     cp_iso = 1644; % Thermal heat capacity [J/kgK]
          from http://www.engineeringtoolbox.com/specific
          -heat-capacity-d_391.html
126     p_iso = 1350; % Density of EPR kg/m3S
127 end
128
129 %Resistance calculation
130 roh_20 = res*1/(xsect*1E6); % specific resistance at
    20C
131 R = roh_20*(1+a_res*(T_start - (20+273) )); %
    resistance at 20C
132
133
134 % Heat Capacities matrix
135 C = zeros(2,2);
136
137 C(1,1) = xsect * 1 * p * cp; %xsection in mm2
138 C(2,2) = (xsect_iso) * p_iso * cp_iso; %xsection_iso
    already in m2
139
140
141 %Concudctivity matrix
142 if geometry == 1
143     Ga = 4*pi*a;
144     Gb = 2*pi*a_iso/(log(r_iso_half/r_c));
145     Gc = 2*pi*a_iso/(log(r_iso/r_iso_half));
146 elseif geometry == 2
147     %Ga = a*1E-6/;
148     Gb = 2*pi*a_iso/(log(r_iso_half/r_c));
149     Gc = 2*pi*a_iso/(log(r_iso/r_iso_half));
```

```
150 end
151
152 Gkonv = hc * A_iso;
153 Grad = A_iso * e * bc * (T_all(4,1)^2 + T_amb^2) * (
    T_all(4,1) + T_amb);
154 G = G_matrix(Ga,Gb,Gc,Gkonv,Grad);
155
156 % Heat Sources and Sinks
157 Q = zeros(2,1);
158 Qrad = Grad * (T_all(1,1) - T_all(2,1));
159 Q(1) = I^2*R;
160 Q(2) = T_amb*((Gkonv+Grad)-(Gkonv+Grad)^2/(Gc+(Gkonv+
    Grad))) - Qrad;
161
162 %% Implicit Forward Euler method
163 t = 0;
164 n = 1;
165
166 while t < N
167     t(n+1) = t(n) + dt; %Increase time
168     T(:,n+1) = -(G*dt-C)^(-1) * (C*T(:,n) + Q*dt); %
        Calculate new temp
169     n = n+1; %increase index
170     T_all(:,n) = T_update(Ga,Gb,Gc,Gkonv,Grad,T(1,n),T
        (2,n),T_amb); %Update all nodes
171
172     %Update Joule losses, heat sources
173     R(n) = R_update(roh_20,a_res,T_all(1,n));
174     Q(1) = I^2*R(n);
175
176     %Update convection and radiation, heat sinks
177     Grad = A_iso * e * bc * (T_all(4,n)^2 + T_amb^2) *
         (T_all(4,n) + T_amb);
178     Qrad = Grad * (T_all(4,n) - T_amb);
179     G = G_matrix(Ga,Gb,Gc,Gkonv,Grad);
180     Q(2) = T_amb*((Gkonv+Grad)-(Gkonv+Grad)^2/(Gc+(
        Gkonv+Grad))) - Qrad;
181 end
182
183 %From K to C
184 T_all = T_all - 273;
185
186 if plot_mode == 1
187     mylegend{end+1} = [num2str(I) 'A: Conductor
        temperature'];
188     mylegend{end+1} = [num2str(I) 'A: Insulator
        temperature'];
189
190     plot(t,T_all(2,:),'--','Color',color(j,:),'
        LineWidth',2);
191     hold on;
192     plot(t,T_all(4,:),'Color',color(j,:),'LineWidth'
        ,2);
```

```
193 else
194     mylegend{1} = ['Conductor temperature'];
195     mylegend{2} = ['Insulator temperature'];
196
197     %%----- Text output -----
198     disp(['Cross-Section: ' num2str(xsection(j)) ' mm2
            :']);
199     disp(['Temperature conductor: ' num2str(T_all(2,
            end)) ' C']);
200     disp(['Temperature insulation: ' num2str(T_all(4,
            end)) ' C']);
201     disp(['Resistance: ' num2str(R(end)*1000) ' mOhm'
            ]);
202     disp(['Power losses: ' num2str(R(end)*I^2) ' W']);
203     disp(' ');
204     output(3,j) = T_all(2,end);
205     output(4,j) = T_all(4,end);
206
207     %%----- Plotting -----
208     figure(fig);
209     subplot(N_c,1,j);
210     plot(t,T_all(2,:),'--','color',[0 .5 0]);
211     hold on;
212     plot(t,T_all(4,:));
213     ylim([20 50]);
214      xlim([0 2000]);
215     title(['Nominal voltage: ' num2str(U(j)) 'V, '
            num2str(I) 'A, Cross-Section: ' num2str(xsection
            (j)) 'mm2'])
216
217     if show_res_plot
218     figure(fig_res);
219     plot(t,R*1000,'Color',color(j,:));
220     hold on;
221     mylegend_res{end+1} = ['Cross-Section: ' num2str(
            xsection(j)) 'mm2'];
222     end
223
224     if show_power_plot
225      figure(fig_power);
226          plot(t,R*I^2,'Color',color(j,:));
227      hold on;
228     end
229
230     R_(j) = R(end)*1000;
231     P_(j) = R(end)*I^2;
232     W_(j) = (xsect*p+xsect_iso*p_iso)*1000;
233     CD(j) = I/xsection(j);
234 end
235
```

```
236 figure(fig);
237 grid on;
238 legend(mylegend,'Location','SouthEast');
239 ylabel('Temperature in C');
240 xlabel('Time in s');
241
242 if show_res_plot
243  figure(fig_res);
244  grid on;
245  ylabel('Resistance in m\Omega');
246  xlabel('Time in s');
247  legend(mylegend_res,'Location','SouthEast');
248 end
249
250 if show_power_plot
251  figure(fig_power);
252  grid on;
253  ylabel('Power in W');
254  xlabel('Time in s');
255  legend(mylegend_res,'Location','SouthEast');
256 end
257
258 end
259
260 tightfig(fig);
261 if show_res_plot
262     tightfig(fig_res);
263 end
264 if show_power_plot
265     tightfig(fig_power);
266 end
267
268 %Create output file
269 output = abs([I_all;xsection;output(3,:);output(4,:);
    CD;1-CD/CD(1);W_;1-W_/W_(1);R_;1-R_/R_(1);P_;1-P_/
    P_(1)])
270
271 if show_summary_plot
272 figure(fig_prop);
273 %Current density over voltage:
274 subplot(2,2,1);
275 plot(U,CD,'x-');
276 xlabel('Voltage in V');
277 ylabel('Current density in A/mm2');
278
279 %Weight over voltage:
280 subplot(2,2,2);
281 plot(U,W_,'x-');
282 xlabel('Voltage in V');
283 ylabel('Weight in g/m');
284
285 %Resistance over voltage:
```

```
subplot(2,2,3);
plot(U,R_,'x-');
xlabel('Voltage in V');
ylabel('Resistance in m\Omega/m');

%Power losses over voltage:
subplot(2,2,4);
plot(U,P_,'x-');
xlabel('Voltage in V');
ylabel('Power losses in W/m');

for j = 1:4
    subplot(2,2,j);
    grid on;
    set(gca,'XTick',U)
end

tightfig(fig_prop);
end
```

Pre-charge simulation

```
% -- PRE CHARGE SIMULATION - Fabian Luttenberger 2016 --%

close all;
clear all;
clc;

%init
U = [350 650 1350];
C = 1000E-6; % Capacitance [Farad]
R_Res = [14 26 54]; % Resistance [Ohm]
R_cells = [34.2 136.8 547]*1E-3; % Cell resistances [Ohm]
R_line = 7*[1 2.3 6.2]*1E-3; % HV path resistance for 7m length [Ohm]
N = 0.5; % Length of simulation [s]
dt = 0.0001; % Time step [s]

pre_time = [0.5 0.5 0.5];
cap_charge = [0.98 0.98 0.98];

mode = 2;
% 1... Close HV contactor after pre-charge time pre_time
% 2... Close HV contactor if voltage of capactior reached U*cap_charge

%Define variables
R_HV = R_line+R_cells; % HV path resistance [s]
```

```
25 uc = zeros(4,1); % row #1: Beginning current peak,
       #2: after pre-charge, #3:
26 ur = U';
27 tau = R_Res*C;
28 du = U-U.*cap_charge;
29 I = U'./R_Res';
30 Nc = length(U);
31 outputs = zeros(3,3);
32 outputs(:,1) = I;
33 trigger = 0; %trigger for pre-charge completion
34 mylegend = {}; %Legend
35
36 %Run Pre-Charge loop:
37 for j = 1:Nc
38
39
40 t = 0;
41 n = 1;
42 R = R_Res;
43
44 mylegend{j} = [num2str(U(j)) 'V'];
45
46 % Pre-charge calculation loop:
47 while t < N
48     t(n+1) = t(n) + dt; %Increase time step
49
50 %Pre-charging is finished:
51     if (t(n) >= pre_time(j) && mode == 1) || (ur(j,n)
           < du(j) && mode == 2)
52         if trigger == 0
53             trigger = 1;
54             R(j) = R_HV(j);
55             i = n; % Save index when pre-charging is
                   finished
56         end
57     end
58         uc(j,n+1) = (R(j)*C+dt)^(-1)*(U(j)*dt+R(j)*C*
               uc(j,n));
59         ur(j,n+1) = U(j) - uc(j,n+1);
60         I(j,n+1) = ur(j,n)/R(j);
61
62     n = n + 1;
63 end
64
65 %Set Outputs
66 if mode == 2
67     outputs(j,1) = t(i);
68 end;
69 outputs(j,2) = ur(j,i)/R(j);
70 outputs(j,3) = uc(j,i);
71 outputs(j,4) = ur(j,i);
72
73 trigger = 0;
```

```
74 end
75
76 %Numerical outputs:
77 disp('System voltages [V]:');
78 disp(num2str(U'))
79 disp(' ');
80  if mode == 2
81      disp('Pre-charge times [s]:');
82  else
83      disp('Initial current peak [A]:');
84  end
85 disp(num2str(outputs(:,1)))
86 disp(' ');
87 disp('Current peak after pre-charging [A]:');
88 disp(num2str(outputs(:,2)))
89 disp(' ');
90 disp('Capacitor voltage after pre-charging [V]:');
91 disp(num2str(outputs(:,3)))
92 disp(' ');
93 disp('Voltage drop over resistor after pre-charging [
     V]:');
94 disp(num2str(outputs(:,4)))
95
96 %Plotting:
97 scrsz = get(groot,'ScreenSize');
98 fig = figure('Position',[10 100 scrsz(3)/1.8 scrsz(4)
     /1.3]);
99
100 %Plot capactior voltage:
101 subplot(3,1,1);
102 plot(t,uc);
103 grid on;
104 xlim([0 N]);
105 title('Capacitor voltage');
106 xlabel('Time in s');
107 ylabel('Uc in V');
108 ylim([0 U(3)]);
109 legend(mylegend);
110
111 %Plot voltage drop over resistor:
112 subplot(3,1,2);
113 plot(t,ur);
114 grid on;
115 xlim([0 N]);
116 title('Voltage drop over pre-charge resistor');
117 xlabel('Time in s');
118 ylabel('Ur in V');
119 ylim([0 U(3)]);
120 legend(mylegend);
```

```
121
122 %Plot current:
123 subplot(3,1,3);
124 plot(t,I);
125 grid on;
126 xlim([0 N]);
127 %ylim([0 300]);
128 title('Battery current');
129 xlabel('Time in s');
130 ylabel('I in A');
131 legend(mylegend);
132
133 tightfig(fig);
```

List of Figures

1.1. Current plotted over voltage with constant power based on [3] 2
1.2. Vehicle topology and electric drivetrain 3

2.1. WLTP and CADC speed profiles 10
2.2. Workflow for dynamic power calculation 11
2.3. Transformed WLTP and CADC power profiles 14
2.4. RMS Currents for the WLTP and CADC power profiles at the prospected nominal system voltage levels 16

3.1. Clearance and creepage distance 20
3.2. Creepage distances according to IEC 60664 24
3.3. Principle structure of a HV system with insulation monitoring adapted from [7] 28

4.1. Schematic battery pack architecture 31
4.2. Principle structure of a lithium-ion cell and working principle during discharge 33
4.3. Equivalent electric circuit according to [24] 35
4.4. Exemplary Nyquist plot according to [24] 36
4.5. Current charge pulse and voltage drops over time according to [24] 37
4.6. Passive (a) and active (b) balancing circuit examples for 3 cells connected in series 40
4.7. Thermal model of a cable with insulator adapted from [27] . 42
4.8. Simulation results for surface temperatures of cables 49
4.9. Cable Current density, weight, steady-state resistance, and steady-state power losses at different voltage levels and resulting currents 51

4.10. Comparison between copper and aluminum with same conductivity and same heat capacity for copper cross section, adapted from [26] 53
4.11. Structure of contactor 58
4.12. Voltage and current curve during contactor switch-off adapted from [37] 59
4.13. DC circuit during contactor switch-off according to [38] . . . 60
4.14. Blowing magnet principle 62
4.15. Arc time of a sealed contactor with a system voltage of 600V and a current of 75A taken from [38] 63
4.16. Weight and volume of various contactors over their nominal switching current 64
4.17. Weight and volume of various contactors grouped into current ranges over their maximal switching voltage 66
4.18. Arc voltage for single and splitted arc adapted from [37] . . . 67
4.19. Structure of fuse 69
4.20. Voltage and current graph of a fuse, adapted from [45] 70
4.21. Fault circuit 71
4.22. Fault current rise at different voltage levels 72
4.23. Fuse body length and volume at different voltage levels . . . 75
4.24. HV schematic with pre-charge unit 77
4.25. Typical pre-charge behavior 78
4.26. Pre-charge behavior for a defined pre-charge time of 200 ms . 82
4.27. Pre-charge behavior for charging to a defined capacitor level of 90% of the system voltage 85

5.1. Inverter circuit according to [11] 90
5.2. IGBT structure according to [6] 91
5.3. Torque over speed in constant torque and constant power region according to [11] 94
5.4. Electrical machine insulation adapted from [57] 95

A.1. IP code formation according to [58] 100

List of Tables

1.1. General voltage levels according to [3] 4
1.2. Voltage classes according to ISO 6469-3 5
1.3. Definition of system voltage levels 7

2.1. Drive cycle characteristics 9
2.2. Vehicle parameters and energy efficiency taken from [9] . . . 12
2.3. Summary of RMS power and currents at different voltage levels, nominal voltages were considered 15

3.1. Minimum required insulation resistance for different maximum system voltages according to ISO 6469-3 20
3.2. Clearance distances according to IEC 60664-1 22
3.3. Altitude correction factors up to 6000 m according to IEC 60664-1 22
3.4. CTI values according to IEC 60664 23
3.5. Interpolated creepage distances according to IEC 60664 25

4.1. Cell characteristics NMC/graphite lithium-ion pouch cell . . 34
4.2. Cell resistance 38
4.3. Cell losses of WLTP and CADC 39
4.4. conductor and insulation characteristics according to [26, 27] 44
4.5. Transient thermal behavior of a cable at different voltage levels and currents 48
4.6. Thermal simualtion per-meter results for cable with PVC insulation, voltage level 1 as reference 50
4.7. Comparison between copper and aluminum 52
4.8. HV connection classifications 55
4.9. Overview of the analyzed fuses 73
4.10. Input parameters for the pre-charge simulation 80

List of Tables

4.11. Resistance values for defined pre-charge times 81
4.12. Simulation results with a defined pre-charging time of 200 ms 83
4.13. Resistor values for defined capacity level 84
4.14. Simulation results with for charging to a defined capcitor level of 90% of the system voltage 86

A.1. IP ratings according to [58] 101
A.2. Additional letters according to [58] 102

B.1. Simulation results with a defined pre-charging time 104
B.2. Simulation results with for charging to a defined capcitor level 105

Bibliography

[1] Benedikt Schmülling. *Ausgewählte Themen der elektrischen Antriebstechnik 2 - Elektromobilität*. Tech. rep. Graz, Technical University, 2014.

[2] Matthias Deiml, Armin Engstle, and Martin Schlecker. *Coup-e 800: Electric High-Performance Powertrain With 800 Volt Powernet*. Apr. 2014.

[3] Martin-Hans Fischer. *Voltage Classes for Electric Mobility*. Tech. rep. ZVEI - German Electrical and Electronic Manufactures' Association, 2013.

[4] *ISO 6469-3: Electrically propelled road vehicles - Safety specifications - Part 3: Protection of persons against electric shock*. Dec. 2011.

[5] *ISO 6469-1: Electrically propelled road vehicles - Safety specifications - Part 1: On-board rechargeable energy storage system (RESS)*. Sept. 2009.

[6] Maurice Kowal et al. *Optimized Voltage Range for Future Electric and Hybrid-Electric Vehicles*. Tech. rep. Institute for Power Electronics and Electrical Drives (ISEA), Apr. 2011.

[7] Reiner Korthauer. *Handbuch Lithium-Ionen-Batterien*. Springer-Verlag, 2013.

[8] Heinz Steven. *Homologation test cycles worldwide*. Green Global NCAP labelling / green scoring Workshop, 2013.

[9] H. Helms et al. *Electric vehicle and plug-in hybrid energy efficiency and life cycle emissions*. Tech. rep. Ifeu – Institut fur Energie- und Umweltforschung, 2010.

[10] DieselNet. *Emission Test Cycles*. Sept. 8th, 2015. URL: http://www.dieselnet.com/standards/cycles/#eu-ld.

[11] Ali Emadi. *Advanced Electric Drive Vehicles*. CRC Press, 2015.

[12] CHEMIE.DE. *Luftdichte*. Oct. 11th, 2015. URL: http://www.chemie.de/lexikon/Luftdichte.html.

[13] *IEC 60664-1: Insulation coordination for equipment within low-voltage systems - Part 1: Principles, requirements and tests*. Apr. 2007.

[14] *ISO 6469-2: Electrically propelled road vehicles - Safety specifications - Part 2: Vehicle operational safety means and protection against failures*. Sept. 2009.

[15] *IEC 61851-1: Electric vehicle conductive charging system - Part 1: General requirements*. Apr. 2013.

[16] Mohammad Hassan Memari and Victoria Jane Nakanwagi. *Electrical Insulation in a 400 V Battery Module for Hybrid Vehicles*. Master's Thesis. 2014.

[17] *IEC 61851-23: Electric vehicle conductive charging system – Part 23: DC electric vehicle charging station*. Mar. 2014.

[18] Yong Liu. *Power Package Electrical Isolation Design*. English. In: *Power Electronic Packaging*. Springer New York, 2012, pp. 9–26. ISBN: 978-1-4614-1052-2. DOI: 10.1007/978-1-4614-1053-9_2. URL: http://dx.doi.org/10.1007/978-1-4614-1053-9_2.

[19] Holger Potdevin. *Insulation Monitoring in High Voltage Systems for Hybrid and Electric Vehicles*. In: *ATZelektronik* 4 (June 2009), pp. 28–31.

[20] Chunming Zhao and Qing Li. *Research on On-line Monitoring Methods of High Voltage Parameter in Electric Vehicles*. In: *World Electric Vehicle Journal Vol. 4*. Nov. 2010.

[21] K. Jalkanen et al. *Cycle aging of commercial NMC/graphite pouch cells at different temperatures*. In: *Applied Energy* 154 (2015), pp. 160–172. ISSN: 0306-2619. DOI: http://dx.doi.org/10.1016/j.apenergy.2015.04.110. URL: http://www.sciencedirect.com/science/article/pii/S0306261915005735.

[22] AVL List GmbH. *AVL internal document, unpublished*. 2015.

[23] Hans-Georg Schweiger et al. *Comparison of Several Methods for Determining the Internal Resistance of Lithium Ion Cells*. In: *Sensors* 10.6 (2010), p. 5604. URL: http://www.mdpi.com/1424-8220/10/6/5604.

[24] Grzegorz Piłatowicz et al. *A critical overview of definitions and determination techniques of the internal resistance using lithium-ion, lead-acid, nickel metal-hydride batteries and electrochemical double-layer capacitors as examples*. In: *Journal of Power Sources* 296 (2015), pp. 365–376. DOI: http://dx.doi.org/10.1016/j.jpowsour.2015.07.073. URL: http://www.sciencedirect.com/science/article/pii/S0378775315301245.

[25] J. Cao, N. Schofield, and A. Emadi. *Battery balancing methods: A comprehensive review*. In: *2008 IEEE Vehicle Power and Propulsion Conference*. Sept. 2008, pp. 1–6.

[26] J. Grandvuillemin et al. *Ampacity of power bus bars for Hybrid-Electric or Electric Vehicles*. In: *Vehicle Power and Propulsion Conference, 2008. VPPC '08. IEEE*. Sept. 2008, pp. 1–6.

[27] J. Grandvuillemin et al. *Thermal Modelling Of Enclosed Cables In Automotive Applications*. In: *Vehicle Power and Propulsion Conference, 2007. VPPC 2007. IEEE*. Sept. 2007, pp. 730–735. DOI: 10.1109/VPPC.2007.4544220.

[28] Michael R. Yenchek, Gregory P. Cole, and John C. Edwards. *Thermal Modeling of Portable Power Cables*. Tech. rep. United States Department of the Interior, Bureau of Mines, 1993.

[29] Bernd Künstl. *Stromtragfähigkeitsgrenzen von elektrischen Leitungssystemen*. Master's Thesis. Graz, Technical University, Nov. 2011.

[30] Aluru Teja and K. Rajagopala. *Thermal Analysis by Conduction Convection and Radiation in a Power Cable*. In: *IOSR Journal of Electrical and Electronics Engineering (IOSR-JEEE)* (June 2014), pp. 51–56.

[31] *PVC isolierte HV Leitung für automobile Anwendungen*. LEONI Kabel GmbH. July 2012.

[32] Larry Pryor, Rick Schlobohm, and Bill Brownell. *A Comparison Of Aluminum Vs. Copper As Used In Electrical Equipment*. May 2008.

[33] *High Voltage Contact and Connector Systems for Electric and Hybrid Vehicles*. Rosenberger Hochfrequenztechnik GmbH Co. KG. Oct. 2015.

[34] *Automtive Relays; High Voltage Contactors*. EVC500. Rev. 0213. Tyco Electronics Corporation. Feb. 2013.

[35] Hendrik Koepf et al. *Breaking performance of protection devices for automotive dc powertrains with a voltage of 450 V*. In: *ICEC 2014; The 27th International Conference on Electrical Contacts; Proceedings of*. June 2014, pp. 1–6.

[36] Jens Jebramcik and Frank Berger. *Observations on switching characteristics of arc chutes in DC contactors*. In: *ICEC 2014; The 27th International Conference on Electrical Contacts; Proceedings of*. June 2014, pp. 1–6.

[37] Timo Mützel. *Physikalische Grundlagen und Lösungsansätze zum Schalten von Gleichströmen*. In: *Kontaktverhalten und Schalten, VDE 21. Albert-Keil-Kontaktseminar*. 2011, pp. 1–7.

[38] Jens Jebramcik and Frank Berger. *DC-Schaltverhalten von Löschkammerkonstruktionen für Schütze*. In: *The 27th International Conference on Electrical Contacts; Proceedings of*. Oct. 2013, pp. 1–10.

[39] Picker. *Contact Arc Phenomenon*. Dec. 15th, 2015. URL: http://www.pickercomponents.com/pdf/application%20note/Contact_ARC_Phenomenon.pdf.

[40] Xue Zhou et al. *Experimental study on arc behaviors of a bridge-type contact when opening a resistive load in the range of from 280VDC to 730 VDC*. In: *Electrical Contacts (Holm), 2014 IEEE 60th Holm Conference on*. Oct. 2014, pp. 1–7.

[41] *Introducing KILOVAC LEV100 Series 900 Vdc Contactor*. Tyco Electronics Corporation. Apr. 2008.

[42] *HVDC RELAY*. Xiamen Hongfa Electroacoustic Co.,Ltd. Apr. 2008.

[43] H.C. Cline. *Fuse protection of DC systems*. In: American Power Conference, Chicago, IL (United States), Sept. 1995.

[44] A. Wright. *Construction, behaviour and application of electric fuses*. In: *Power Engineering Journal* 4.3 (May 1990), pp. 141–148. ISSN: 0950-3366.

[45] C.P. Yang et al. *Simulation methodologies to support novel fuse design for energy storage systems using COMSOL*. In: *Hybrid and Electric Vehicles Conference 2013 (HEVC 2013), IET*. Nov. 2013, pp. 1–5. DOI: 10.1049/cp.2013.1888.

[46] Charles Mulertt. *Fuse Operation under DC Conditions*. Tech. rep. Mersen - Tech Topics: Component Protection Note 1, Issue 1, 2006.

[47] J.C. Gomez et al. *Application of the mechanistic arc model to DC current limiting fuses*. In: *Power Engineering Society Winter Meeting, 2000. IEEE*. Vol. 3. Jan. 2000, 2145–2149 vol.3. DOI: 10.1109/PESW.2000.847685.

[48] *Bussmann series IEC High speed catalogue*. Eaton Industries Manufacturing GmbH. Feb. 2015.

[49] Pacific Engineering Corporation. *EV Fuse*. Dec. 20th, 2015. URL: http://www.pecj.co.jp/en/fuse/ev/ev.html.

[50] A.K. Mensah-Brown et al. *Capacitor precharging and capacitance/resistance measurement in electric vehicle drive system*. US Patent App. 14/198,981. Sept. 2015. URL: http://www.google.com/patents/US20150251542.

[51] *HPRS 100 - High-power resistor in metal profile*. KRAH ELEKTRONISCHE BAUELEMENTE GMBH. July 2010.

[52] Davide Andrea. *Li-Ion BMS - Precharge - A design guide to DC precharge circuits.* Sept. 10th, 2016. URL: http://liionbms.com/php/precharge.php.

[53] T. Hosking. *Comparative evaluation and analysis of the 2008 Toyota Lexus, Camry and 2004 Prius DC link capacitor assembly vs. the SBE Power Ring DC link capacitor*. In: *Vehicle Power and Propulsion Conference, 2009. VPPC '09. IEEE*. Sept. 2009, pp. 717–723.

[54] Elke Schuster et al. *Thermal behavior and electrochemical heat generation in a commercial 40 Ah lithium ion pouch cell*. In: *Journal of Power Sources* 286 (2015), pp. 580–589. ISSN: 0378-7753. DOI: http://dx.doi.org/10.1016/j.jpowsour.2015.03.170. URL: http://www.sciencedirect.com/science/article/pii/S0378775315006047.

[55] A. Philippou, M. Bina, and F. J. Niedernostheide. *Automated vertical design optimization of a 1200V IGBT*. In: *Simulation of Semiconductor Processes and Devices (SISPAD), 2015 International Conference on*. Sept. 2015, pp. 72–75.

[56] M. Frisch and T. Ernoe. *Power module with additional low inductive current path*. In: *Integrated Power Electronics Systems (CIPS), 2010 6th International Conference on*. Mar. 2010, pp. 1–6.

[57] Don-Han Hwang et al. *Analysis of voltage stress in stator winding of IGBT PWM inverter-fed induction motor systems*. In: *Electrical Machines and Systems, 2003. ICEMS 2003. Sixth International Conference on*. Vol. 1. Nov. 2003, 440–444 vol.1.

[58] *IEC 60529: Schutzart durch Gehäuse (IP-Code)*. Sept. 2000.